

An Investigation on the Comparative Sensor Performance of Polysilicon Nanowires with Single Crystal Silicon Nanowire

By

Anamika Shargen

Mehedi Hasan

&

Salim Sazzad

Submitted to the

Department of Electrical & Electronic Engineering

East West University

In partial fulfillment of the requirements for the degree of
Bachelor of Science in Electrical & Electronic Engineering

(B.Sc. in EEE)

Spring, 2017

Thesis Advisor

Dr. Mohammad Mojammel Al Hakim

Department Chairperson

Dr. MuhammedMazharul Islam

Abstract

We study for the first time the effect of nanowire thickness and doping concentration on the electrical characteristics of single crystal and polycrystalline silicon nanowire biosensors. For nanowire thicknesses of 100 nm and 75 nm, a plausible sub-threshold slope around 100 mV/decade for a viable biosensor operation only achieve if doping concentration is $2 \times 10^{16}/\text{cm}^3$ or below both for single crystal and poly Si nanowires. For a 50nm nanowire thickness a relatively wide doping concentration range with a maximum doping up to $4 \times 10^{17}/\text{cm}^3$ choose for biosensor design while maintaining decent sub-threshold characteristics. The widest range of doping concentrations choose for 25nm and 10nm nanowire thickness with a maximum doping up to $10^{18}/\text{cm}^3$ while maintaining a promising sub-threshold slope around 95 mV/decade for a viable biosensor design using single crystal and polycrystalline silicon nanowires. In general poly Si NW shows inferior characteristics than single crystal Si NW. However, for 10nm Si NW single crystal & poly Si NW show same sub-threshold slopes at all doping densities. Considering the fact that spacer etch process provides the cheapest & mass manufacturable platform for biosensor fabrication using poly Si material in comparison to the available single crystal platforms. It decides from this work that poly Si NW biosensor with Si thickness $\leq 10\text{nm}$ is the possible commercial route of sensor fabrication.

Acknowledgement

First of all, we would like to thank our thesis supervisor Professor Dr. Mohammad Mojammel Al Hakim, Department of Electrical and Electronic Engineering of East West University (EWU), Dhaka, for his affectionate guidance and giving us the great opportunity to research on this interesting topic. Without his support we could not reach the current stage with this thesis. He continually provided us with invaluable knowledge throughout this research. We greatly appreciate his dedication and owe him lots of gratitude for guiding us with friendly behavior.

We also want to thank to our honorable teacher Dr. Anisul Haque, Professor of Department of Electrical and Electronic Engineering of East West University for supporting us with his profound knowledge on semiconductor materials.

We also want to thank to our department chairperson Dr. Mohammed Mazharul Islam for his support.

Finally, we want to thank our family for support us as well as thank to all of our friends for their endless love and support.

Approval

The thesis title “An Investigation on the Comparative Sensor Performance of Polysilicon Nanowires with Single Crystal Silicon Nanowire” submitted by Mehedi Hasan (2013-2-80-061), Salim Sazzad (2013-2-80-063) and Anamika Shargen (2013-2-80-068) in the semester of Spring-2017, has been approved as satisfactory in partial fulfillment of the degree of the Bachelor of Science in Electrical and Electronic Engineering on April, 2017.

Professor Dr. Mohammad Mojammel Al Hakim
Department of Electrical and Electronic Engineering
East West University, Dhaka 1212, Bangladesh

Authorization

We hereby declare that we are the sole authors of this thesis. We authorize East West University to lend this thesis to other institutions for the purpose of scholarly research.

Salim Sazzad

Mehedi Hasan

Anamika Shargen

We further authorize East West University to reproduce this thesis by photocopy or other means, in total or in part, at the request of other institutions or individuals for the purpose of scholarly research.

Salim Sazzad

Mehedi Hasan

Anamika Shargen

Contents

Abstract	2
Acknowledgement	3
Approval	4
Authorization	5
Contents	6
List of Figures	7
List of Tables	8
Chapter 1	9
Introduction	9-10
Chapter 2	11
Methodology	11
2.1 Device features and simulation models for single crystal silicon nanowire.....	11-14
2.2 Simulation models for poly silicon nanowire.....	14-15
2.3 Simulation profile.....	15-16
Chapter 3	17
Results and Discussion	17-26
Chapter 4	27
Conclusion	27
References	28
Chapter 5	29
Appendix A	29
Single Crystal Silicon Nanowire.....	29-47
Appendix B	48
Poly Crystal Silicon Nanowire.....	48-66

List of Figures

Figure 2.1: Schematic of the simulated p-type silicon nanowire.....	11
Figure 2.2: The distribution of acceptor and donor-like trap states across forbidden energy gap.....	15
Figure 2.3: Cross-sectional view of p-type nanowire showing the mesh density used in this simulation.....	16
Figure 3.1: Sub-threshold characteristics of p-type Silicon nanowires with $10^{16}/\text{cm}^3$ doping concentration at 100nm thickness; (a) single crystal Si and (b) poly crystal Si. The NWs have channel length of $1\mu\text{m}$	17
Figure 3.2: Output characteristics of p-type Silicon nanowires with $10^{16}/\text{cm}^3$ doping concentration at 100nm thickness; (a) single crystal Si and (b) poly crystal Si. The NWs have channel length of $1\mu\text{m}$	18
Figure 3.3: Sub-threshold characteristics of p-type Silicon nanowires with $4\times 10^{17}/\text{cm}^3$ doping concentration at 100nm thickness; (a) single crystal Si and (b) poly crystal Si. The NWs have channel length of $1\mu\text{m}$	19
Figure 3.4: Output characteristics of p-type Silicon nanowires with $4\times 10^{17}/\text{cm}^3$ doping concentration at 100nm thickness; (a) single crystal Si and (b) poly crystal Si. The NWs have channel length of $1\mu\text{m}$	20
Figure 3.5: Sub-threshold characteristics of p-type Silicon nanowires with $10^{16}/\text{cm}^3$ doping concentration at 25nm thickness; (a) single crystal Si and (b) poly crystal Si. The NWs have channel length of $1\mu\text{m}$	21
Figure 3.6: Output characteristics of p-type Silicon nanowires with $10^{16}/\text{cm}^3$ doping concentration at 25nm thickness; (a) single crystal Si and (b) poly crystal Si. The NWs have channel length of $1\mu\text{m}$	22
Figure 3.7: Sub-threshold characteristics of p-type Silicon nanowires with $4\times 10^{17}/\text{cm}^3$ doping concentration at 25nm thickness; (a) single crystal Si and (b) poly crystal Si. The NWs have channel length of $1\mu\text{m}$	23
Figure 3.8: Output characteristics of p-type Silicon nanowires with $4\times 10^{17}/\text{cm}^3$ doping concentration at 25nm thickness; (a) single crystal Si and (b) poly crystal Si. The NWs have channel length of $1\mu\text{m}$	24
Figure 3.9: Sub-threshold slopes as a function of doping concentrations for different thicknesses of single crystal Silicon and poly crystal Silicon nanowires.....	25

List of Tables

Table 2.1: Parameters for Equations 2.1 to 2.7.....	12-13
Table 2.2: Default Parameter for equations 2.8 to 2.10.....	13-14
Table 2.3: Default Parameters of Slotbooms Bandgap Narrowing Model foe equation 2.11..	14
Table 2.4: Default mobility model values for polysilicon.....	14

Chapter 1

Introduction

A nanowire is an extremely small structure, typically with diameters on the order of few nanometers up to 100nm. Silicon nanowire is one of the 1D nano-structures and has emerged as the promising sensing nanomaterial upon its unique mechanical, electrical and optical properties [1]. Due to its small size and large surface-to-volume ratio the depletion and accumulation of charge-carriers produced by specific binding of biological macromolecule on the surface affects the entire cross sectional conduction pathway, that's why NW devices give extraordinary sensitivity when compared to other transducers reported in the literature [2]. Si-NW chemical sensors operated as field-effect transistors (FET) are currently the most commonly used structures [3]. The application of silicon nanowire as a sensing nanomaterial for detection of biological and chemical species has gained attention due to its unique properties [4]. Though this advantage of nanowires has been used to sense ions, proteins, DNA and viruses, some important issues remain for mass commercialization. The appropriate choice of thickness, length, doping of nanowires and cost of fabrication are the outstanding issues has to be specified.

In general, the silicon nanowire nanofabrication toolbox consists of two techniques such as bottom-up approach and top-down approach. Generally, single crystal silicon nanowire is fabricated by using bottom-up technique. Bottom-up approach is a growth or synthesized technique of the Si NWs from bulk silicon wafers either metal catalyzed-assisted or metal catalyzed-free [4]. Bottom-up nano-fabrication is in principle simple and provides many high quality materials. In recent years, many researchers have successfully fabricated Si NWs using this approach in producing a large quantity of Si NWs [4]. In these techniques, suitable methods for accurate nanowire alignment are lacking, and electrical contact formation is problematic, making it difficult to construct functional device arrays [3].

Some expensive top-down technique is also exists for fabricating single crystal silicon nanowire which overcomes the shortcomings of bottom-up. Several groups used nano-patterning techniques such as deep-UV photolithography and electron beam lithography to fabricate silicon nanowires on silicon-on-insulator (SOI) substrate [6]. This has the advantage of CMOS compatibility. But the major disadvantage of this technique is the high cost associated with these advanced lithography techniques and expensive SOI wafers. Recently a low cost, top-down approach to nanowire fabrication has been reported that uses thin film technology and spacer etch technique [6-7]. This approach is particularly attractive because it produces nanowires with nano-scale dimensions using mature lithography in combination with standard deposition and spacer etch techniques that are widely available in industry. More importantly, this process can be used for glass or plastic substrates suitable for the realization of low cost disposable diagnostic kits. However, in this approach defined nanowires are usually amorphous and/ or polysilicon depending on the deposition and annealing conditions and hence, nanowire material usually composed of grain boundaries and defects which may also affect its electrical characteristics eventually affecting biosensor performance realized in these nanowires. So far there have been only a number of reports on poly silicon nanowires and there is no study comparing the performance of single crystal & poly crystalline silicon nanowire biosensors.

In this study we first time perform a critical comparison of single crystal & poly crystalline Si NW's electrical performance to appraise in depth the achievable performance of poly Si NW biosensor in comparison to single crystal Si NW while poly Si platform has significant cost advantage. The effect of nanowire thickness and doping concentration on the electrical characteristics of both type silicon nanowires are investigated which also provides the proper combination of nanowire thickness and doping concentration to ensure the sensitive operation for both type of silicon. The electrical characteristics of a p-type silicon (single crystal and poly crystal) nanowire having a nanowire length $1\mu\text{m}$ is studied at various thicknesses and doping concentrations. 10nm, 25nm, 50nm, 75nm and 100nm thick nanowires with doping density varying from $10^{16}/\text{cm}^3$ to $10^{18}/\text{cm}^3$ are investigated.

Chapter 2

Methodology

2.1 Device features and simulation models for single crystal silicon nanowire

The investigation on the sensitivity of Silicon nanowire for biosensor application were done with the help of numerical simulations using the software SILVACO Atlas device simulator [11], installed on the VLSI lab of East West University. A p-type silicon nanowire was created on 100nm oxide with a 500nm buried Si layer. A secondary gate (backgate) is made with 25nm Al beneath the buried Si layer. The gate oxide thickness was 2nm and a heavily doped polysilicon layer was used as top gate material. In the silicon nanowire, two heavily doped regions on the two sides of the channel were employed to ensure ohmic contact on the source/drain regions. The gate doping was $10^{20}/\text{cm}^3$ and the source/drain regions were also heavily doped with the doping density of $10^{20}/\text{cm}^3$. Here, the gate doping was n-type whereas the drain and the channel doping was p-type. To contact source to drain and gate, aluminum electrode was chosen.

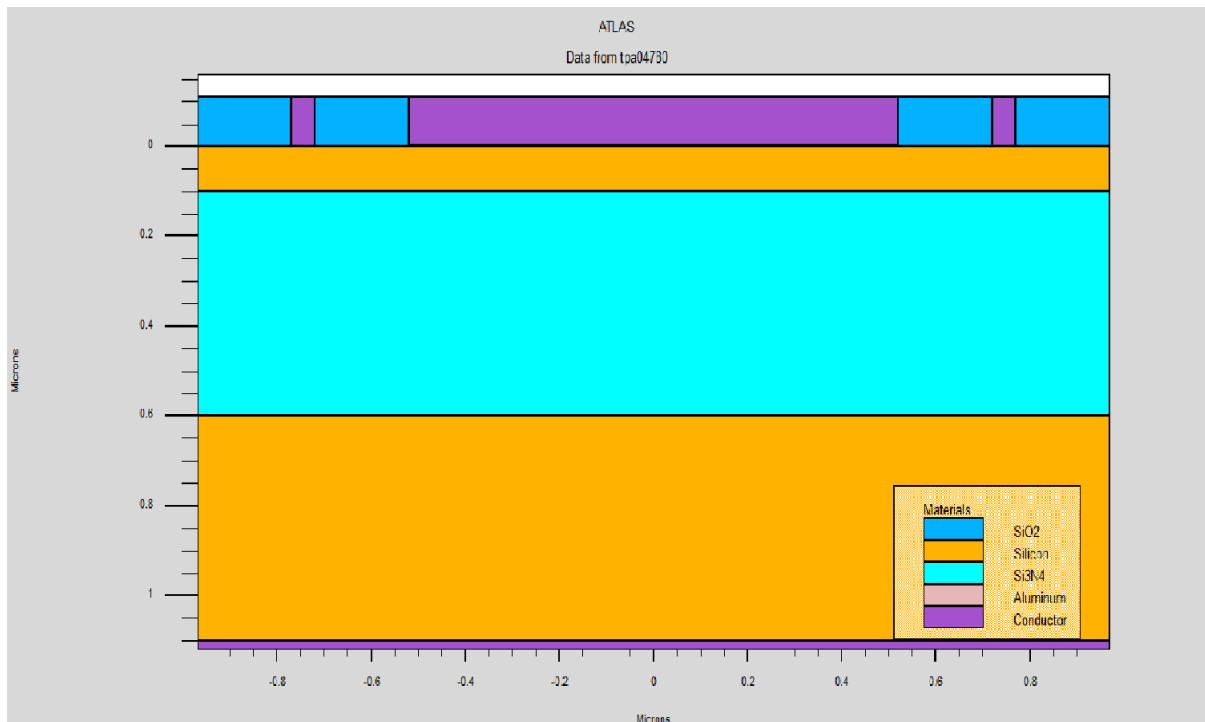


Figure 2.1: Schematic of the simulated p-type silicon nanowire.

In simulation our Si NW thickness were chosen at 100nm, 75nm, 50nm, 25nm and 10nm. Body doping of NW was also varied from $10^{16}/\text{cm}^3$ to $10^{18}/\text{cm}^3$ as Si-NW thickness 10nm quantum effect is neglected and a classical drift diffusion model is used to investigate Si-NW behavior. Fermi-Dirac (FERMI) carrier statistics model was used to account for certain properties of very highly doped (degenerate) materials. To accurately model carrier mobility in the constricted volume of NW Lombardi (CVT) model was used to take account temperature (T_L), perpendicular electric field (E_{\perp}), parallel electric field (EII) and doping concentration (N) effects [11]. In the CVT model, the transverse field, doping dependent and temperature

dependent parts of the mobility are given by the three components that are combined using Mathiessen's rule.

These components are surface mobility limited by scattering with acoustic photons (μ_{AC}), the mobility limited by the surface roughness (μ_{SR}) and the mobility limited by scattering with optical intervalley photons (μ_b) are combined using Mathiessen's rule as follows [11]:

$$\mu_T^{-1} = \mu_{AC}^{-1} + \mu_b^{-1} + \mu_{SR}^{-1} \quad (2.1)$$

The first component, surface mobility limited by scattering with acoustic phonons equations [11]:

$$\mu_{AC,n} = \frac{BN.CVT}{E_{\perp}} + \frac{CN.CVT N^{\tau N.CVT}}{T_L E_{\perp}^{1/3}} \quad (2.2)$$

$$\mu_{AC,p} = \frac{BN.CVT}{E_{\perp}} + \frac{CN.CVT N^{\tau P.CVT}}{T_L E_{\perp}^{1/3}} \quad (2.3)$$

The equation parameters BN.CVT, BP.CVT, CN.CVT, CP.CVT, TAUN.CVT, and TAUP.CVT used for this simulation are shown in Table 2.1 [11].

The second component, μ_{sr} is the surface roughness factor and is given by [11]:

$$\mu_{sr} = \frac{DELN.CVT}{E_{\perp}^2} \quad (2.4)$$

$$\mu_{sr} = \frac{DELP.CVT}{E_{\perp}^2} \quad (2.5)$$

The equation parameters DELN.CVT and DELP.CVT used for this simulation are shown in Table 2.1 [11].

The third mobility component, the mobility limited by scattering with optical intervalley phonons is given by [11]:

$$\mu_{b,n} = MU0N.CVT \exp\left(\frac{-PCN.CVT}{N}\right) + \frac{\left[MUMAXN.CVT \left(\frac{T_L}{300}\right)^{-GAMN.CVT} - MU0N.CVT\right]}{1 + \left(\frac{N}{CRN.CVT}\right)^{ALPHN.CVT}} - \frac{[-MU1N.CVT]}{1 + \left(\frac{CSN.CVT}{N}\right)^{BETAN.CVT}} \quad (2.6)$$

$$\mu_{b,p} = MU0P.CVT \exp\left(\frac{-PCP.CVT}{N}\right) + \frac{\left[MUMAXP.CVT \left(\frac{T_L}{300}\right)^{-GAMP.CVT} - MU0P.CVT\right]}{1 + \left(\frac{N}{CRP.CVT}\right)^{ALPHP.CVT}} - \frac{[-MU1P.CVT]}{1 + \left(\frac{CSP.CVT}{N}\right)^{BETAP.CVT}} \quad (2.7)$$

Table 2.1: Parameters for Equations 2.1 to 2.7

Statement	Parameter	Default	Units
MOBILITY	BN.CVT	4.75×10^7	cm/(a)
MOBILITY	BP.CVT	9.925×10^4	cm/(a)
MOBILITY	CN.CVT	1.74×10^5	
MOBILITY	BP.CVT	8.842×10^5	
MOBILITY	TAUN.CVT	0.125	
MOBILITY	TAUP.CVT	0.0317	
MOBILITY	GAMN.CVT	2.5	
MOBILITY	GAMP.CVT	2.2	
MOBILITY	MU0N.CVT	52.2	cm ² /(v-a)
MOBILITY	MU0P.CVT	44.9	cm ² /(v-a)
MOBILITY	MU1N.CVT	43.4	cm ² /(v-a)
MOBILITY	MU1P.CVT	29.0	cm ² /(v-a)
MOBILITY	MUMAXN.CVT	1417.0	cm ² /(v-a)
MOBILITY	MUMAXP.CVT	470.5	cm ² /(v-a)
MOBILITY	CRN.CVT	9.68×10^{14}	cm ⁻³
MOBILITY	CRP.CVT	2.23×10^{17}	cm ⁻³
MOBILITY	CSN.CVT	3.43×10^{20}	cm ⁻³
MOBILITY	CSP.CVT	6.10×10^{20}	cm ⁻³
MOBILITY	ALPHN.CVT	0.680	
MOBILITY	ALPHP.CVT	0.71	
MOBILITY	BETAN.CVT	2.00	
MOBILITY	BETAP.CVT	2.00	
MOBILITY	PCN.CVT	0.00	cm ⁻³
MOBILITY	PCP.CVT	0.23×10^{16}	cm ⁻³
MOBILITY	DELN.CVT	5.82×10^{14}	cm ⁻³

The model for carrier emission and absorption processes produced by Shockley-Read-Hall (SRH) is used to reflect the recombination phenomenon within the device. The electron and hole lifetimes τ_n & τ_p were modelled as concentration dependant. The equation is given by [11]:

$$R_{SRH} = \frac{pn - n_{ie}^2}{\tau_p \left[n + n_{ie} \exp\left(\frac{ETRAP}{kT_L}\right) \right] + \tau_n \left[p + n_{ie} \exp\left(\frac{-ETRAP}{kT_L}\right) \right]} \quad (2.8)$$

$$\tau_n = \frac{TAUN0}{1 + \left(\frac{N}{NSRHN}\right)} \quad (2.9)$$

$$\tau_p = \frac{TAUPO}{1 + \left(\frac{N}{NSRHP}\right)} \quad (2.10)$$

Here N is called the local (total) impurity concentration. The used parameters TAUN0, TAUPO, NSRHN and NSRHP are Table 2.2 [11]. This model was activated with the CONSRH parameter of the MODELS statement.

Table 2.2: Default Parameter for equations 2.8 to 2.10

Statement	Parameter	Default	Units
MATERIAL	TAUNO	1.0×10^{-7}	S
MATERIAL	NSRHN	5.0×10^{16}	cm^{-3}
MATERIAL	TAUPO	1.0×10^{-7}	S
MATERIAL	NSRHP	5.0×10^{16}	cm^{-3}

To account bandgap narrowing effects, BGN model was used. These effects may be described by an analytic expression relating the variation in bandgap, ΔE_g , to the doping concentration, N. The expression used in ATLAS is from Slotboom and de Graaff [11]:

The used values for the parameters BGN.E, BGN.N and BGN.C are shown in Table 2.3 [11]:

Table 2.3: Default Parameters of Slotbooms Bandgap Narrowing Model for equation 2.11

Statement	Parameter	Default	Units
MATERIAL	BGN.E	9.0×10^{16}	V
MATERIAL	BGN.N	1.0×10^{16}	cm^{-3}
MATERIAL	BGN.C	0.5	-

2.2 Simulation models for poly silicon nanowire

The 2D coupled Poisson's drift-diffusion solver with Fermi-Dirac (FERMI) carrier statistics was also used to model carrier transport in poly silicon NW. The Shockley-Read-Hall model for carrier emission and absorption was used to reflect the recombination phenomena within the device. Moreover, the band gap narrowing (BGN) effects in the heavily doped source/drain regions were included by Slotboom and de Graaff's analytical BGN model. However, for mobility we used constant mobility model for poly silicon NWS simulation because TFT module in ATLAS is compatible with constant low field mobility model only. Use of other mobility model overwrites constant low field model and gives inaccurate results. Constant low field mobility model is independent of doping concentration, carrier densities and electric field. It does account for lattice scattering due to temperature according to:

$$\mu_{n0} = \text{MUN} \left(\frac{T_L}{300}\right)^{-\text{TMUN}} \quad (3.1)$$

$$\mu_{p0} = \text{MUP} \left(\frac{T_L}{300}\right)^{-\text{TMUP}} \quad (3.2)$$

Where T is the lattice temperature. The low field mobility parameters: MUN, MUP, TMUN and TMUP can be specified in the MOBILITY statement with the defaults as shown in Table 2.4.

Table 2.4: Default mobility model values for polysilicon

Statement	Parameter	Default	Unit
MOBILITY	MUN	1000	$\text{cm}^2/\text{V.s}$
MOBILITY	MUP	500	$\text{cm}^2/\text{V.s}$
MOBILITY	TMUN	1.5	-
MOBILITY	TMUP	1.5	-

However we have used $MUN=14\text{cm}^2/\text{V.s}$ and $MUP=6\text{cm}^2/\text{V.s}$ as experimentally extracted mobility of similar polysilicon nanowires were within the range of $6\text{cm}^2/\text{V.s}$ to $12\text{cm}^2/\text{V.s}$ considering variation of polysilicon nanowire width and height after fabrication.

Poly silicon is a disorder material which contains a large number of defects states within the band gap of the material and interface. The defect states as a combination of exponentially decaying band tail states and Gaussian distribution of mid gap states [11] shown in Figure 3.2. We therefore model the poly silicon using a continuum of trap states consist of both donor-like and acceptor-like states distribution across the energy band gap. The defect states as a combination of exponentially decaying band Tail states and Gaussian distribution of mid gap states are used with parameters previously used in the literature for successful modelling of poly silicon thin film transistor [12].

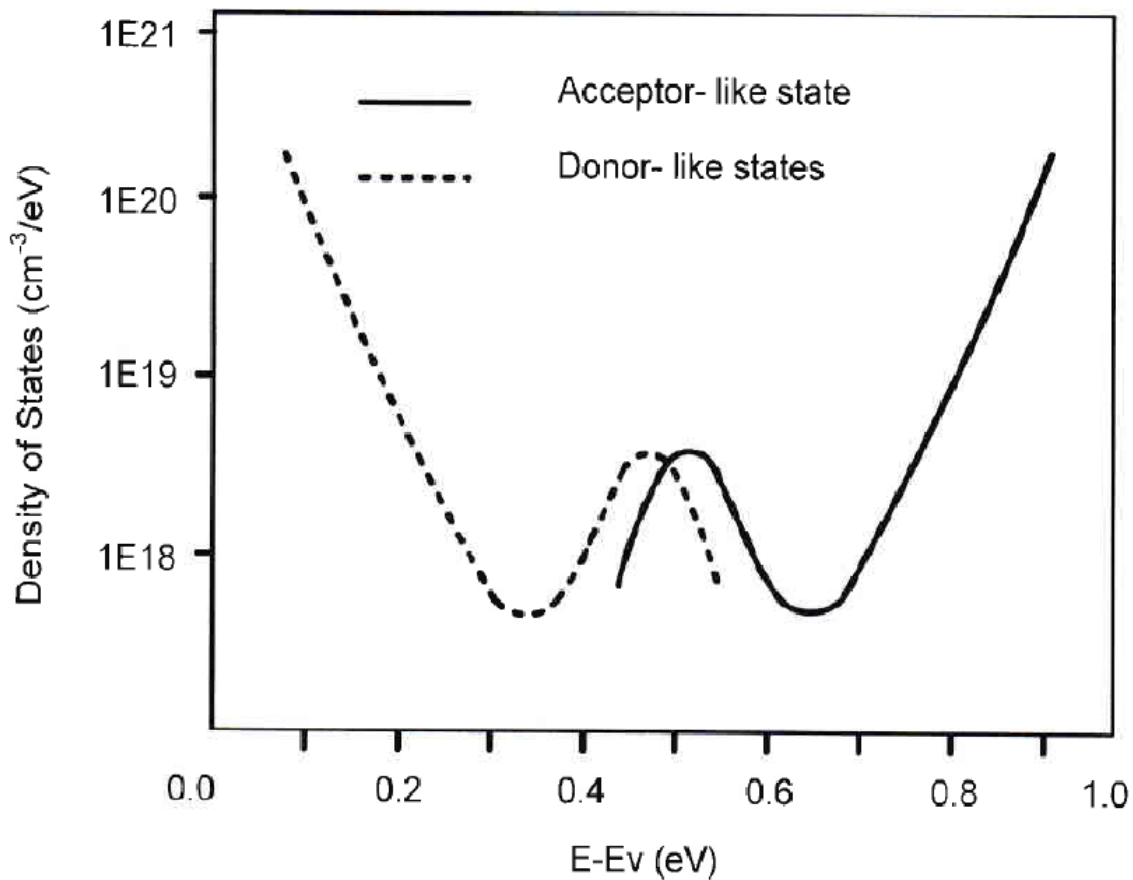


Figure 2.2: The distribution of acceptor and donor-like trap states across forbidden energy gap.

2.3 Simulation profile

Device simulation using SILVACO Atlas usually faces convergence problems and necessitates a long simulation run times. To avoid these problems, the simulation of silicon nanowire MOSFET has been divided into a few groups. At first, structure definition was performed. In this definition the simulation focused on creating the structure with a suitable mesh density. Regions and electrodes were defined as depicted in Figure 2.3. Finer nodes were assigned in critical areas, such as across the gate oxide to monitor channel activity and to get a better picture

of the depletion layer and junction behavior near the source/drain boundaries. A coarser mesh was used elsewhere in order to reduce simulation run time.

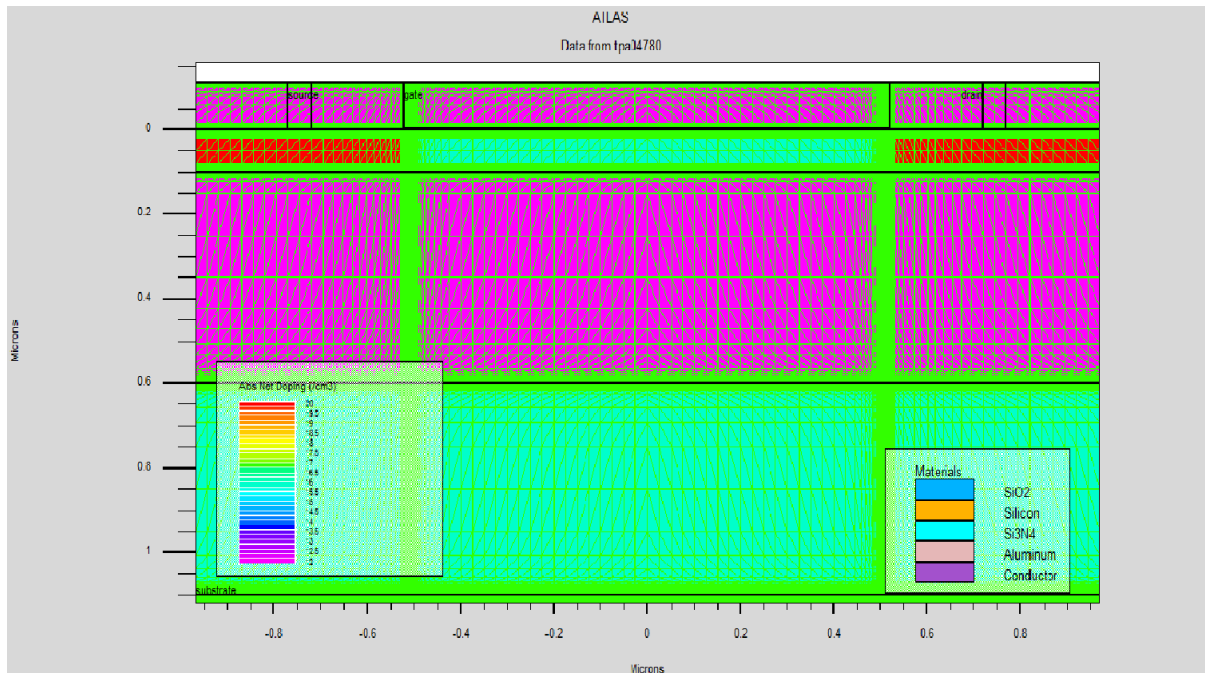


Figure 2.3: Cross-sectional view of p-type nanowire showing the mesh density used in this simulation

Once the structure and the mesh were found to be as desired, the simulation was performed with appropriate models as discussed in section 2.1 and numerical solving methods. The model was invoked by using the statements FERMI, CVT, CONSRH, BGN. The numerical solving methods GUMMEL, NEWTON were used to reduce the simulation run time, while keeping the accuracy of the simulation at an acceptable level.

To get convergence, a special bias point solving method was used. It was found that the simulation faced difficulty in solving the initial desired bias points i.e. $\pm 1V$, $\pm 2V$, $\pm 3V$, $\pm 4V$, $\pm 5V$ for back gate voltage $\pm 1V$ for drain voltage. Therefore, the initial gate bias was set to $0.005V$ and the next bias point was set to $0.05V$, before finally setting the bias point to desired value.

Chapter 3

Results and Discussion:

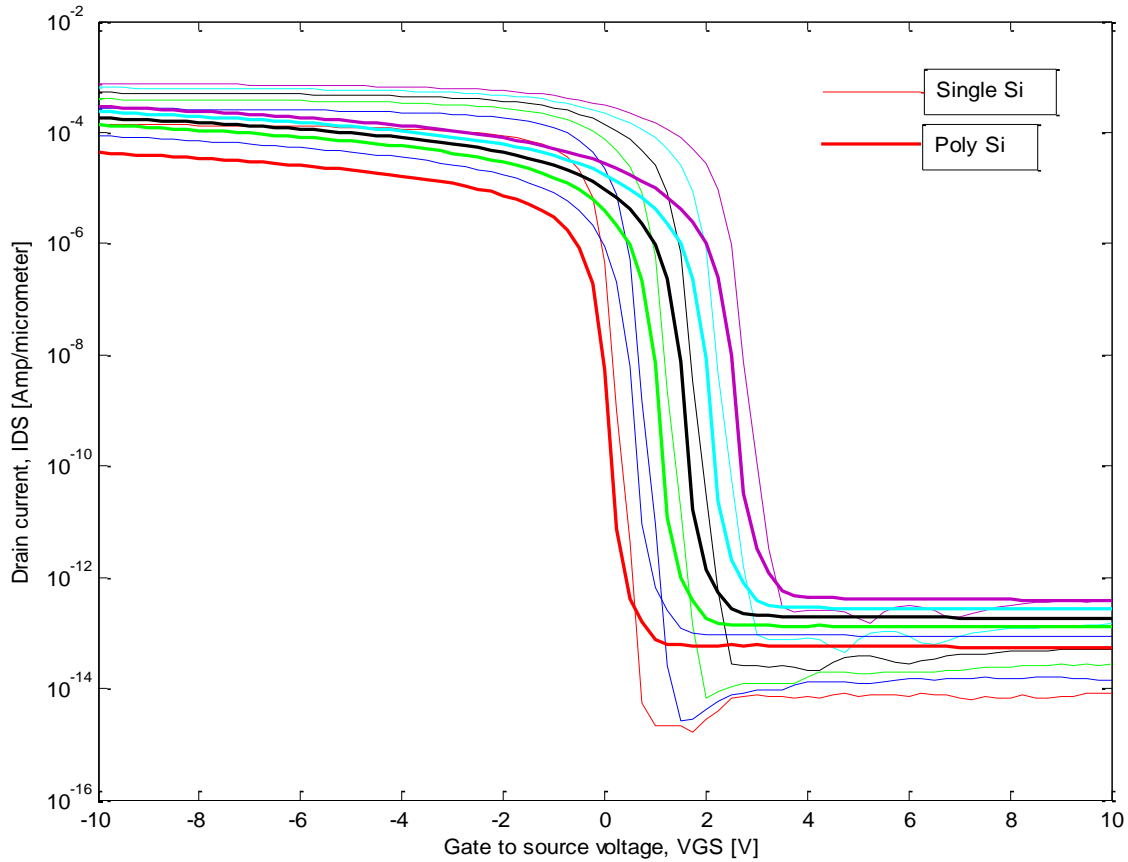


Figure 3.1: Sub-threshold characteristics of p-type Silicon nanowires with $10^{16}/\text{cm}^3$ doping concentration at 100nm thickness; single crystal Si and poly crystal Si. The NWs have channel length of $1\mu\text{m}$.

Figure 3.1 shows sub-threshold characteristics (I_{DS} vs V_{GS}) of p-type (single crystal and poly crystal) Si NWs for 100nm nanowire thickness. The length of the nanowire is $1\mu\text{m}$ and doping density is $10^{16}/\text{cm}^3$. For single crystal Si in Figure 3.1, the sub-threshold slope is found to be 105mV/decade. The drive current of single crystal Si NW is found to be $1.23 \times 10^{-4} \text{A}/\mu\text{m}$ at $V_{DS} = 0.5\text{V}$ and $V_{GS} = -5\text{V}$. For poly Si NW sub threshold slope S is found to be 113mv/decade. The sub threshold slope of $1\mu\text{m}$ long 100nm thick poly Si NW is inferior to that of the single crystal Si NW. The drive current is also lower than single crystal Si NW with a value of $2.11 \times 10^{-5} \text{A}/\mu\text{m}$ at $V_{DS} = 0.5\text{V}$ and $V_{GS} = -5\text{V}$. Although the exhibited value of sub threshold slope is higher than ideal 60mV/decade; a sub-threshold swing around $\approx 100\text{mv}/\text{decade}$ is fair for using both poly Si and single crystal Si NW as sensors with slightly degraded performances for poly Si case.

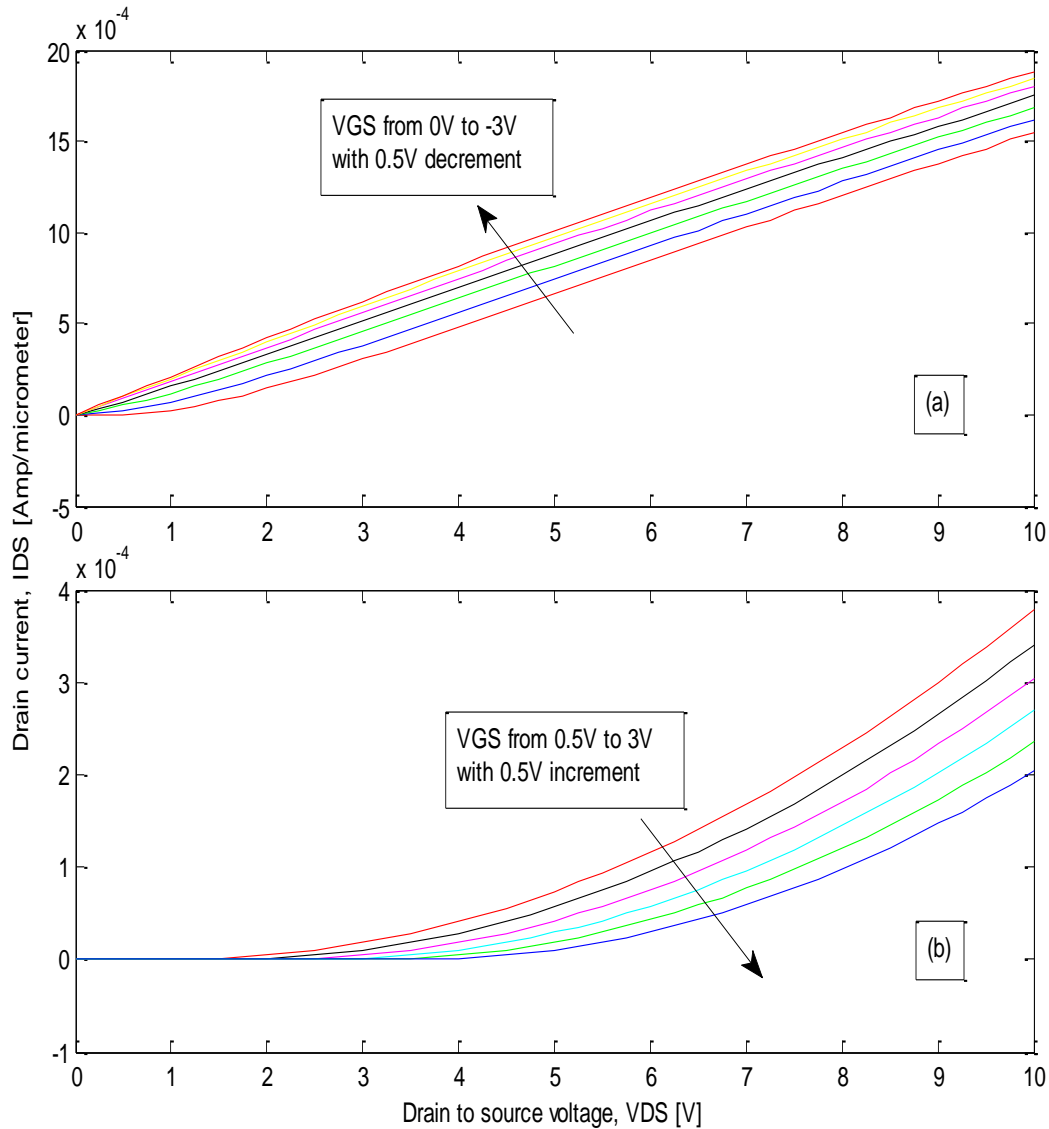


Figure 3.2: Output characteristics of p-type Silicon nanowires with $10^{16}/\text{cm}^3$ doping concentration at 100nm thickness; (a) single crystal Si and (b) poly crystal Si. The NWs have channel length of $1\mu\text{m}$.

Figure 3.2 shows output characteristics (I_{DS} vs. V_{DS}) of $1\mu\text{m}$ long p-type (single crystal and poly crystal) silicon nanowires for 100nm thickness while the doping density is $10^{16}/\text{cm}^3$. For single crystal Si NW a typical non-linear characteristics is observed with insignificant conduction up to certain level of drain bias. With the application of negative V_{GS} this non-linear characteristics is reduced and drive current increases. The increase in drive current can be explained by the modulation of NW conduction due to strong hole accumulation upon application of negative V_{GS} . For poly Si NW the non-linearity of I_{DS} - V_{DS} characteristics is significantly increased. In particular the NWs drive current significantly lower and the NWs do not show significant conduction up to 2V of V_{DS} where is much higher than single crystal Si NW which has a value of 0.5V.

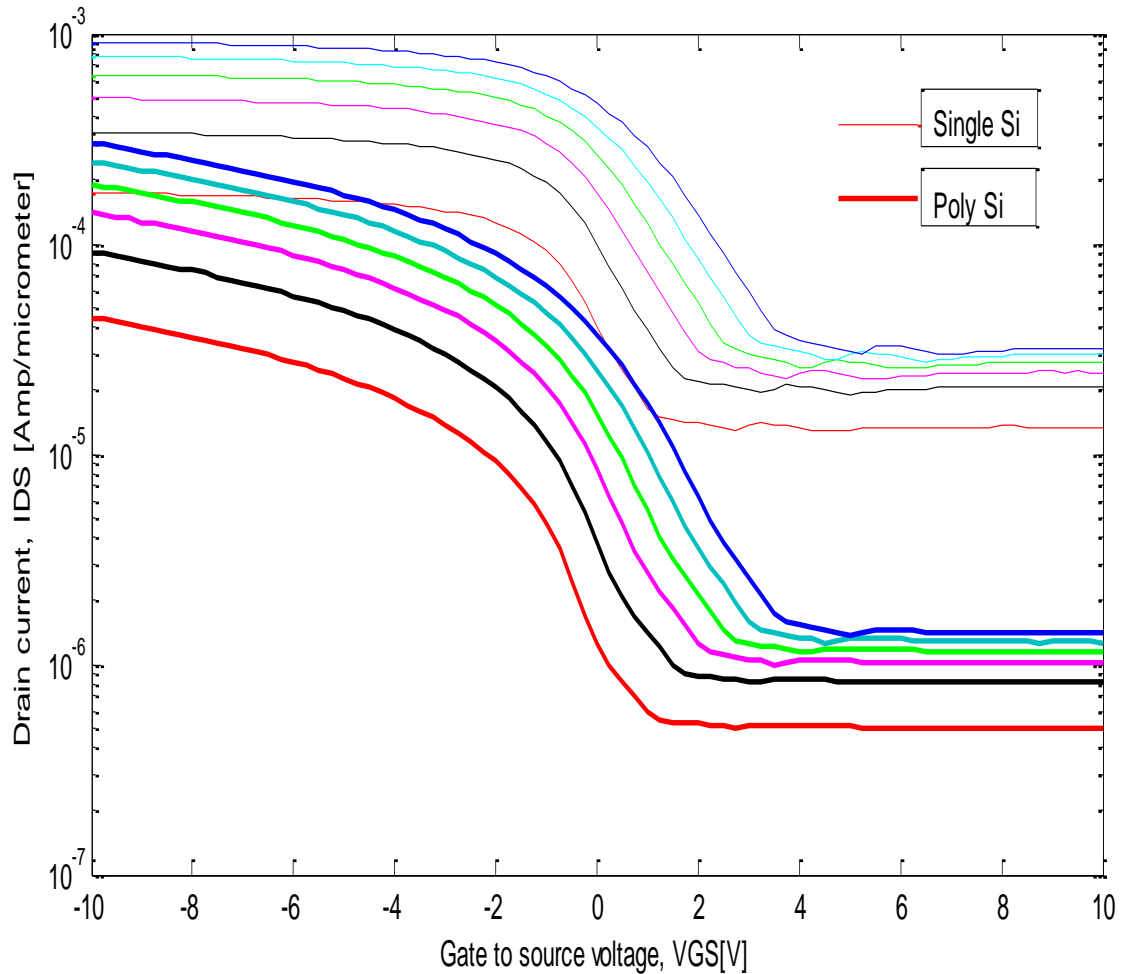


Figure 3.3: Sub-threshold characteristics of p-type Silicon nanowires with $4 \times 10^{17}/\text{cm}^3$ doping concentration at 100nm thickness; single crystal Si and poly crystal Si. The NWs have channel length of $1 \mu\text{m}$.

Figure 3.3 shows sub-threshold characteristics (I_{DS} vs. V_{GS}) of p-type (single crystal and poly crystal) Si NWs for 100nm nanowire thickness. The length of the nanowire is $1 \mu\text{m}$ and doping density is $4 \times 10^{17}/\text{cm}^3$. For single crystal Si in Figure 3.3, the sub-threshold slope is found to be 2420mV/decade. And for the poly crystal Si in Figure 3.3, the sub-threshold slope is found to be 2530mV/decade. These drastically inferior sub-threshold characteristics render 100nm thick single and poly-silicon nanowires with a doping density $4 \times 10^{17}/\text{cm}^3$ unsuitable for a viable biosensor operation. Although the sub-threshold slope of single crystal Si is lower than the poly crystal Si, both have very high values of slopes than the ideal value. This observation implies that both single and poly crystal Si nanowire cannot be used as sensor with a doping density of $4 \times 10^{17}/\text{cm}^3$. The drive current of single crystal Si NW is $1.6 \times 10^{-4} \text{A}/\mu\text{m}$ at $V_{GS} = -5\text{V}$ and $V_{DS} = 0.5\text{V}$. This current is again higher than poly Si NW which has a value of $2.27 \times 10^{-5} \text{A}/\mu\text{m}$ at this biasing condition.

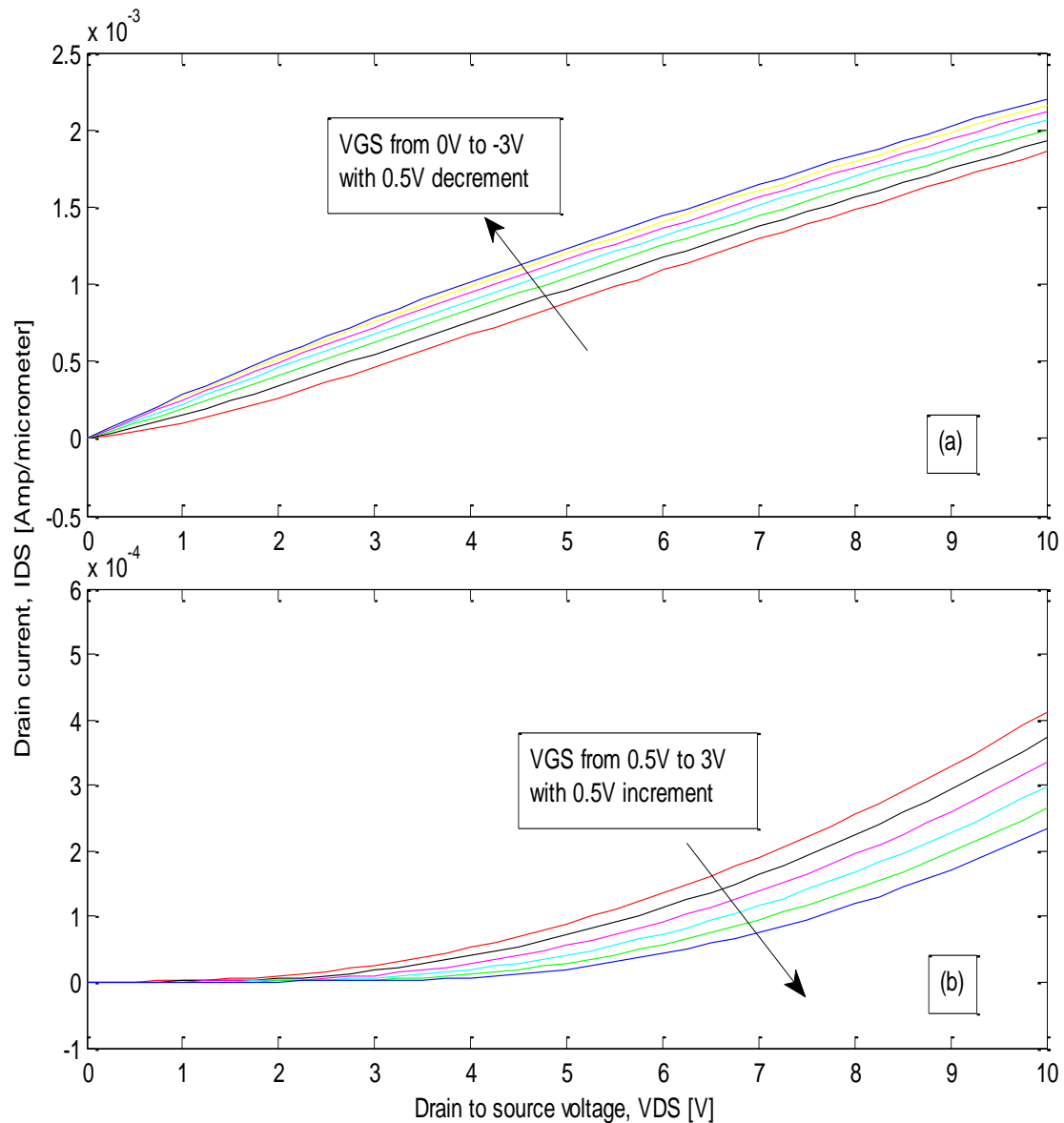


Figure 3.4: Output characteristics of p-type Silicon nanowires with $4 \times 10^{17}/\text{cm}^3$ doping concentration at 100nm thickness; (a) single crystal Si and (b) poly crystal Si. The NWs have channel length of $1\mu\text{m}$.

Figure 3.4 shows output characteristics (I_{DS} vs. V_{DS}) of $1\mu\text{m}$ long p-type (single crystal and poly crystal) silicon nanowires for 100nm thickness while the doping density is $4 \times 10^{17}/\text{cm}^3$. For single crystal Si NW, the characteristics is more linear at this doping density in comparisons to the doping of $10^{16}/\text{cm}^3$ and the typical (Figure 3.2(a)) non-conduction region is also disappears. However, for poly Si NW the characteristics is still non-linear with an insignificant conduction up to a $V_{DS} = 2\text{V}$. The drive current of poly Si NW is inferior to single crystal Si NW. However both single crystal Si and poly Si NW at this doping exhibit higher drive current than $10^{16}/\text{cm}^3$ doping density (Figure 3.2).

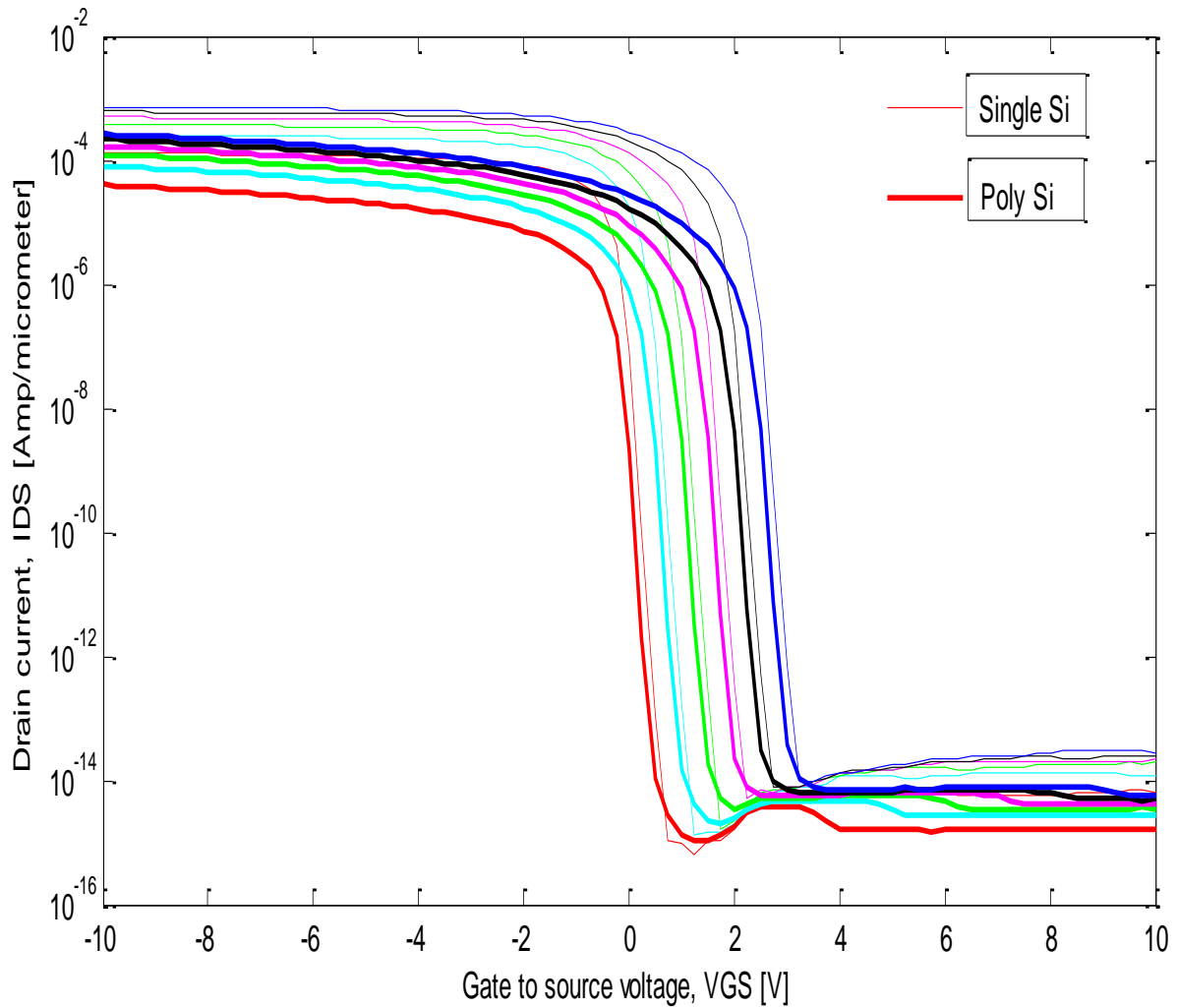


Figure 3.5: Sub-threshold characteristics of p-type Silicon nanowires with $10^{16}/\text{cm}^3$ doping concentration at 25nm thickness; single crystal Si and poly crystal Si. The NWs have channel length of $1\mu\text{m}$.

Figure 3.5 shows sub-threshold characteristics (I_{DS} vs. V_{GS}) of p-type (single crystal and poly crystal) Si NWs for 25nm nanowire thickness. The length of the nanowire is $1\mu\text{m}$ and doping density is $10^{16}/\text{cm}^3$. For single crystal Si in Figure 3.5, the sub-threshold slope is found to be 86.1 mV/decade which is noticeably better than the 100nm thick single crystal Si NW at doping of $10^{16}/\text{cm}^3$. The drive current of single crystal Si NW is $1.14 \times 10^{-4} \text{A}/\mu\text{m}$ at $V_{DS} = 0.5\text{V}$ and $V_{GS} = -5\text{V}$ which is lower than 100nm thick single crystal Si NW at this doping (Figure 3.1). For poly Si sub threshold slope is 103mV/decade which inferior than single crystal Si NW at this doping. However, poly Si NWs sub-threshold slope at 25nm thickness is found to be improved in comparison the 100nm thickness (Figure 3.1).

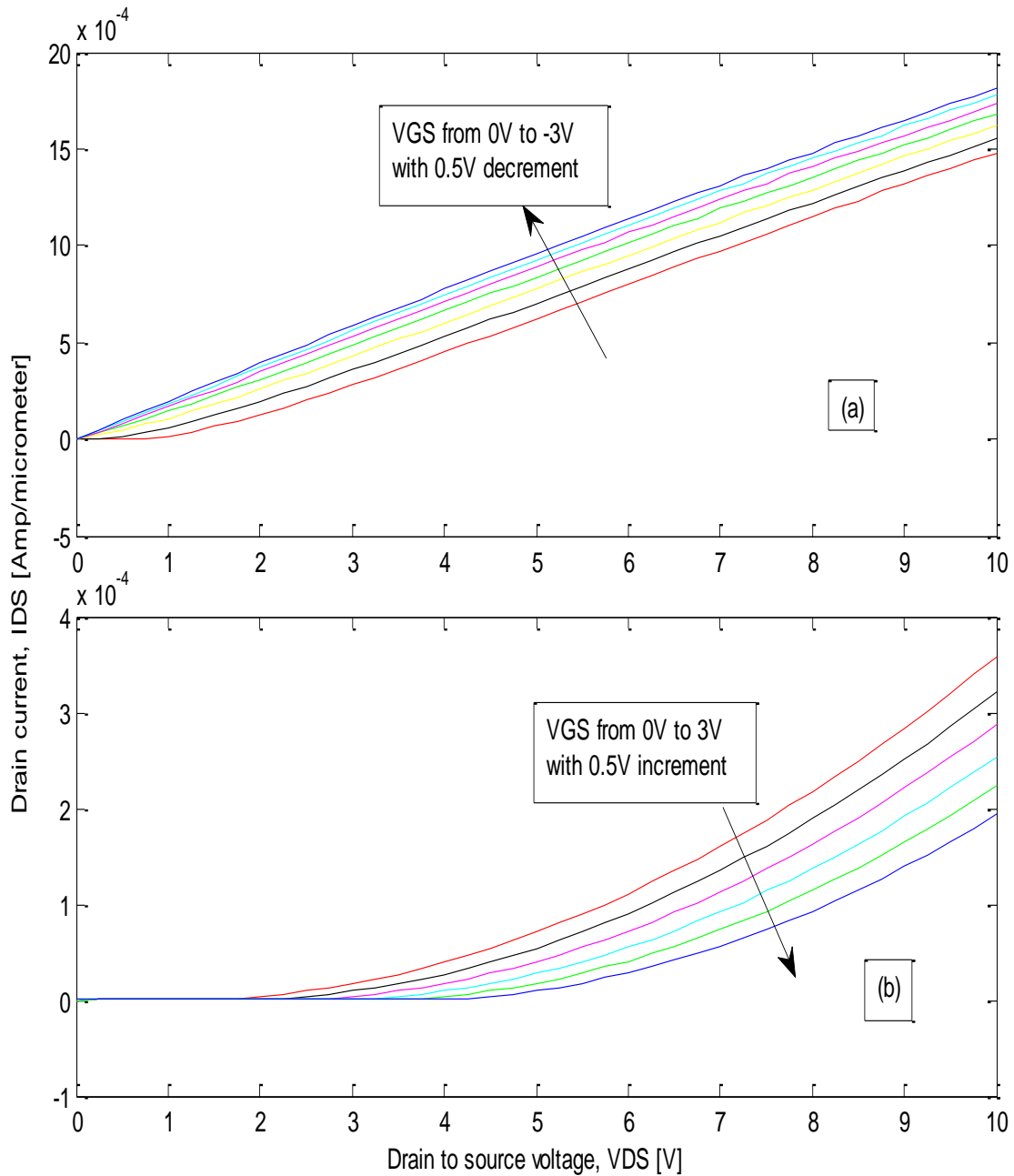


Figure 3.6: Output characteristics of p-type Silicon nanowires with $10^{16}/\text{cm}^3$ doping concentration at 25nm thickness; (a) single crystal Si and (b) poly crystal Si. The NWs have channel length of $1\mu\text{m}$.

Figure 3.6: shows output characteristics (I_{DS} vs. V_{DS}) of $1\mu\text{m}$ long p-type (single crystal and poly crystal) silicon nanowires for 25nm thickness while the doping density is $10^{16}/\text{cm}^3$. For single crystal Si NW the output characteristics at 25nm thickness and $10^{16}/\text{cm}^3$ doping is similar to that of 100nm thick NW at this doping. However the drive current of poly Si NW at 25nm thickness is lower than 100nm thickness. For poly Si NW (Figure 3.6(b)) the characteristics is again more non-linear than single crystal Si NW which is similar to the observations of NW's output characteristics at doping $10^{16}/\text{cm}^3$ and 100nm thickness.

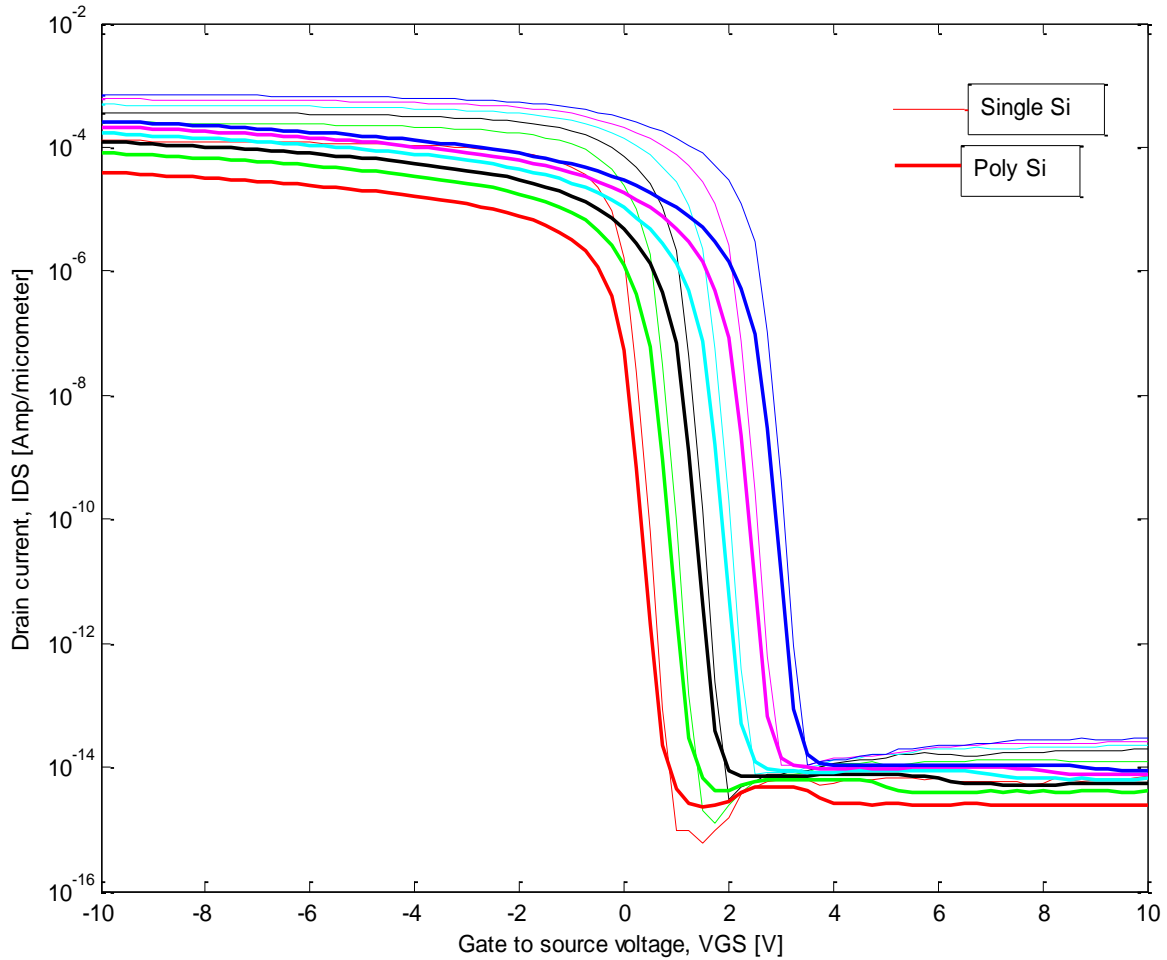


Figure 3.7: Sub-threshold characteristics of p-type Silicon nanowires with $4 \times 10^{17}/\text{cm}^3$ doping concentration at 25nm thickness; single crystal Si and poly crystal Si. The NWs have channel length of $1 \mu\text{m}$.

Figure 3.7 shows sub-threshold characteristics (I_{DS} vs. V_{GS}) of p-type (single crystal and poly crystal) Si NWs for 25nm nanowire thickness. The length of the nanowire is $1 \mu\text{m}$ and doping density is $4 \times 10^{17}/\text{cm}^3$. A drastic change in the NW characteristics can be observed for 25nm thick Si NW at thus doping density in comparison to 100nm thick NW (Figure 3.3). While 100nm thick NW at doping of $4 \times 10^{17}/\text{cm}^3$ exhibited significantly unsuitable sub-threshold slope value offer sensor operation both single crystal poly Si NW at 25nm thickness exhibited significantly improved sub-threshold slope value at doping of $4 \times 10^{17}/\text{cm}^3$. The sub threshold slope of single crystal and poly crystal Si NWs are 97.9mV/decade and 118mV/decade respectively which is much better than 100nm thick NW's at this doping (Figure 3.3). It should also be noted that the drive current of poly/single crystal NWs at this doping is higher than $10^{16}/\text{cm}^3$ doping.

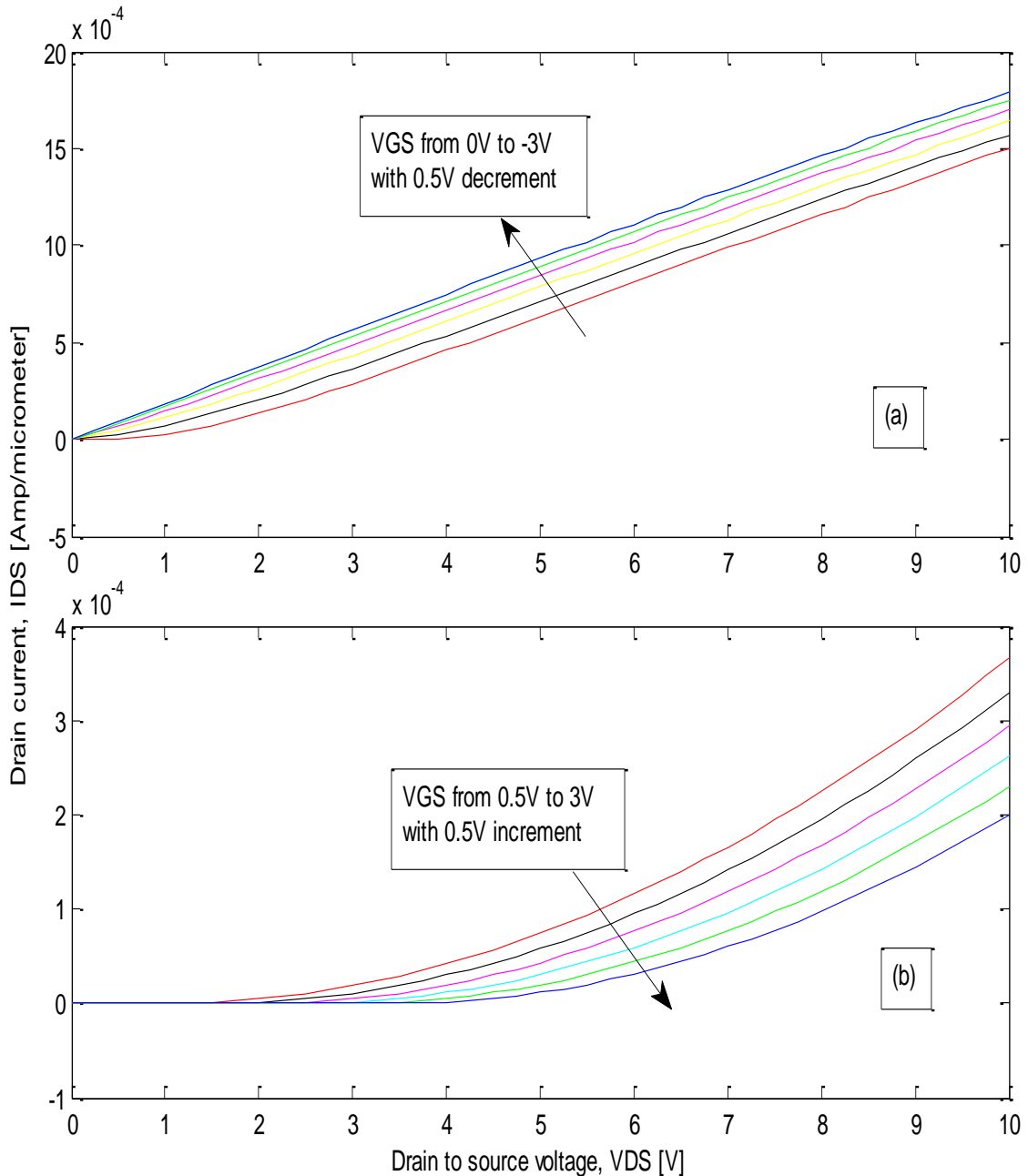


Figure 3.8: Output characteristics of p-type Silicon nanowires with $4 \times 10^{17}/\text{cm}^3$ doping concentration at 25nm thickness; (a) single crystal Si and (b) poly crystal Si. The NWs have channel length of $1\mu\text{m}$.

Figure 3.8 shows output characteristics (I_{DS} vs. V_{DS}) of $1\mu\text{m}$ long p-type (single crystal and poly crystal) silicon nanowires for 25nm thickness while the doping density is $4 \times 10^{17}/\text{cm}^3$. The exhibited output characteristics are similar to the output characteristics observed previously for 100nm NW thickness at this doping. Except that the drive current is lower than 100nm thick NW's at this doping (Figure 3.4).

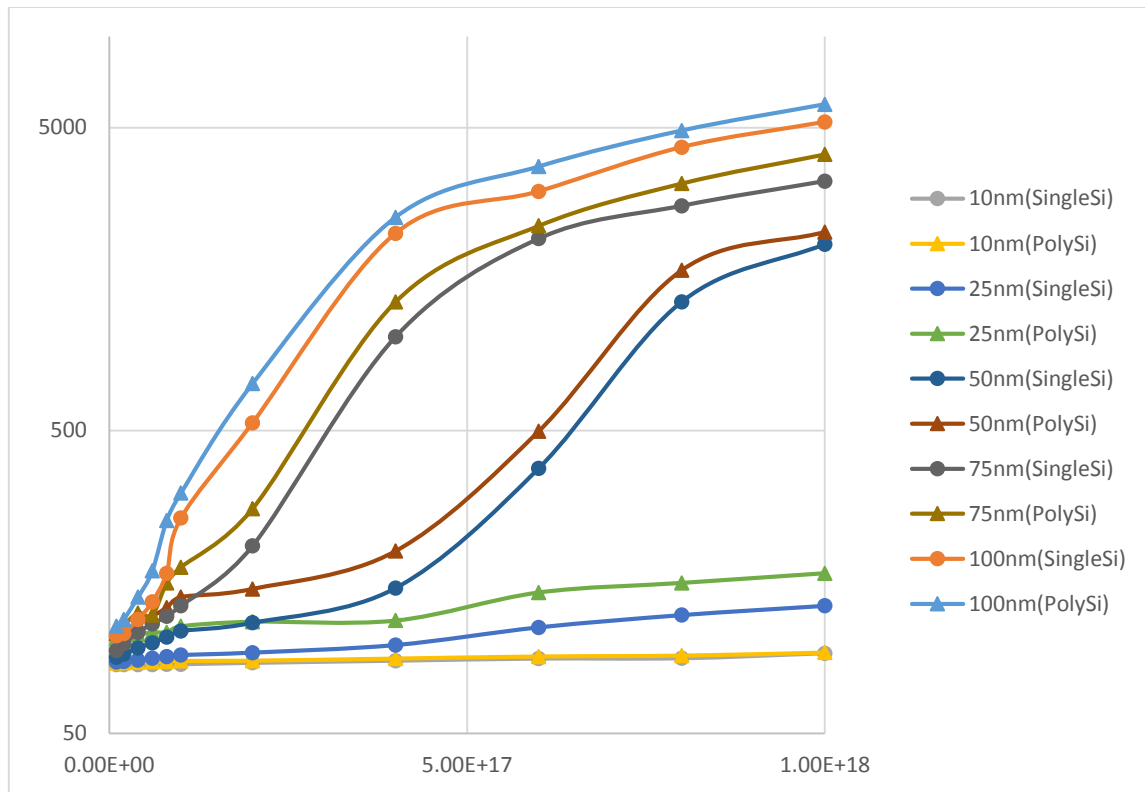


Figure 3.9: Sub-threshold slopes as a function of doping concentrations for different thicknesses of single crystal Silicon and poly crystal Silicon nanowires

Figure 3.9 summarizes the extracted values of sub-threshold slopes as a function of doping concentrations for different thicknesses & for single crystal Silicon / poly crystal Silicon nanowires. It can be seen that poly Si NW generally shows inferior characteristics than single crystal Si NW of all doping densities for NW thicknesses of 100, 75, 50 & 25nm which agrees well with general believe that poly Si NW will give inferior sensor performance than single crystal Si NW. However, for 10nm Si NW single crystal & poly Si NW show same sub-threshold slopes at all doping densities. Considering the fact that spacer etch process provides the cheapest & mass manufacturable platform for biosensor fabrication using poly Si material in comparison to the available single crystal platforms. It can be decided from this work that poly Si NW biosensor with Si thickness $\leq 10\text{nm}$ is the possible commercial route of sensor fabrication. Figure 3.9 also elucidates the proper combination of nanowire thickness and doping to ensure the sensitive operation of single crystal and polycrystalline silicon nanowire biosensors. For nanowire thickness of 100nm and 75nm, a severely degraded sub threshold slope can be observed when doping concentrations are above $10^{17} / \text{cm}^3$ both for single crystal and poly Si nanowires. The polysilicon nanowires exhibit sub-threshold slopes of 5970mV/decade and 4080mV/decade respectively for 100nm and 75nm nanowire thickness at the doping concentration of $10^{18} / \text{cm}^3$. A plausible sub-threshold slope of the single crystal Si NWs exhibit sub-threshold slopes of 5220mV/decade and 3330mV/decade respectively for 100nm and 75nm nanowire thickness at a doping concentration of $10^{18} / \text{cm}^3$. A plausible sub-threshold slope around 100 mV/decade for a viable biosensor operation at these thickness can only be achieve if doping concentration is $2 \times 10^{16} / \text{cm}^3$ or below both for single crystal and poly silicon nanowires. For a 50nm nanowire thickness a relatively wide doping concentration range

can be chosen for biosensor design while maintaining decent sub-threshold characteristics. In this thickness a doping up to $4 \times 10^{17}/\text{cm}^3$ with a sub-threshold slope around 100 mV/decade can be chosen. The widest range of doping concentrations can be chosen for 25nm and 10nm nanowire thickness with a maximum doping up to $10^{18}/\text{cm}^3$ while maintaining a promising sub-threshold slope around 95mV/decade for a viable biosensor design using both single and polycrystalline silicon nanowires.

Chapter 4

Conclusion

We have investigated the effect of nanowire thickness and doping concentration on the electrical characteristics of single crystal and polycrystalline silicon nanowire biosensors. For nanowire thicknesses of 100 nm and 75 nm, a plausible sub-threshold slope around 100 mV/decade for a viable biosensor operation can only be achieved if doping concentration is $2 \times 10^{16}/\text{cm}^3$ or below both for single crystal and poly Si nanowires. For a 50nm nanowire thickness a relatively wide doping concentration range with a maximum doping up to $4 \times 10^{17}/\text{cm}^3$ can be chosen for biosensor design while maintaining decent sub-threshold characteristics. The widest range of doping concentrations can be chosen for 25nm and 10nm nanowire thickness with a maximum doping up to $10^{18}/\text{cm}^3$ while maintaining a promising sub-threshold slope around 95 mV/decade for a viable biosensor design using single crystal and polycrystalline silicon nanowires. In general poly Si NW shows inferior characteristics than single crystal Si NW. However, for 10nm Si NW single crystal & poly Si NW show same sub-threshold slopes at all doping densities. Considering the fact that spacer etch process provides the cheapest & mass manufacturable platform for biosensor fabrication using poly Si material in comparison to the available single crystal platforms. It can be decided from this work that poly Si NW biosensor with Si thickness $\leq 10\text{nm}$ is the possible commercial route of sensor fabrication.

References

1. H. Lee, J. Hong, S. Lee, S. D. Kim, Y. W. Kim, and T. Lee, "Selectively grown vertical silicon nanowire p-n+ photodiodes via aqueous electroless etching," *Applied Surface Science*, vol. 274, pp. 79-84, 2013.
2. F. Patolsky, G. Zheng and C.M. Lieber, "Nanowire-Based Biosensors," *Anal. Chem.* Vol. 78, pp. 4260-4269, 2006.
3. Songyue Chen, "Silicon Nanowire Field-effect Sensor," chapter 2, *Wohrmann Print Service*.
4. J. I. Abdul Rashid, J. Abdullah, Nor A. Yusof, R. Hajian, "The development of silicon nanowire as sensing material and its applications," *Journal of Nanomaterials*, Article ID 328093, pp. 02, 2013.
5. H. C. Lin, M. H. Lee, C. J. Su, T. Y. Huang, C. C. Lee and Y. S. Yang, "A simple and low-cost method to fabricate TFTs with poly-si nanowire channel," *IEEE Electron Device Lett.*, vol. 26, pp. 643-645, 2005.
6. L. P. Poly, Md. A. Haque and M. M. A. Hakim, "An investigation of the effects of doping and thickness on the electrical characteristics of polycrystalline silicon nanowire biosensors," *IEEE*, 2016.
7. M. M. A. Hakim, M. Lombardini, K. Sun, F. Giustiniano, P. L. Roach, D. E. Davies, P. H. Howarth, M. R. R. de Planque, H. Morgan, P. Ashburn, "Thin film polycrystalline silicon nanowire biosensors," *Nano Letters*, vol. 12, pp. 1868-1872, 2012.
8. W. Heywang, K. H. Zaininger, "Silicon: the semiconductor material", in *silicon: evolution and future of a technology*, P. Siffert, E. F. Krimmel eds., Springer Verlag, pp 25-42, 2004
9. J. P. Colinge, Chi-Woo Lee, A. Afzalian, N. D. Akhavan, R. Yan, I. Ferain, P. Razavi, B. O'Neill, A. Blake, M. White, A. M. Kelleher, B. McCarthy, R. Murphy, "Nanowire transistors without junctions," *Nature nanotechnology*, 2010.
10. Y. Cui, Q. Wei, H. Park and C. M. Lieber, "Nanowire and Nano sensor for highly sensitive and selective detection of biological and Chemical species," *Science*, vol. 293, pp. 1289-1292, 2001.
11. *Silvaco international, Atlas User's Manual Device Simulation Software*, Silvaco International Ltd., Santa Clara, Apr 2010.
12. P. Walker, H. Mizuta, S. Uno, Y. Furuta and D. Hasko, "Improved off-current and subthreshold slope in aggressively scaled poly-Si TFTs with single grain boundary in the channel", *IEEE Trans. On Electron Devices*, vol. 51, pp. 212-219, 2004.

Chapter 5

Appendix A

Single Crystal Silicon Nanowire

1. $1e16/cm^3$

NW thickness 10nm:

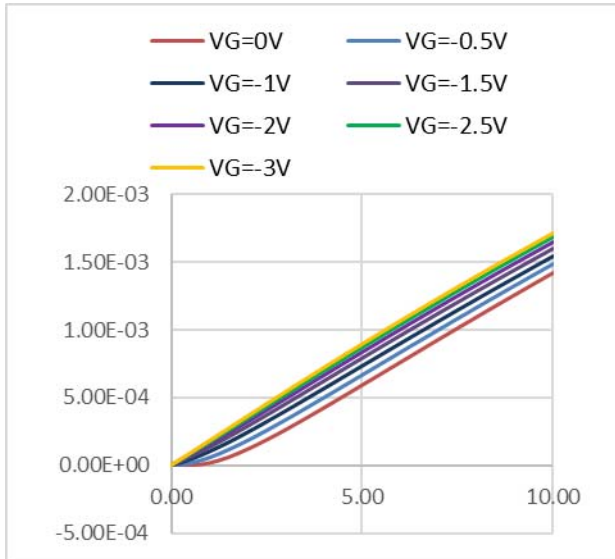


Fig.01: I_{ds} vs V_{ds} curves

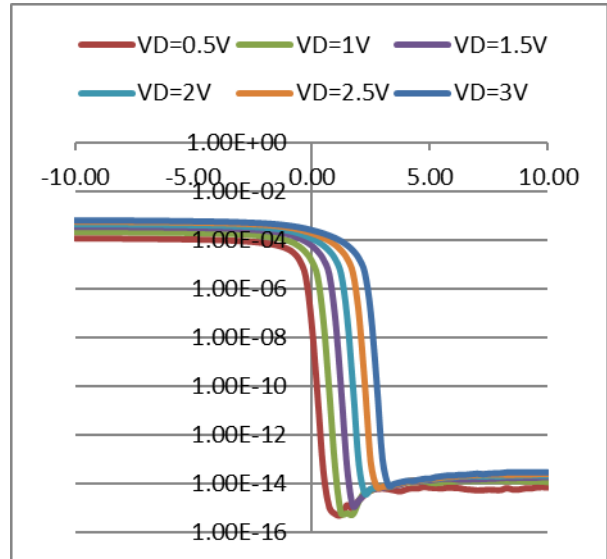


Fig.02: I_{ds} vs V_{gs} curves

NW thickness 25nm:

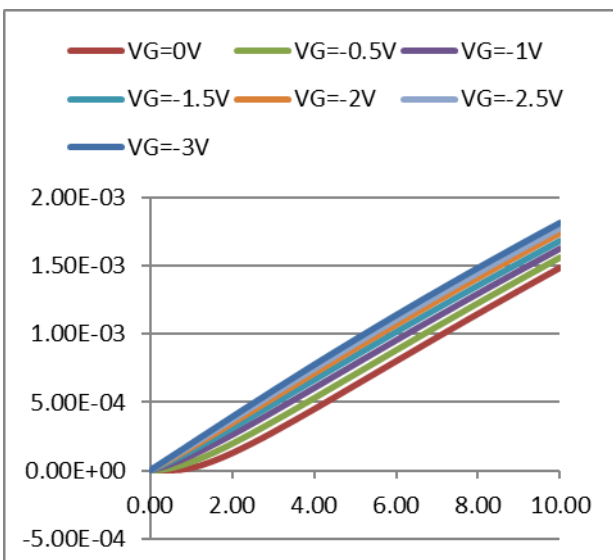


Fig.03: I_{ds} vs V_{ds} curves

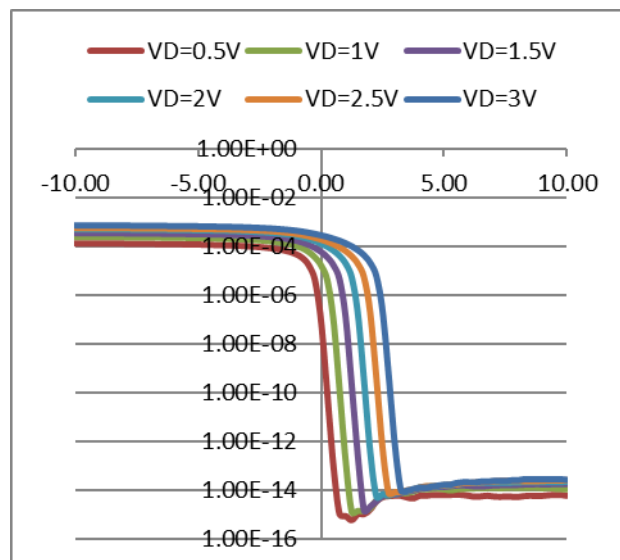


Fig.04: I_{ds} vs V_{gs} curves

NW thickness 50nm:

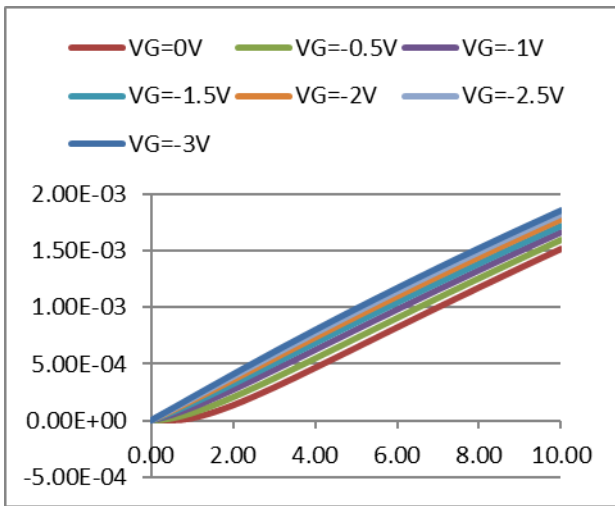


Fig.05: Ids vs Vds curves

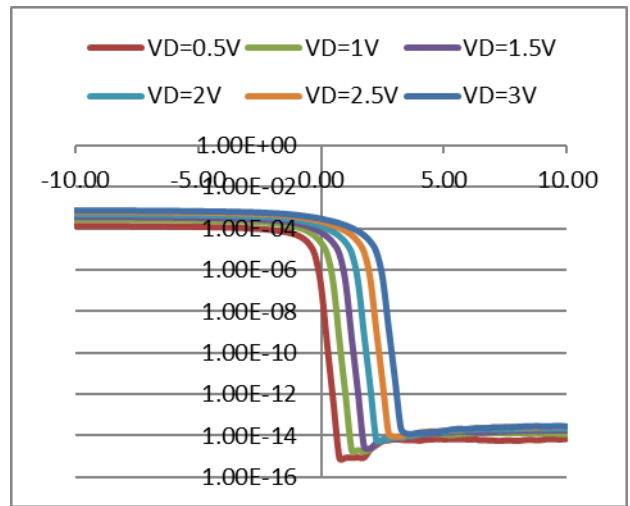


Fig.06: Ids vs Vgs curves

NW thickness 75nm:

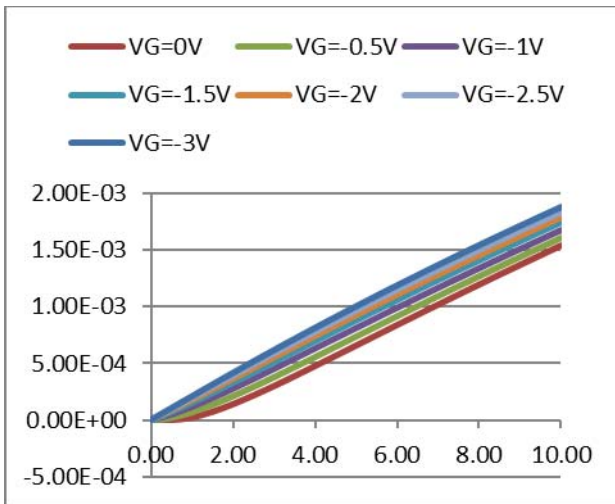


Fig.07: Ids vs Vds curves

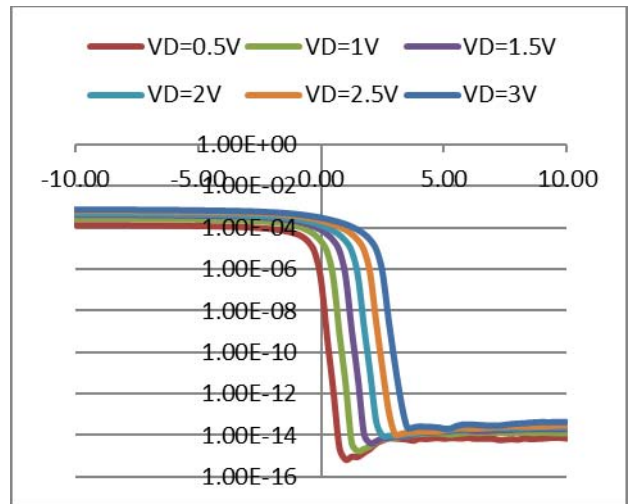


Fig.08: Ids vs Vgs curves

NW thickness 100nm:

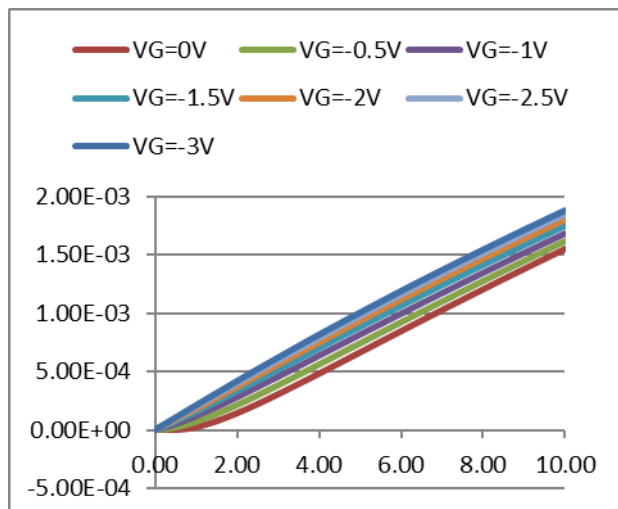


Fig.09: Ids vs Vds curves

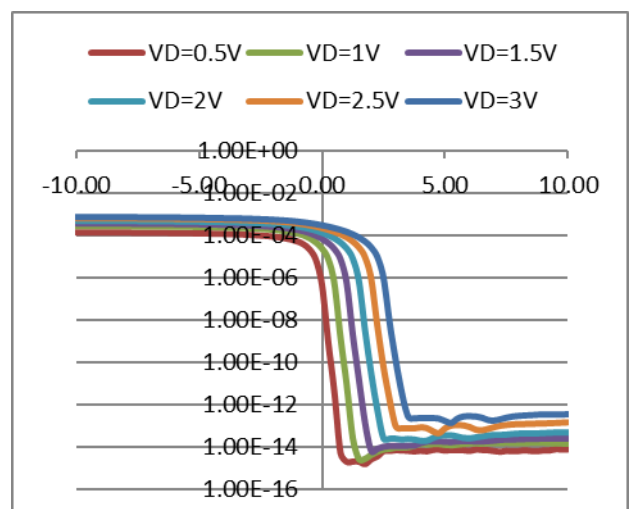


Fig.10: Ids vs Vgs curves

2. $2e16/cm^3$

NW thickness 10nm:

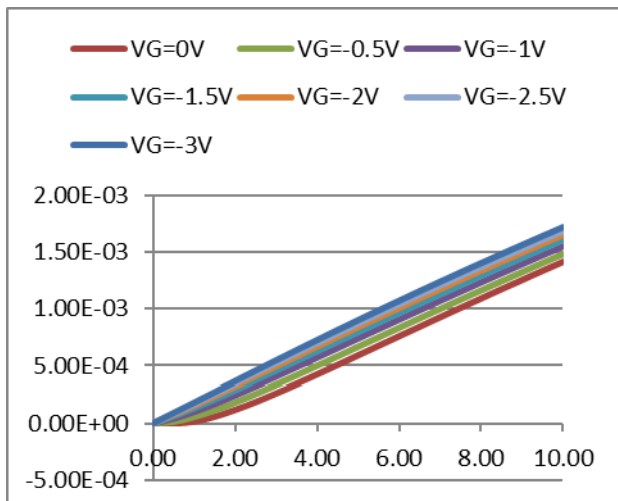


Fig.11: Ids vs Vds curves

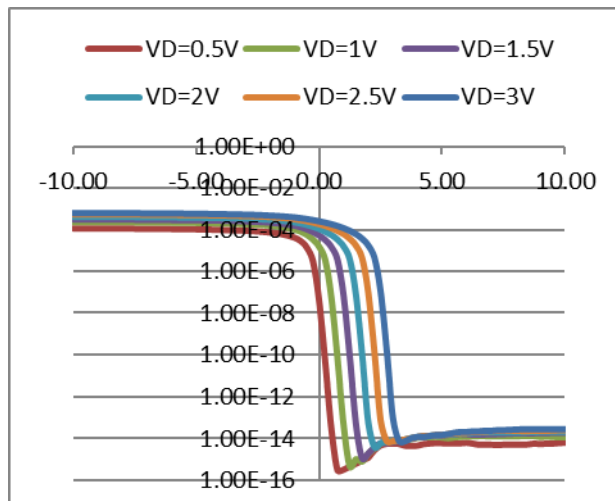


Fig.12: Ids vs Vgs curves

NW thickness 25nm:

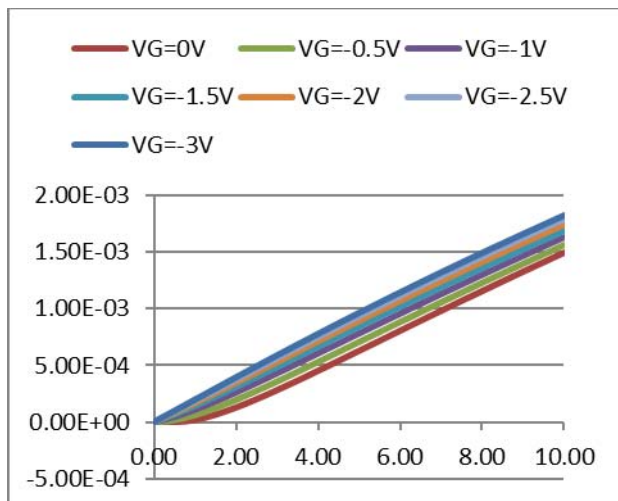


Fig.13: Ids vs Vds curves

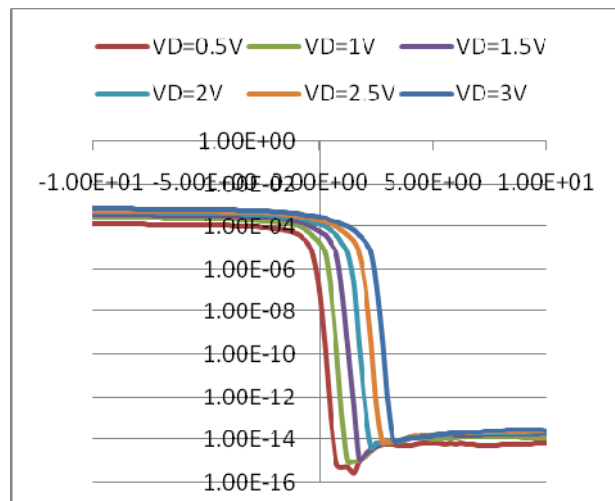


Fig.14: Ids vs Vgs curves

NW thickness 50nm:

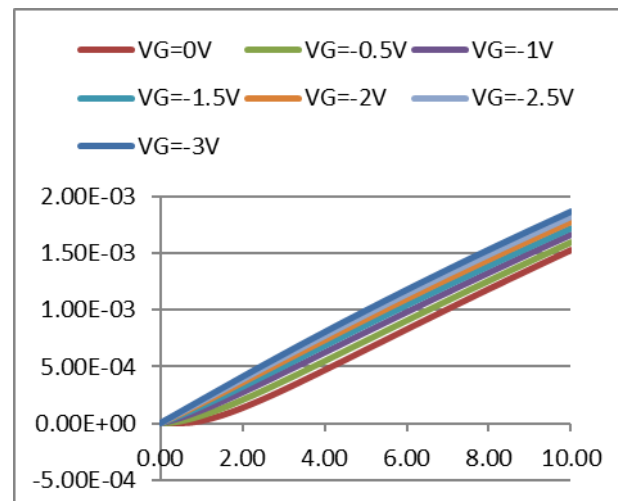


Fig.15: Ids vs Vds curves

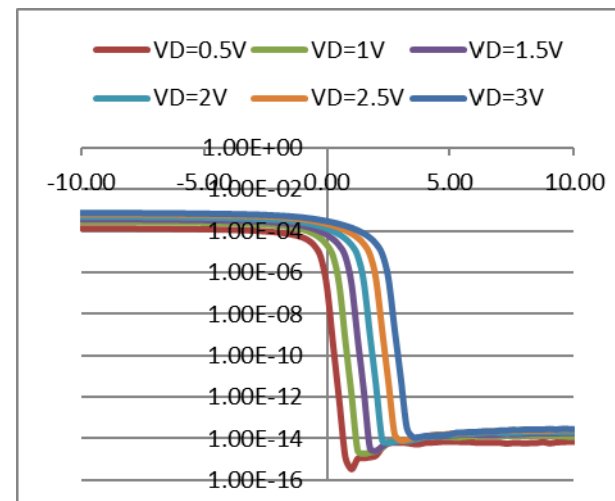


Fig.16: Ids vs Vgs curves

NW thickness 75nm:

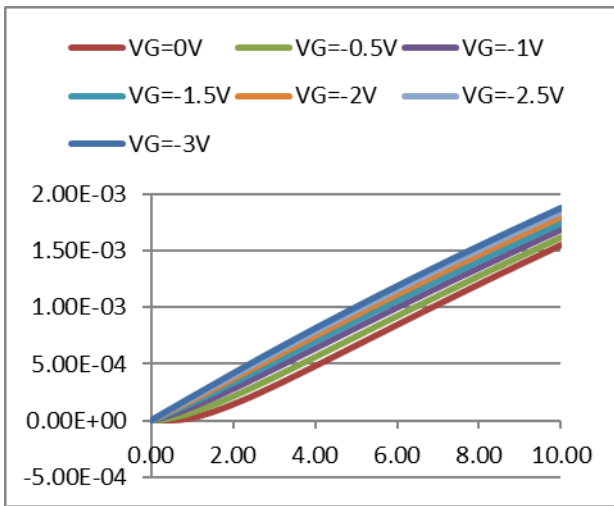


Fig.17: Ids vs Vds curves

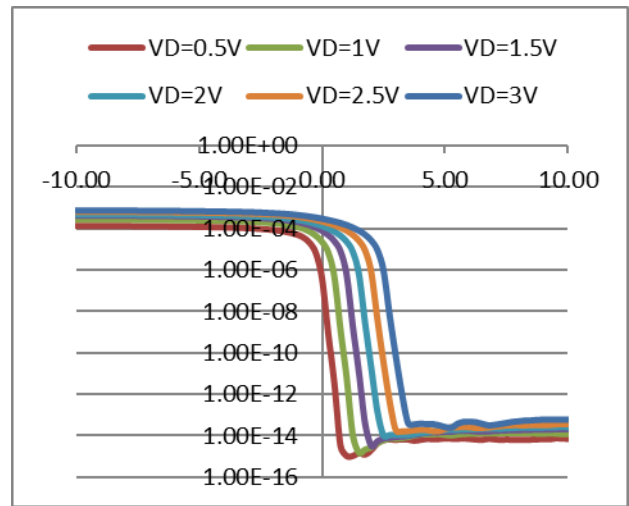


Fig.18: Ids vs Vgs curves

NW thickness 100nm:

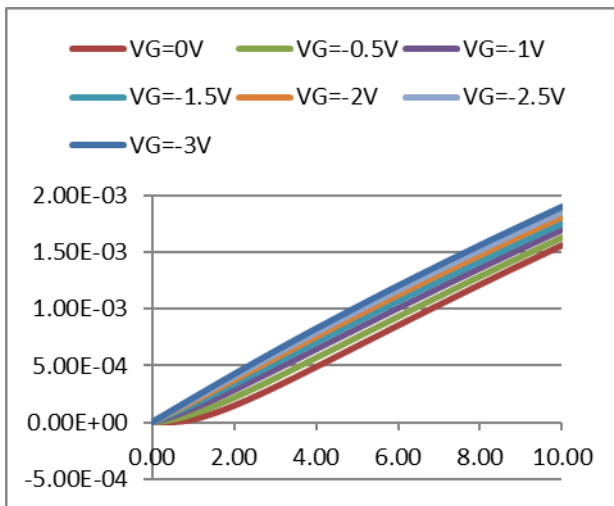


Fig.19: Ids vs Vds curves

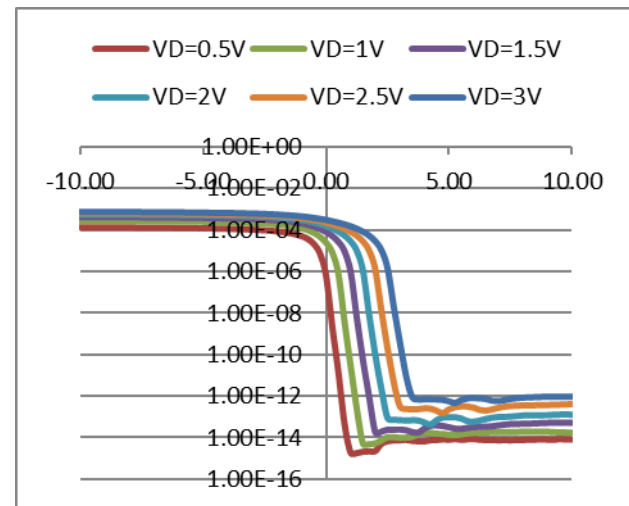


Fig.20: Ids vs Vgs curves

3. $4e16/cm^3$

NW thickness 10nm:

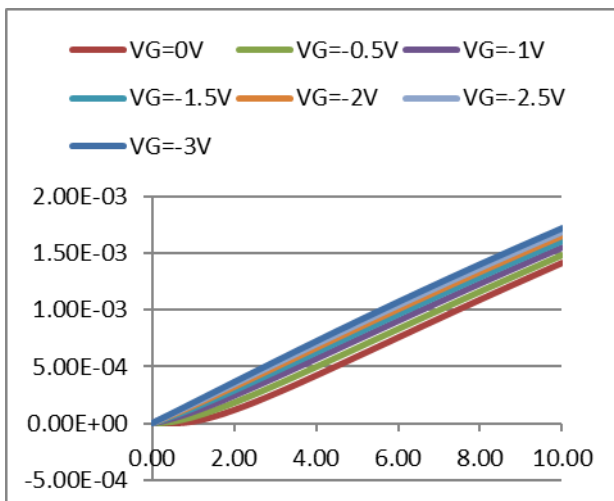


Fig.21: Ids vs Vds curves

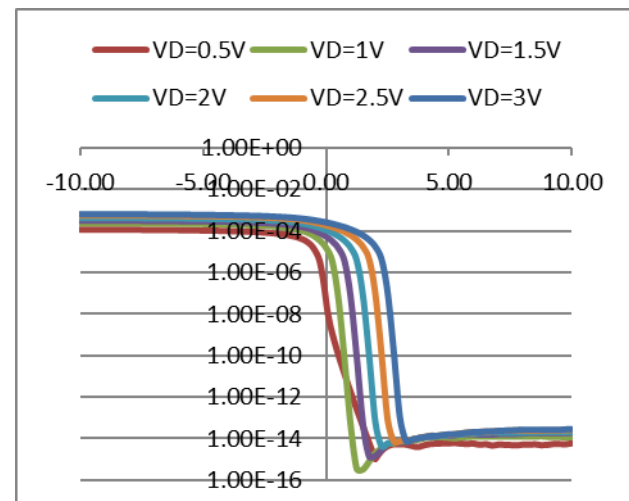


Fig.22: Ids vs Vgs curves

NW thickness 25nm:

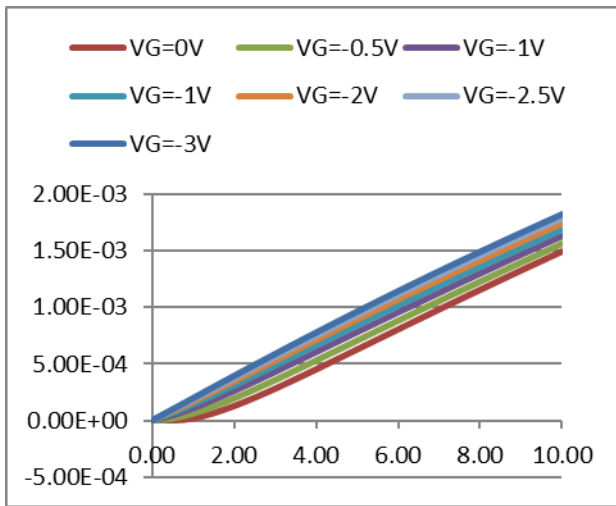


Fig.23: Ids vs Vds curves

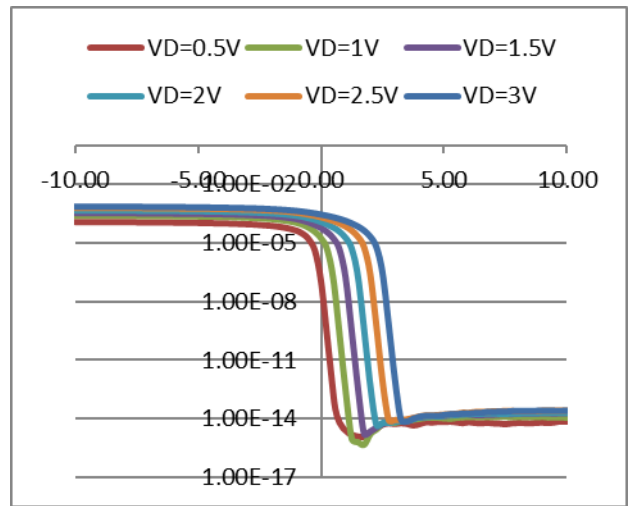


Fig.24: Ids vs Vgs curves

NW thickness 50nm:

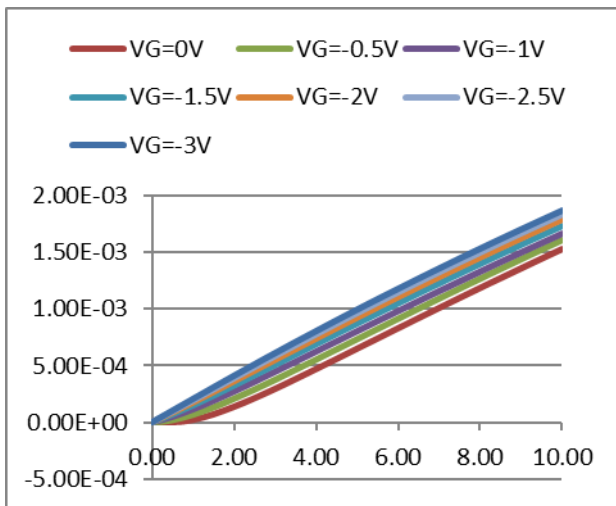


Fig.25: Ids vs Vds curves

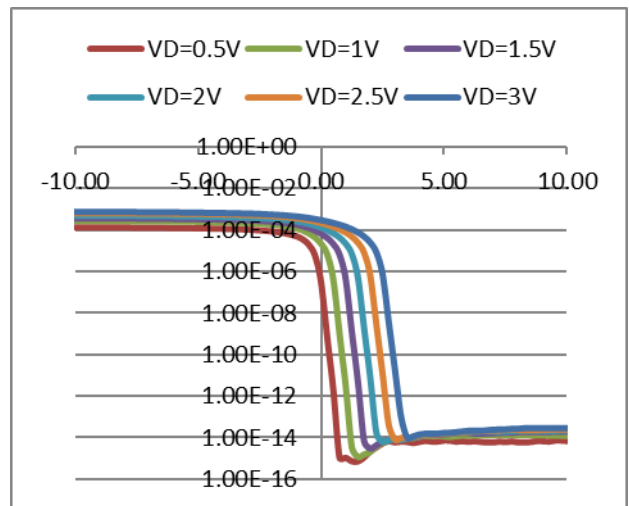


Fig.26: Ids vs Vgs curves

NW thickness 75nm:

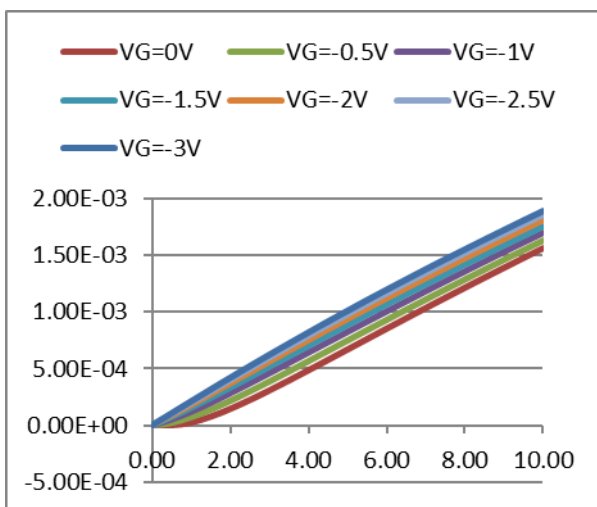


Fig.27: Ids vs Vds curves

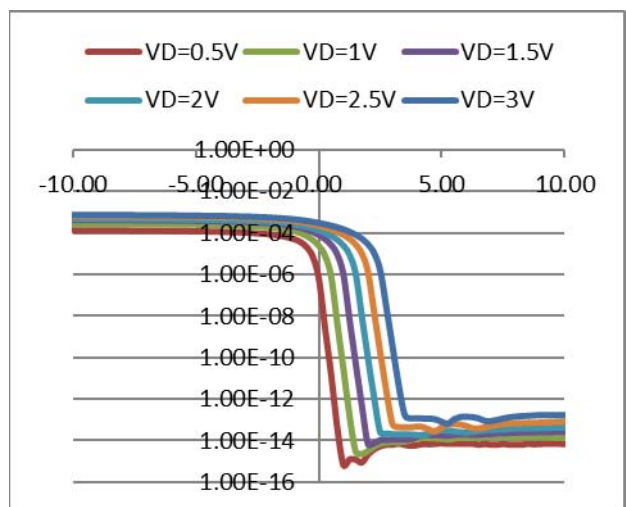


Fig.28: Ids vs Vgs curves

NW thickness 100nm:

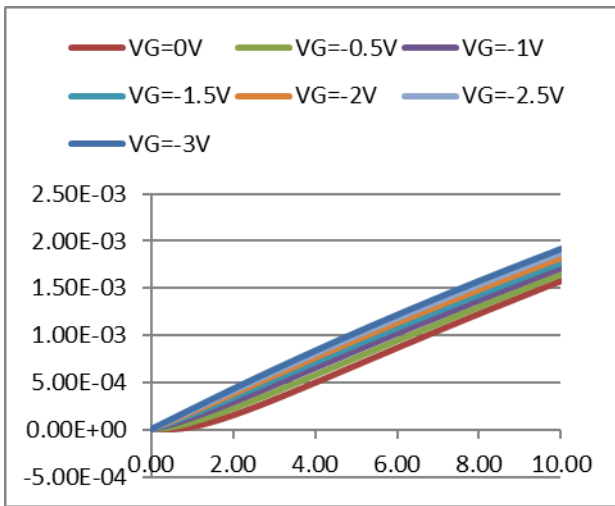


Fig.29: Ids vs Vds curves

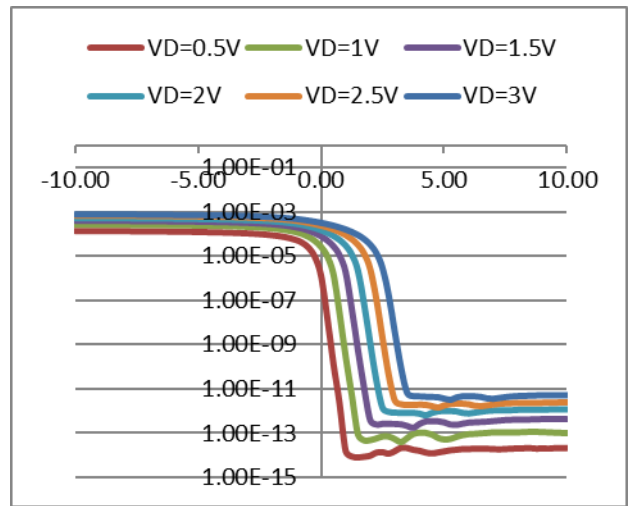


Fig.30: Ids vs Vgs curves

4. $6e16/cm^3$

NW thickness 10nm:

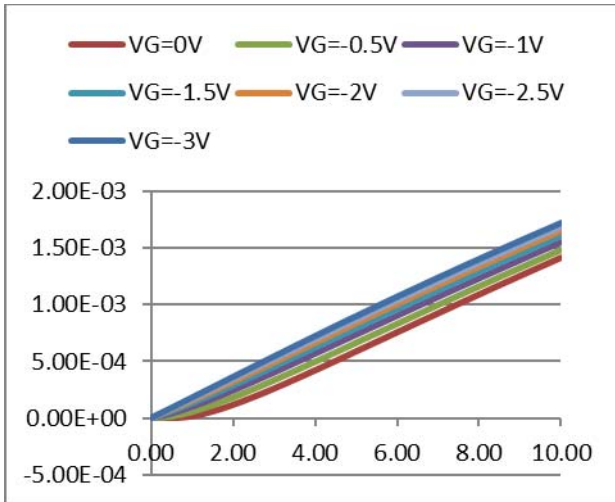


Fig.31: Ids vs Vds curves

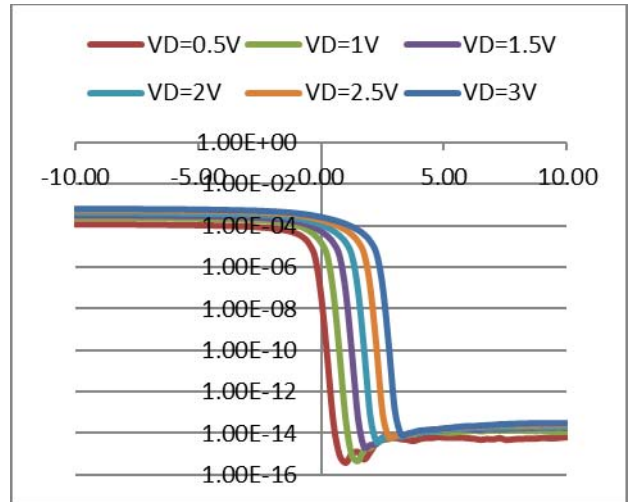


Fig.32: Ids vs Vgs curves

NW thickness 25nm:

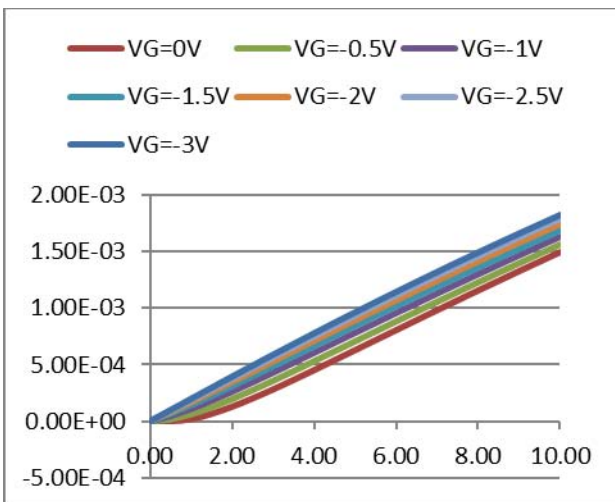


Fig.33: Ids vs Vds curves

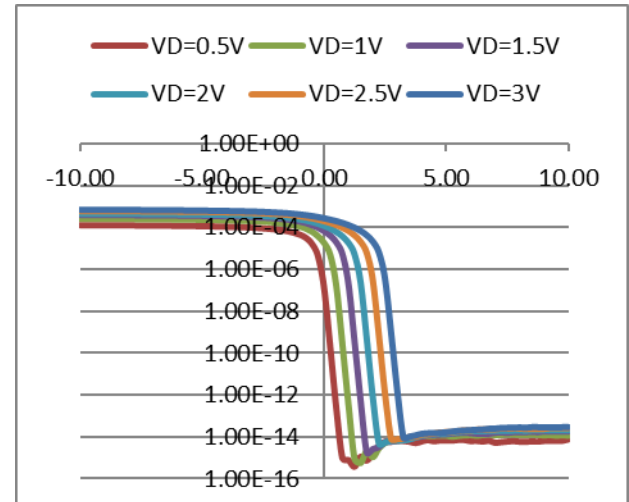


Fig.34: Ids vs Vgs curves

NW thickness 50nm:

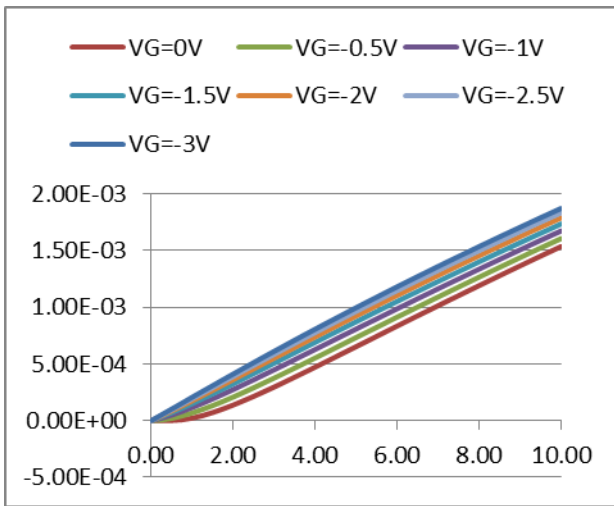


Fig.35: Ids vs Vds curves

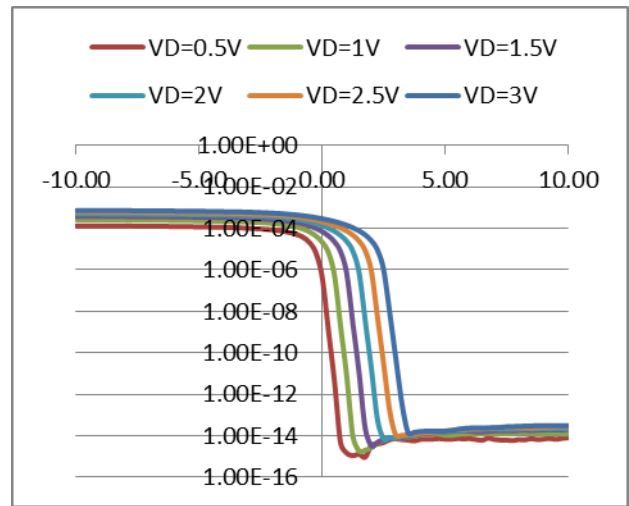


Fig.36: Ids vs Vgs curves

NW thickness 75nm:

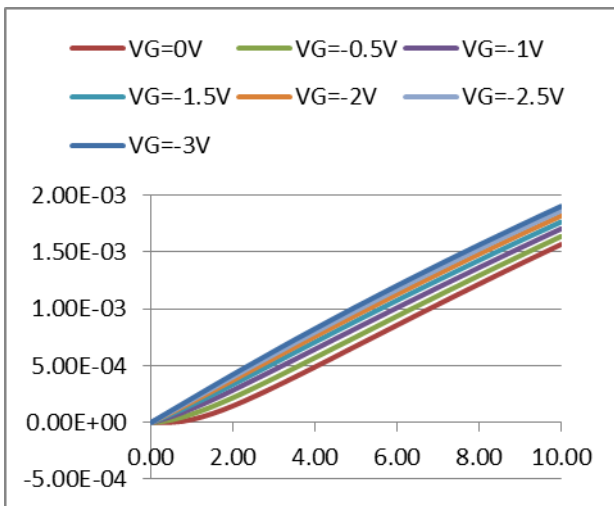


Fig.37: Ids vs Vds curves

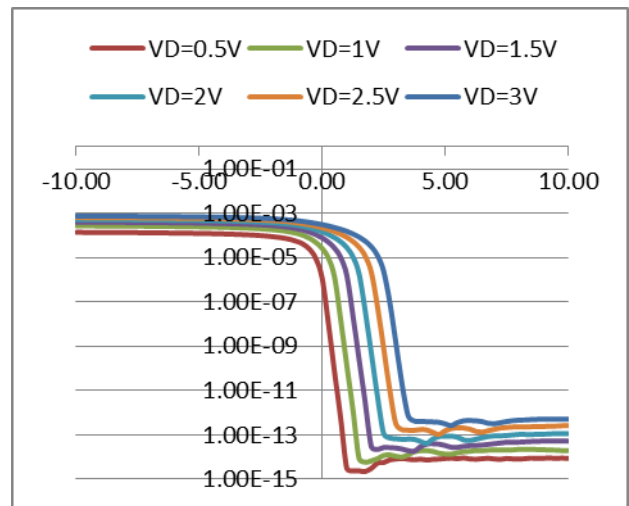


Fig.38: Ids vs Vgs curves

NW thickness 100nm:

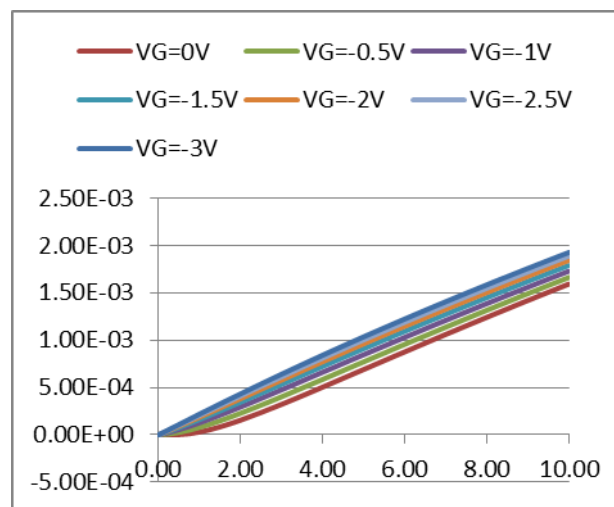


Fig.39: Ids vs Vds curves

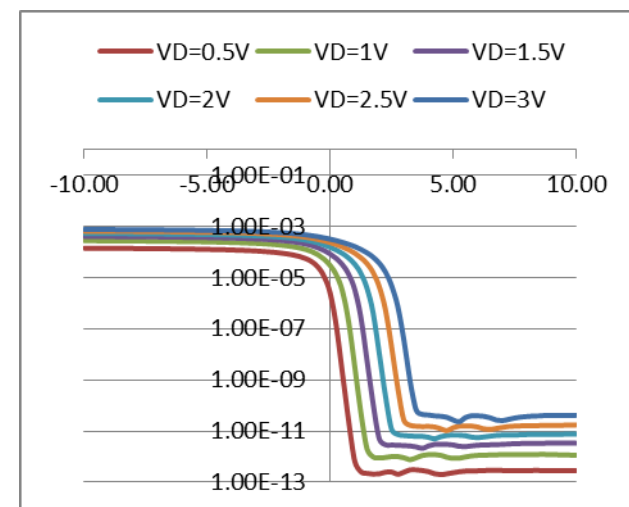


Fig.40: Ids vs Vgs curves

5. $8e16/cm^3$

NW thickness 10nm:

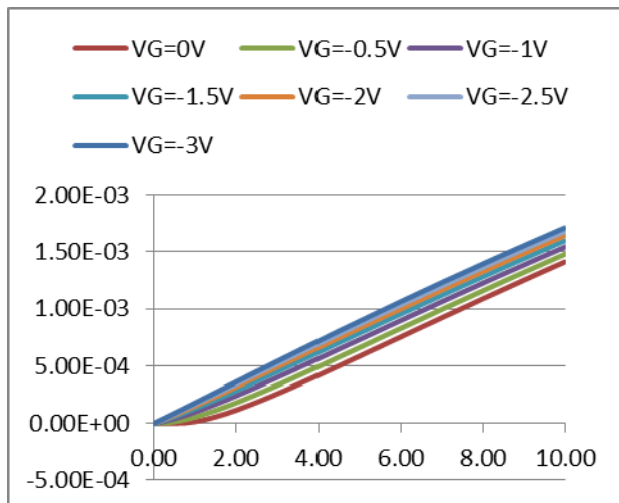


Fig.41: Ids vs Vds curves

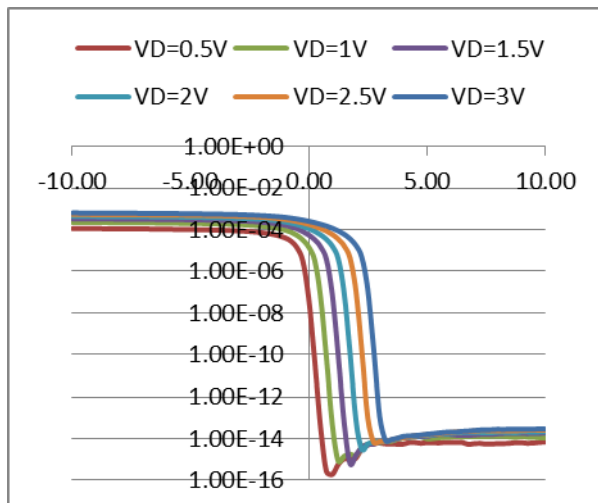


Fig.42: Ids vs Vgs curves

NW thickness 25nm:

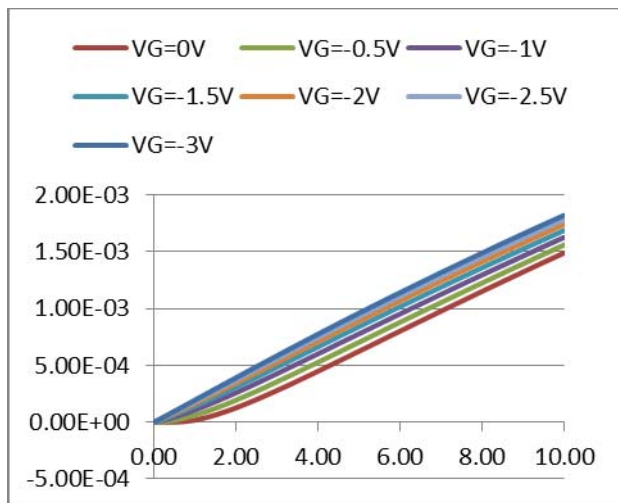


Fig.43: Ids vs Vds curves

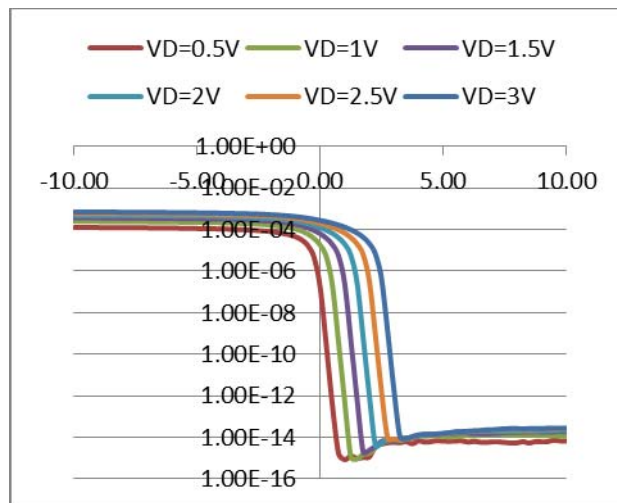


Fig.44: Ids vs Vgs curves

NW thickness 50nm:

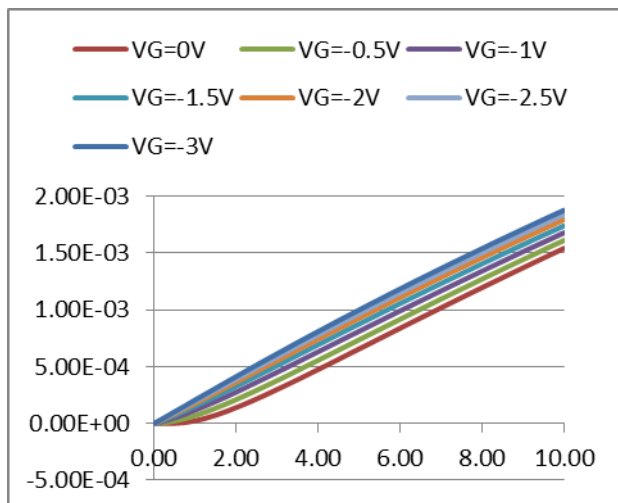


Fig.45: Ids vs Vds curves

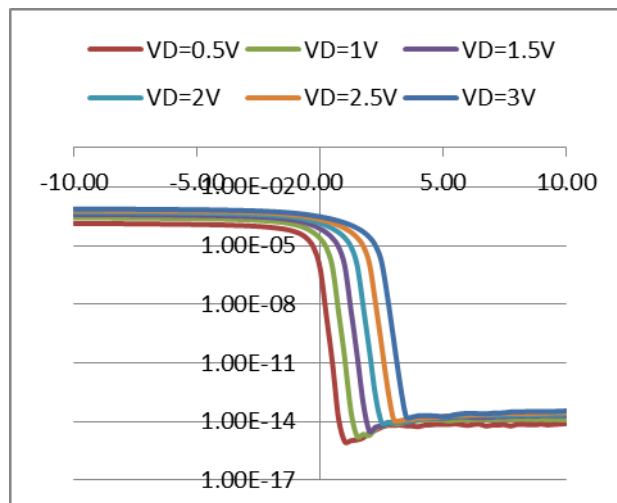


Fig.46: Ids vs Vgs curves

NW thickness 75nm:

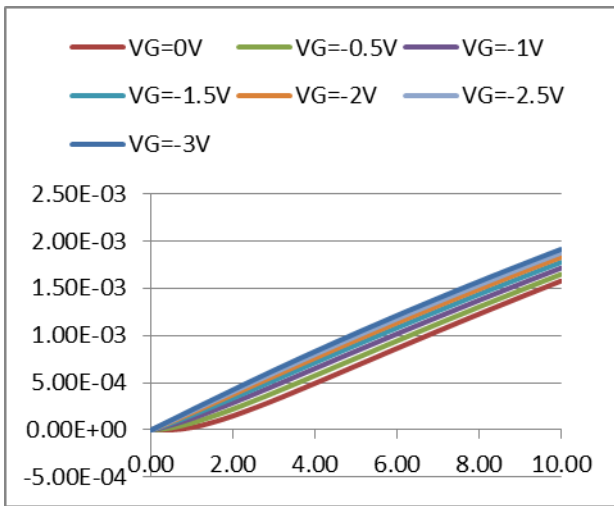


Fig.47: Ids vs Vds curves

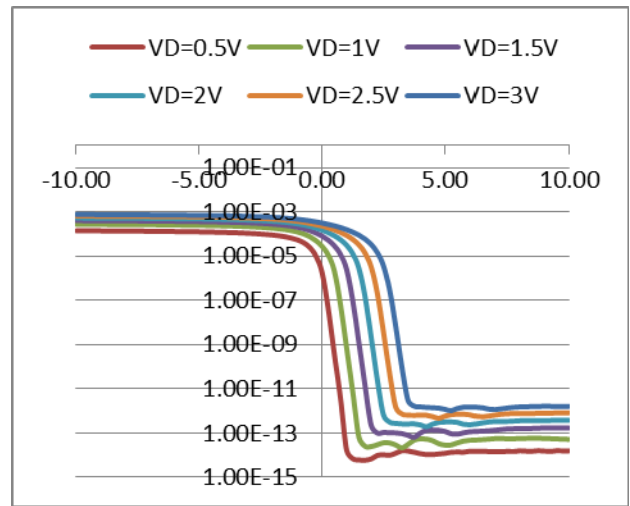


Fig.48: Ids vs Vgs curves

NW thickness 100nm:

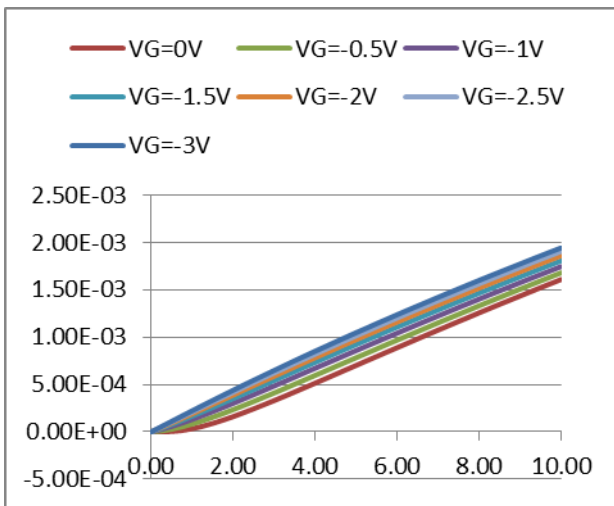


Fig.49: Ids vs Vds curves

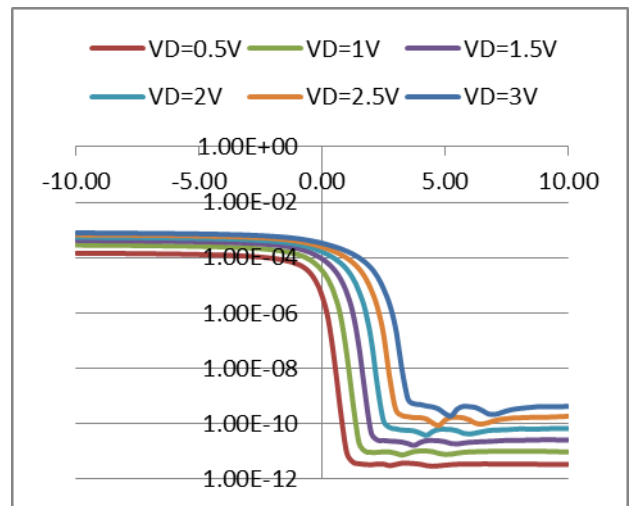


Fig.50: Ids vs Vgs curves

6. $1e17/cm^3$

NW thickness 10nm:

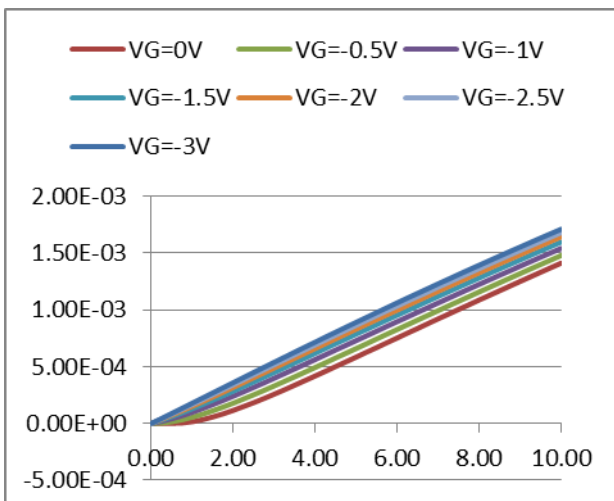


Fig.51: Ids vs Vds curves

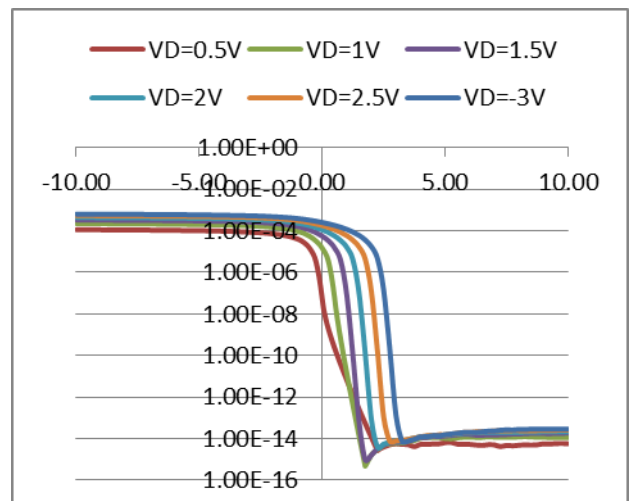


Fig.52: Ids vs Vgs curves

NW thickness 25nm:

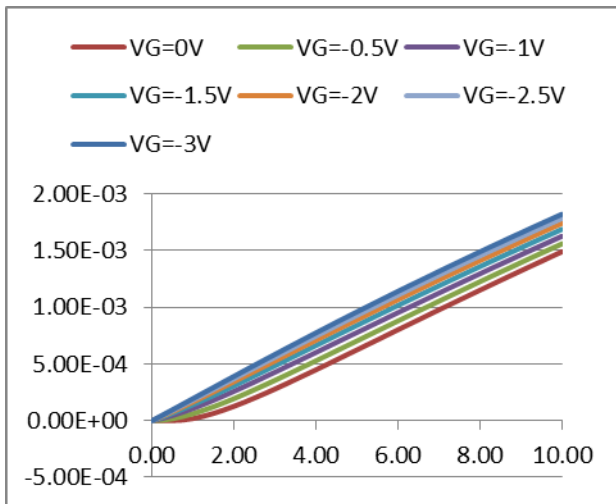


Fig.53: I_{ds} vs V_{ds} curves

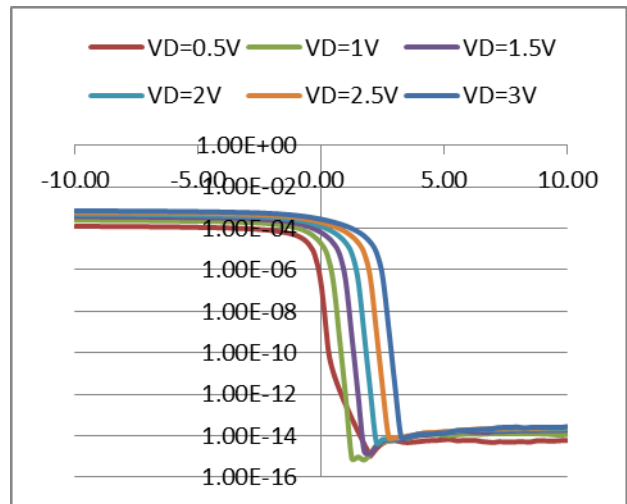


Fig.54: I_{ds} vs V_{gs} curves

NW thickness 50nm:

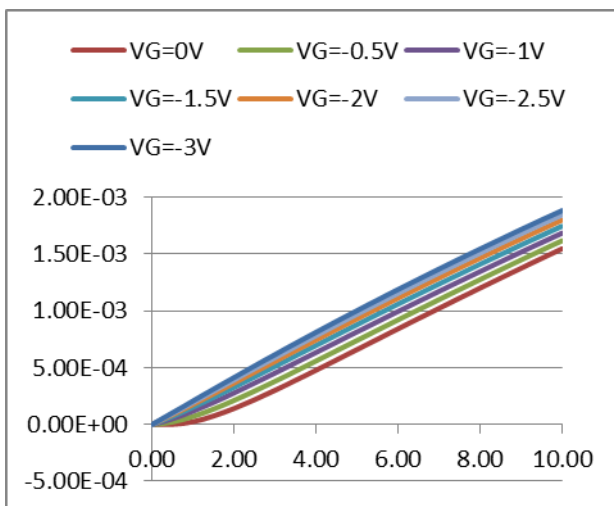


Fig.55: I_{ds} vs V_{ds} curves

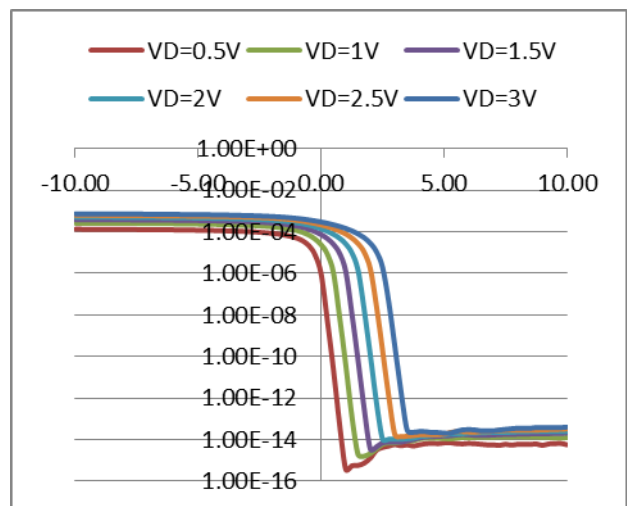


Fig.56: I_{ds} vs V_{gs} curves

NW thickness 75nm:

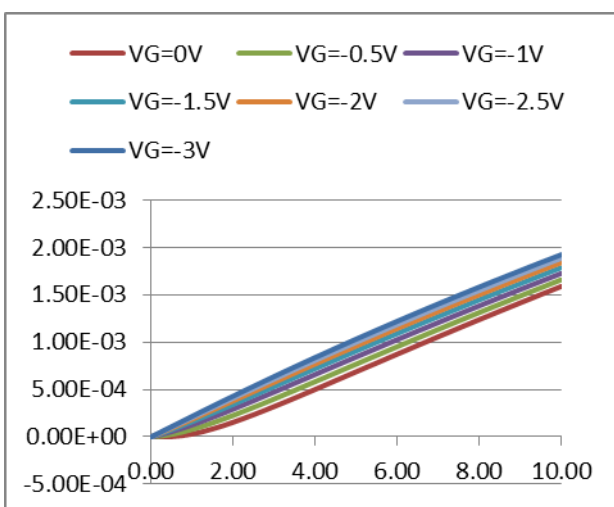


Fig.57: I_{ds} vs V_{ds} curves

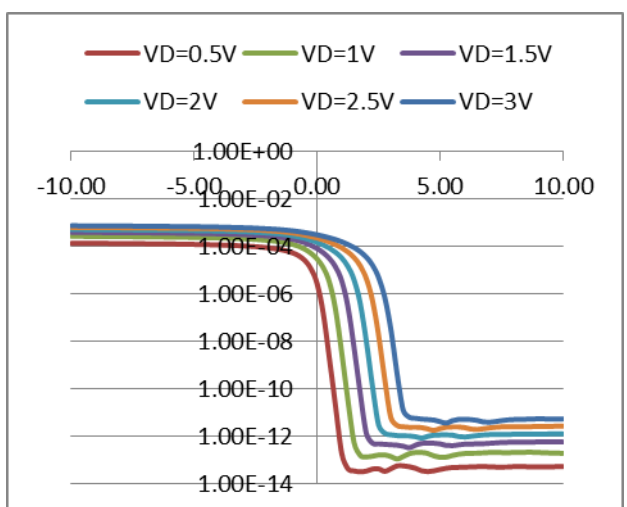


Fig.58: I_{ds} vs V_{gs} curves

NW thickness 100nm:

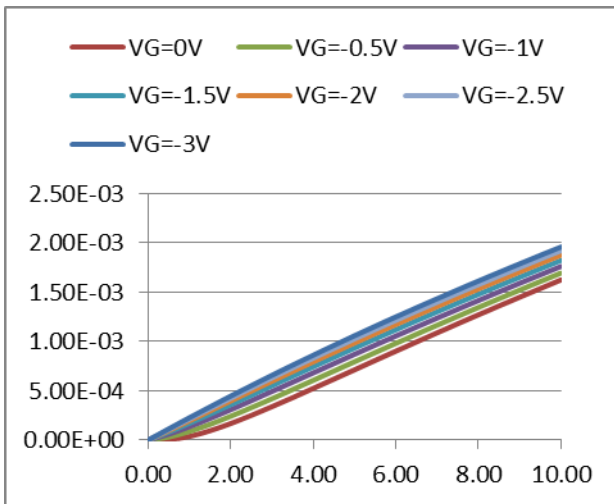


Fig.59: Ids vs Vds curves

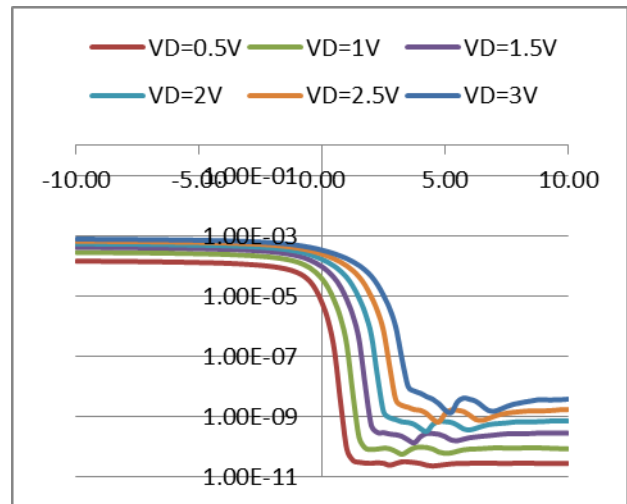


Fig.60: Ids vs Vgs curves

7. $2e17/cm^3$

NW thickness 10nm:

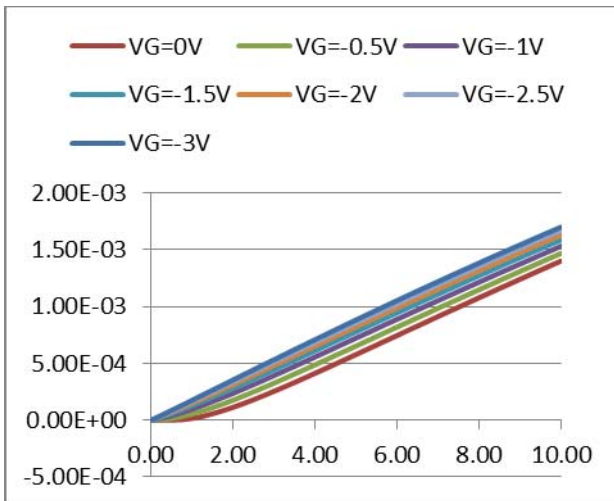


Fig.61: Ids vs Vds curves

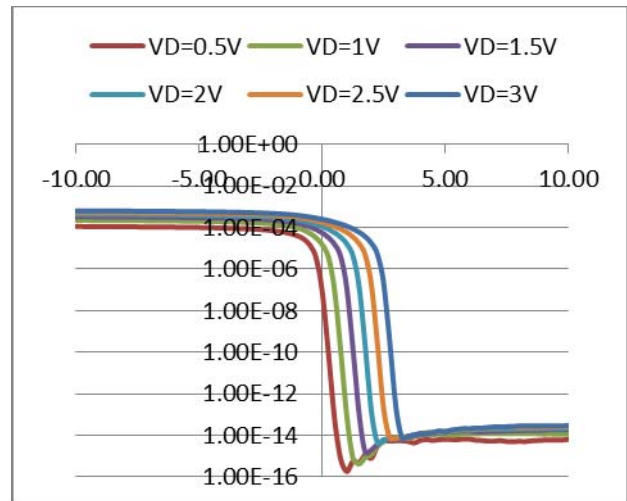


Fig.62: Ids vs Vgs curves

NW thickness 25nm:

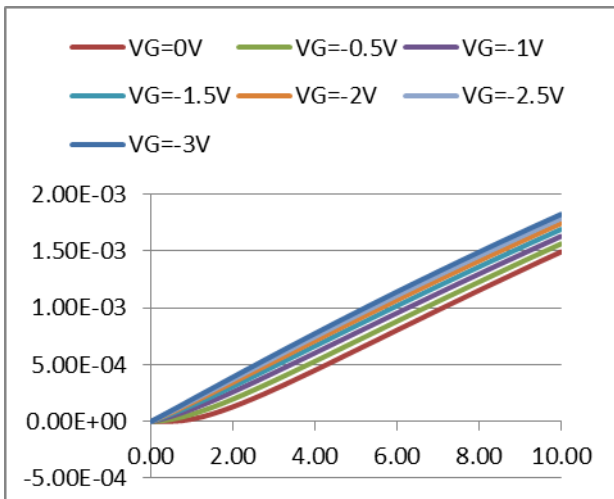


Fig.63: Ids vs Vds curves

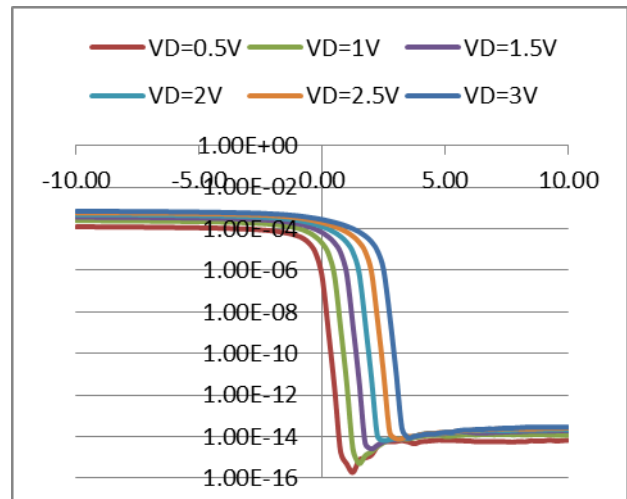


Fig.64: Ids vs Vgs curves

NW thickness 50nm:

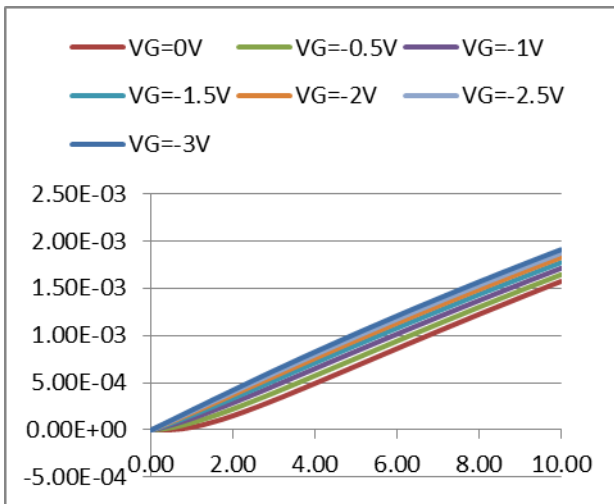


Fig.65: Ids vs Vds curves

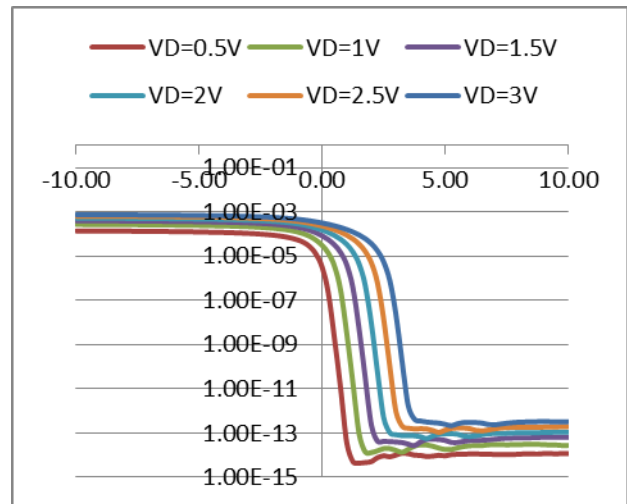


Fig.66: Ids vs Vgs curves

NW thickness 75nm:

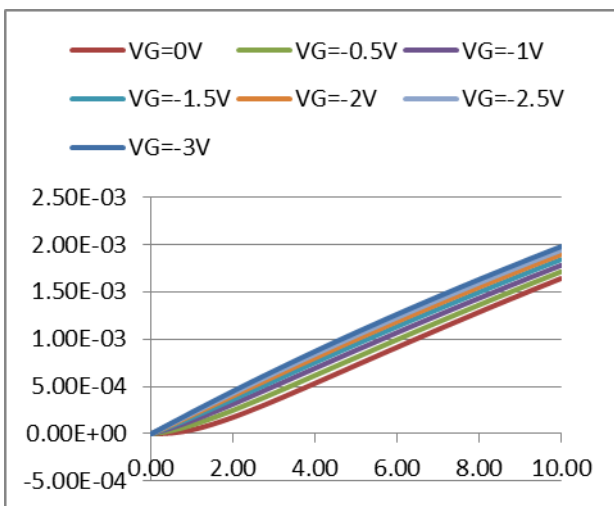


Fig.67: Ids vs Vds curves

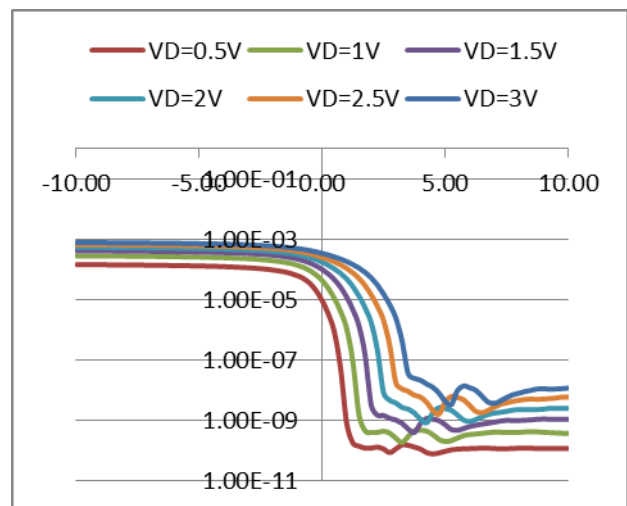


Fig.68: Ids vs Vgs curves

NW thickness 100nm:

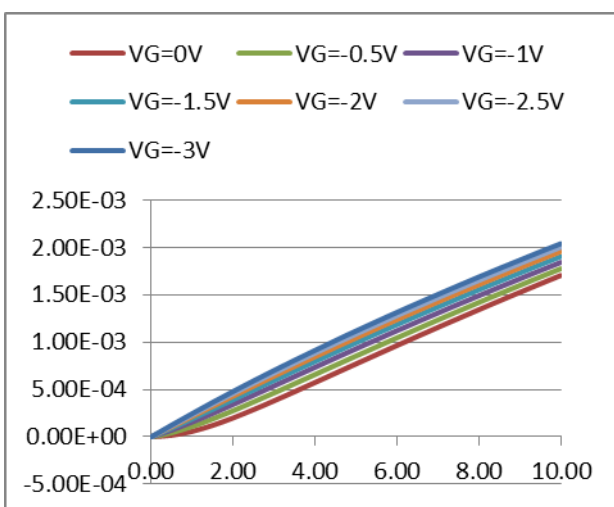


Fig.69: Ids vs Vds curves

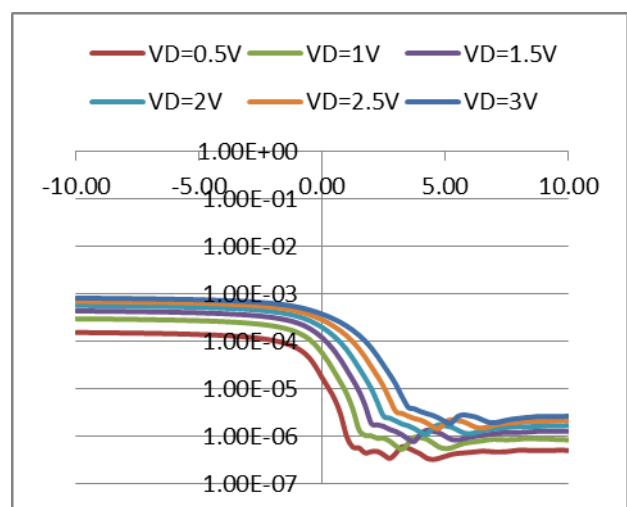


Fig.70: Ids vs Vgs curves

8. $4e17/cm^3$

NW thickness 10nm:

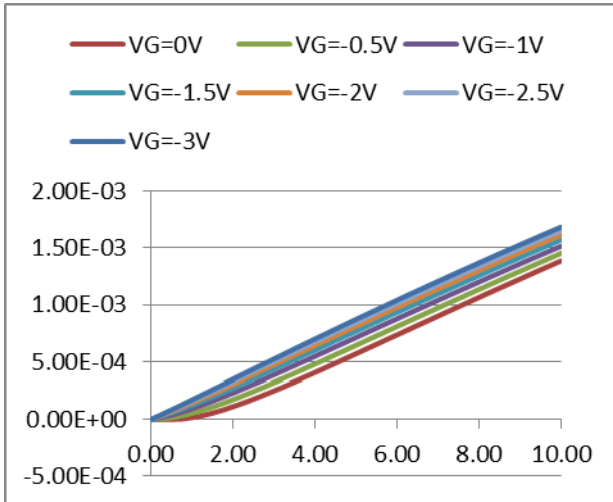


Fig.71: I_{ds} vs V_{ds} curves

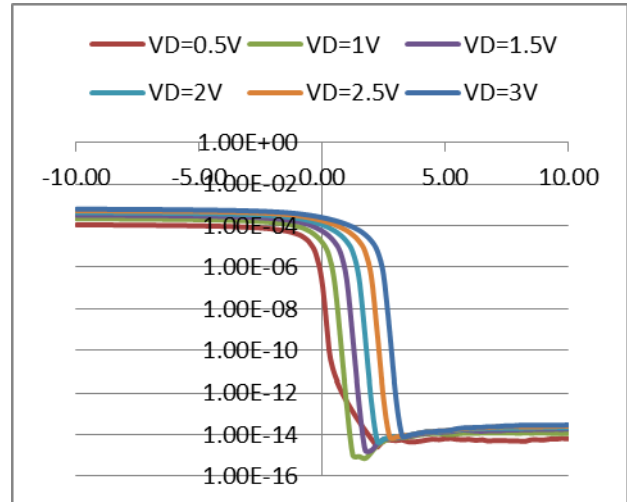


Fig.72: I_{ds} vs V_{gs} curves

NW thickness 25nm:

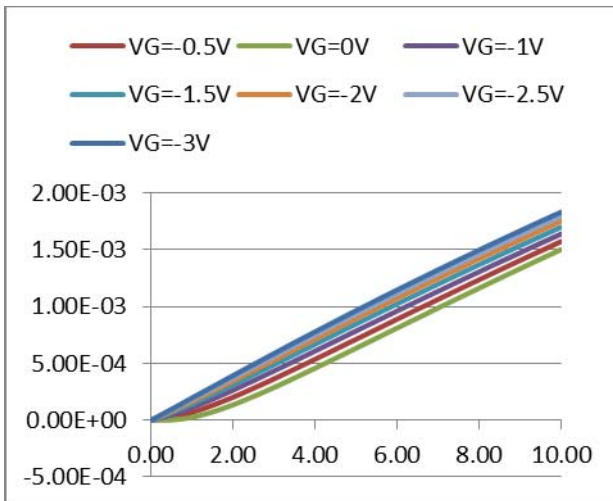


Fig.73: I_{ds} vs V_{ds} curves

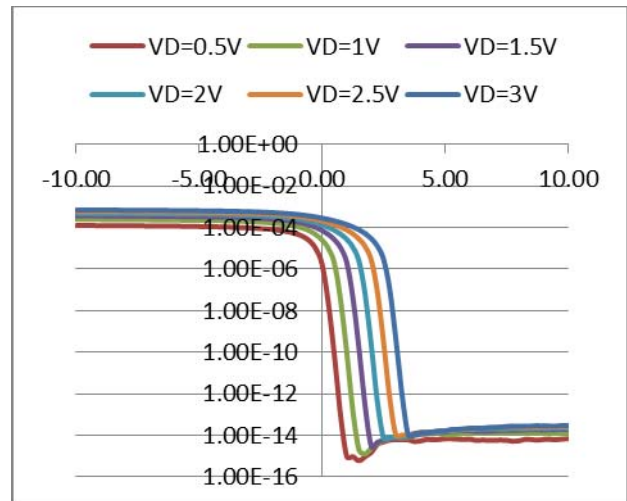


Fig.74: I_{ds} vs V_{gs} curves

NW thickness 50nm:

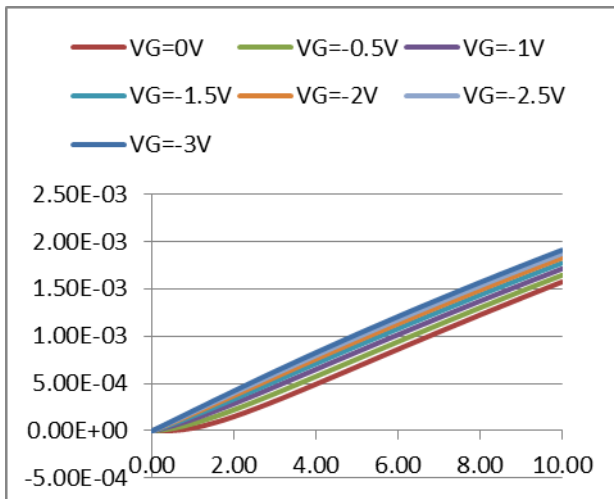


Fig.75: I_{ds} vs V_{ds} curves

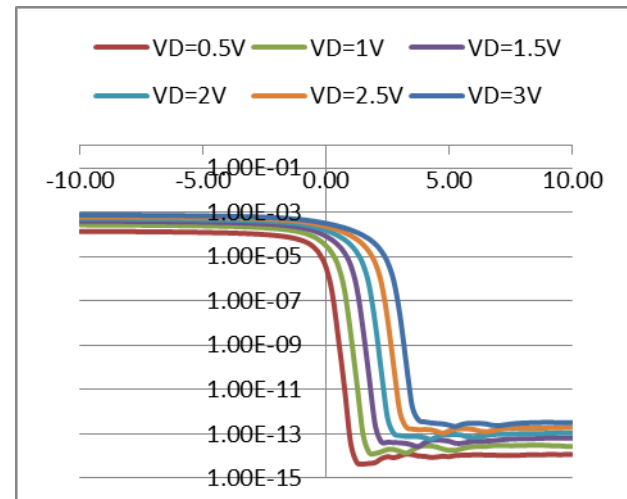


Fig.76: I_{ds} vs V_{gs} curves

NW thickness 50nm:

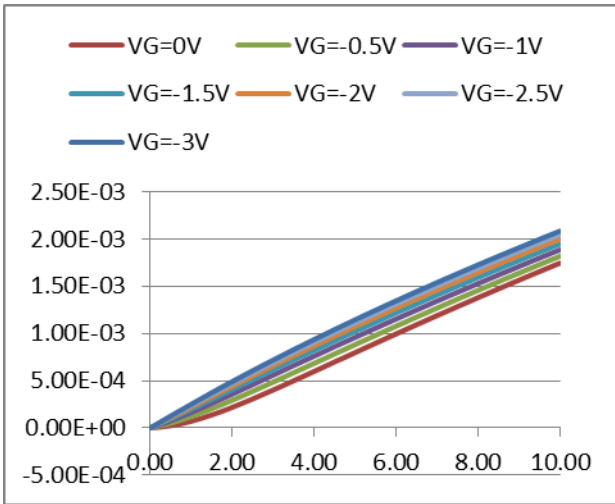


Fig.77: Ids vs Vds curves

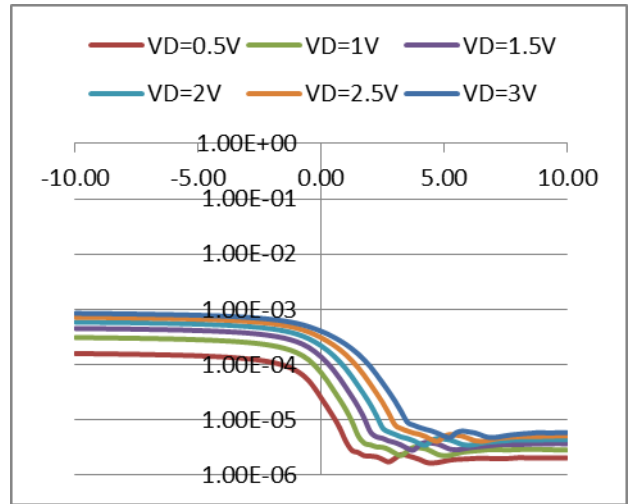


Fig.78: Ids vs Vgs curves

NW thickness 100nm

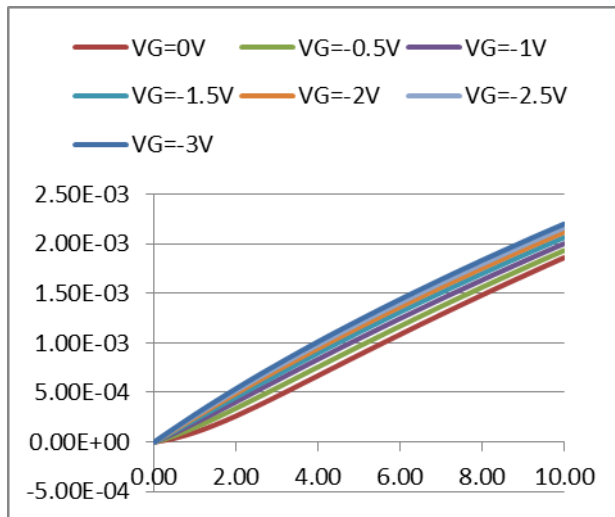


Fig.79: Ids vs Vds curves

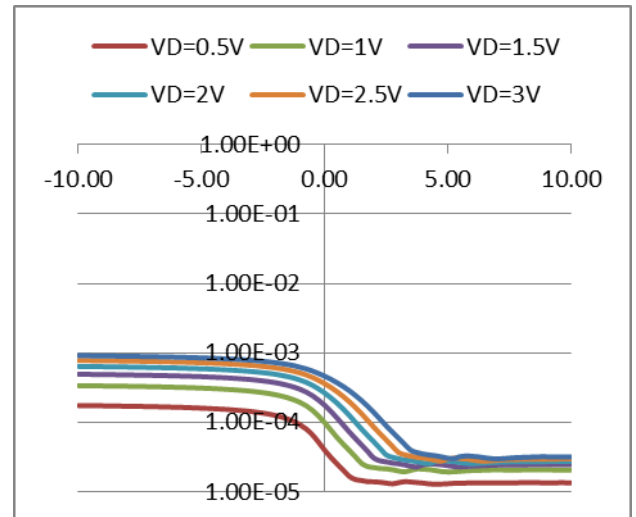


Fig.80: Ids vs Vgs curves

9. $6e17/cm^3$

NW thickness 10nm:

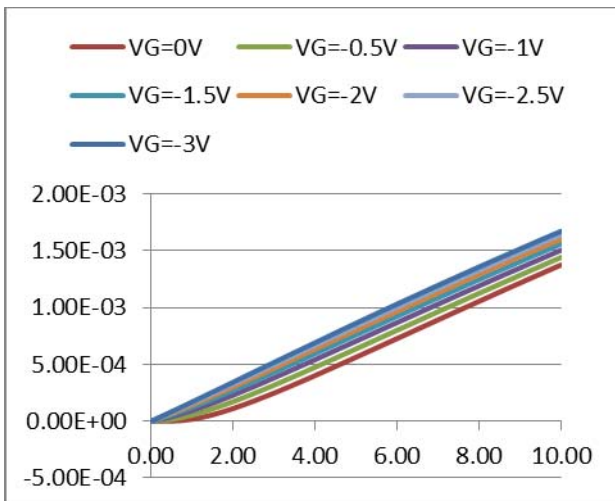


Fig.81: Ids vs Vds curves

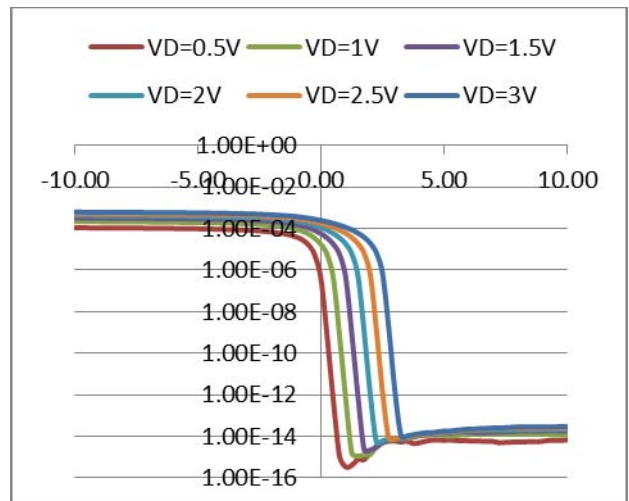


Fig.82: Ids vs Vgs curves

NW thickness 25nm:

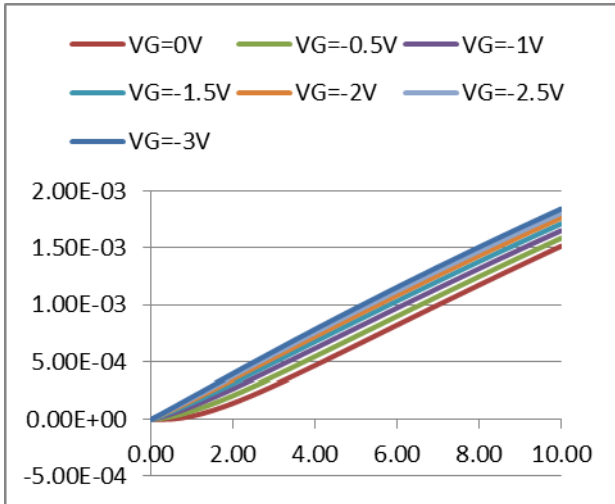


Fig.83: Ids vs Vds curves

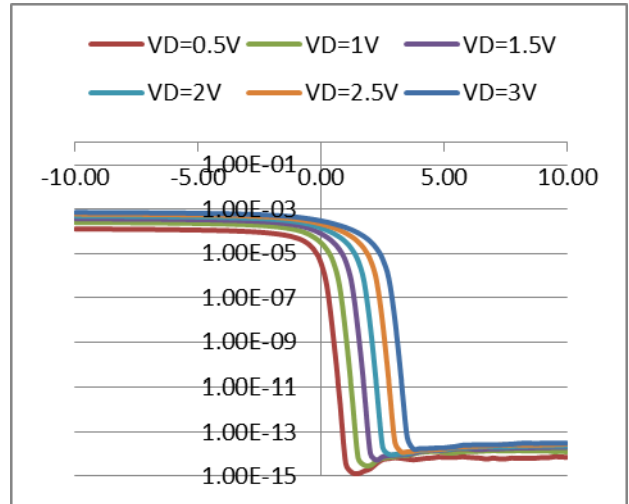


Fig.84: Ids vs Vgs curves

NW thickness 50nm:

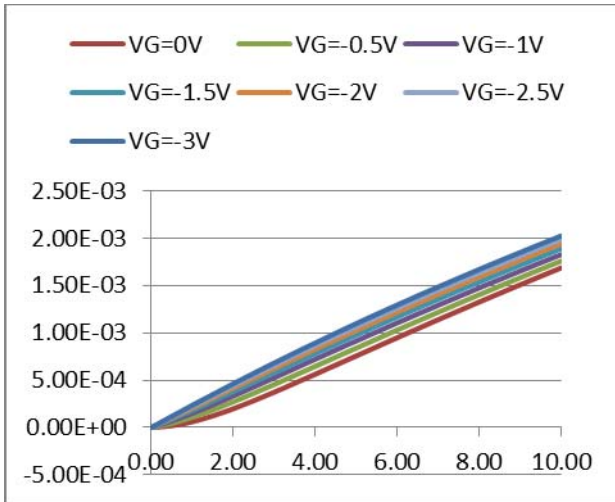


Fig.85: Ids vs Vds curves

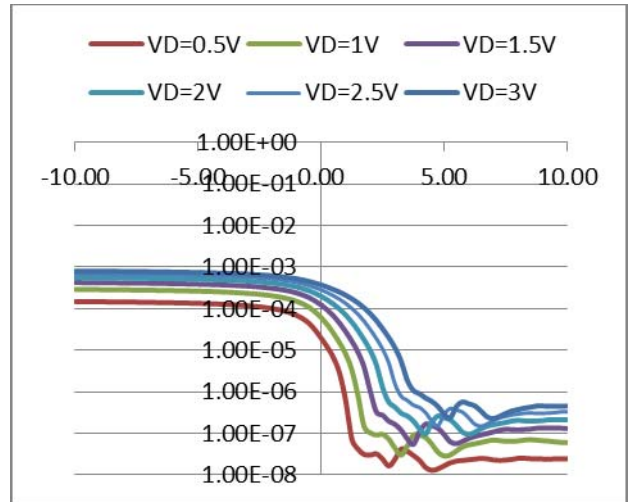


Fig.86: Ids vs Vgs curves

NW thickness 75nm:

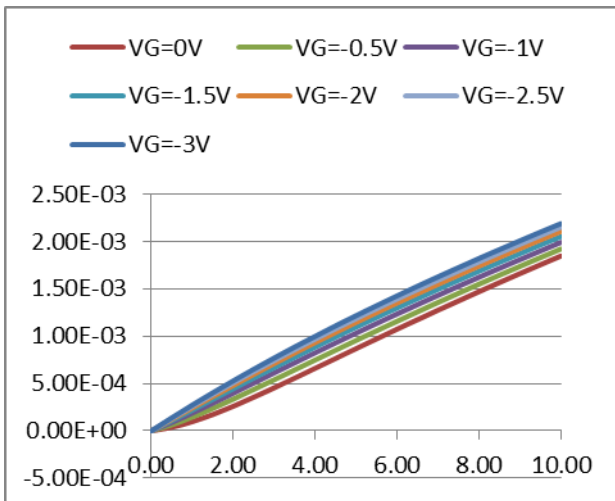


Fig.87: Ids vs Vds curves

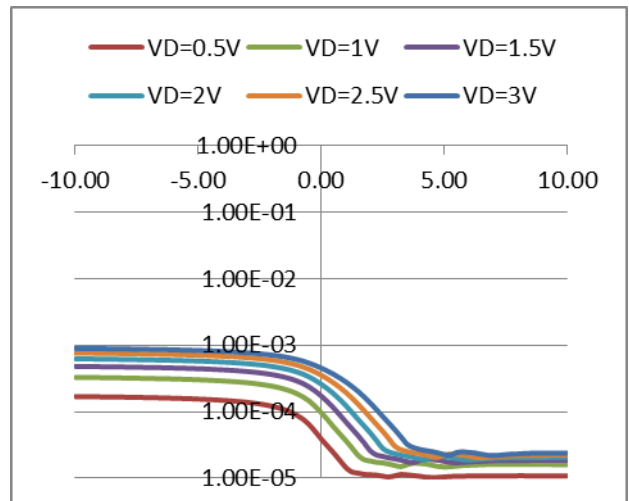


Fig.88: Ids vs Vgs curves

NW thickness 100nm:

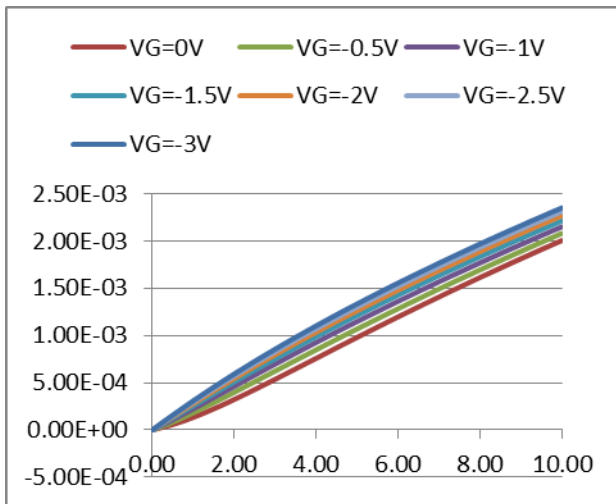


Fig.89: Ids vs Vds curves

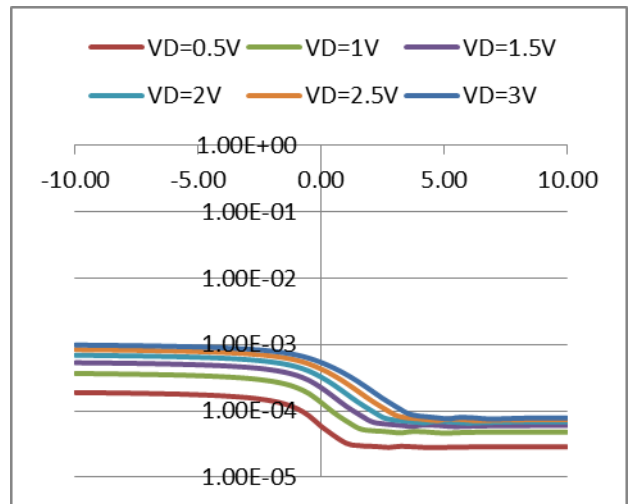


Fig.90: Ids vs Vgs curves

10. $8e17/cm^3$

NW thickness 10nm:

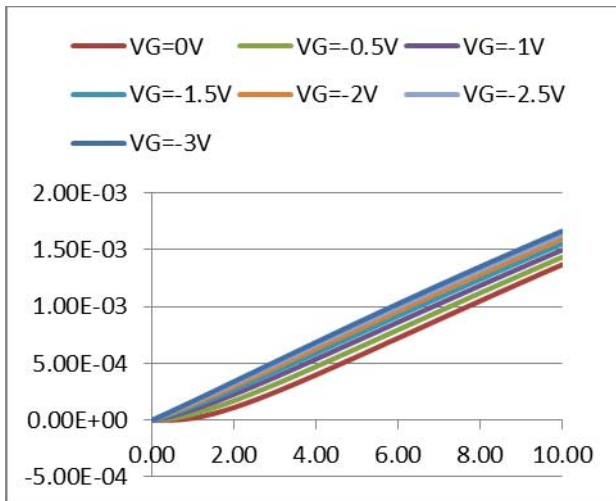


Fig.91: Ids vs Vds curves

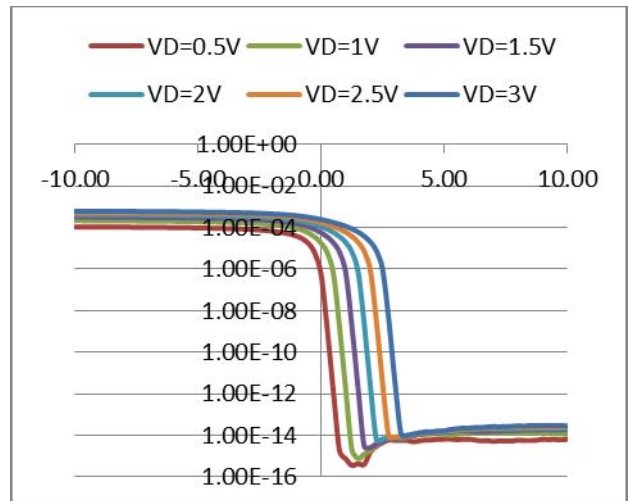


Fig.92: Ids vs Vgs curves

NW thickness 25nm:

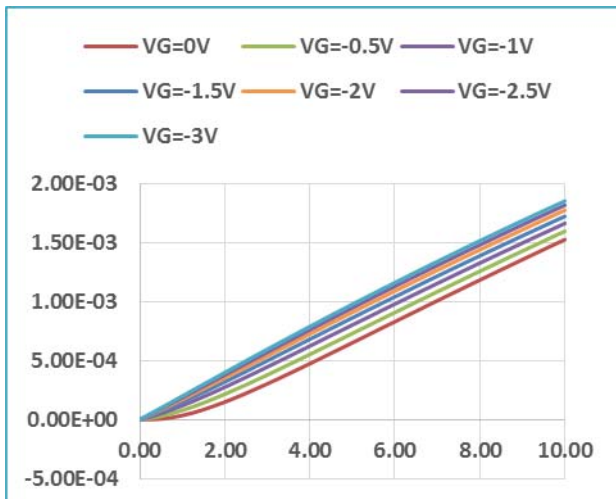


Fig.93: Ids vs Vds curves

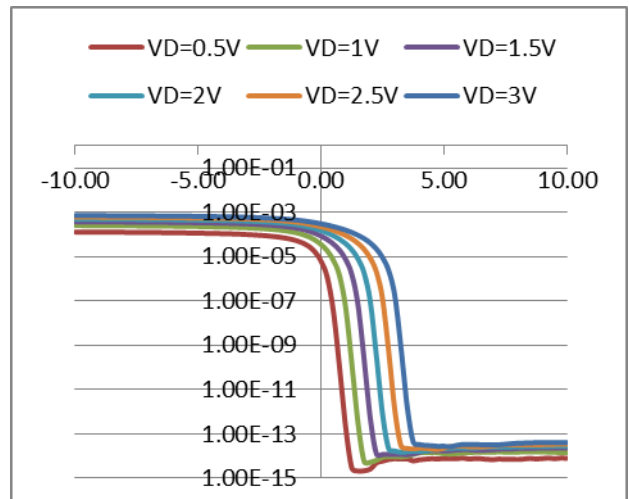


Fig.94: Ids vs Vgs curves

NW thickness 50nm:

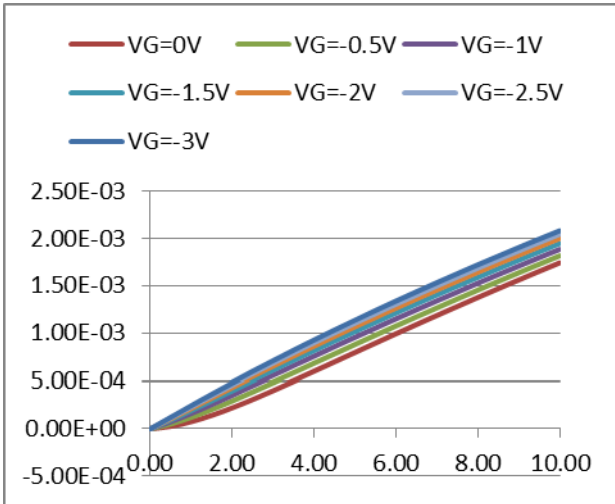


Fig.95: Ids vs Vds curves

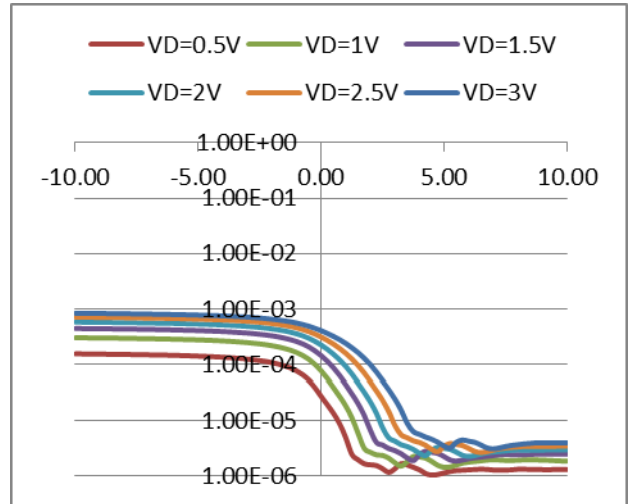


Fig.96: Ids vs Vgs curves

NW thickness 75nm:

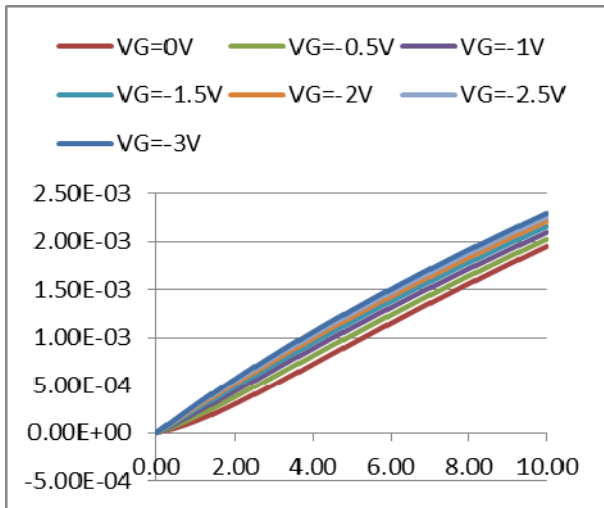


Fig.97: Ids vs Vds curves

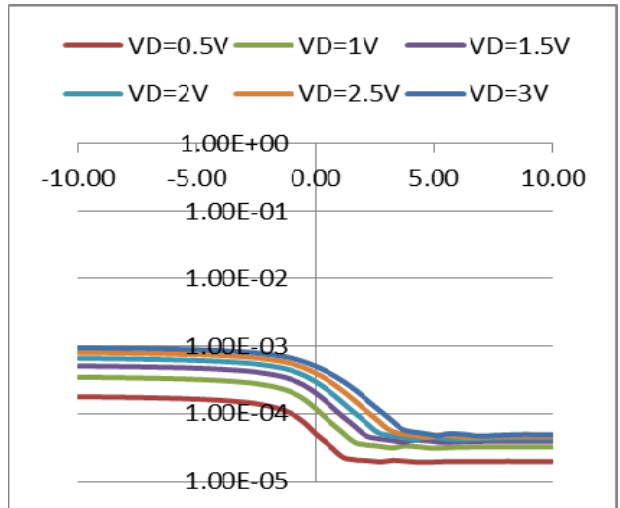


Fig.98: Ids vs Vgs curves

NW thickness 100nm:

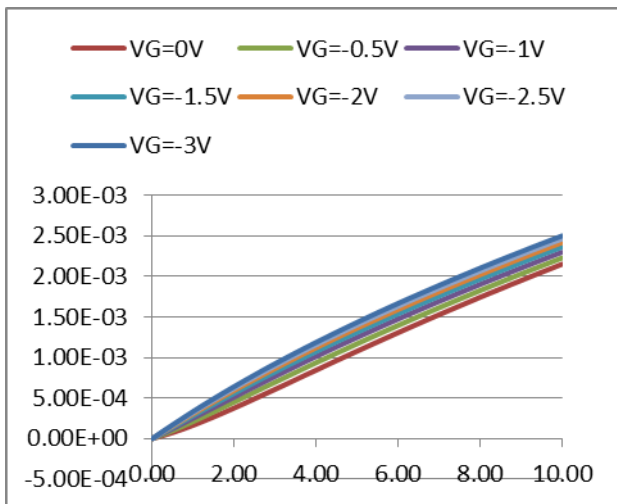


Fig.99: Ids vs Vds curves

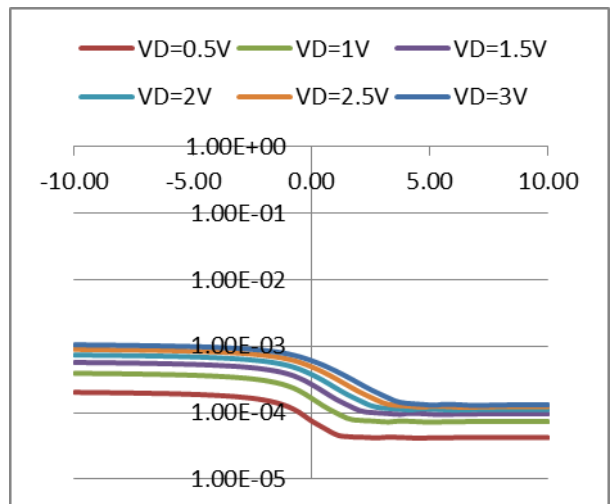


Fig.100: Ids vs Vgs curves

11. $1e18/cm^3$

NW thickness 10nm:

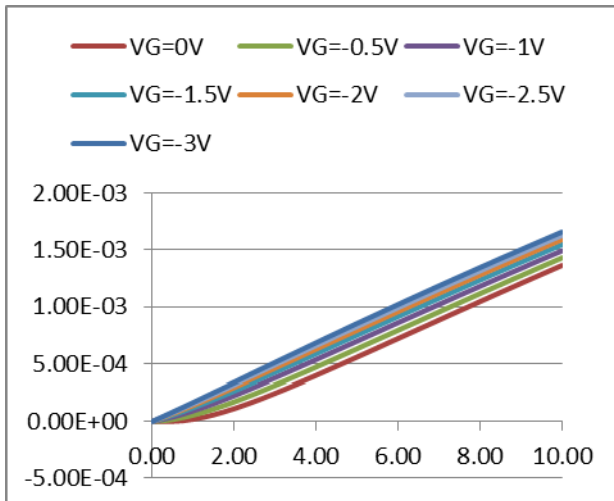


Fig.101: Ids vs Vds curves

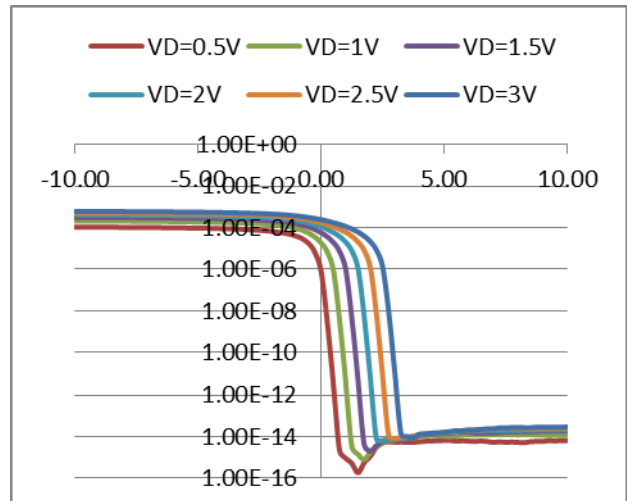


Fig.102: Ids vs Vgs curves

NW thickness 25nm:

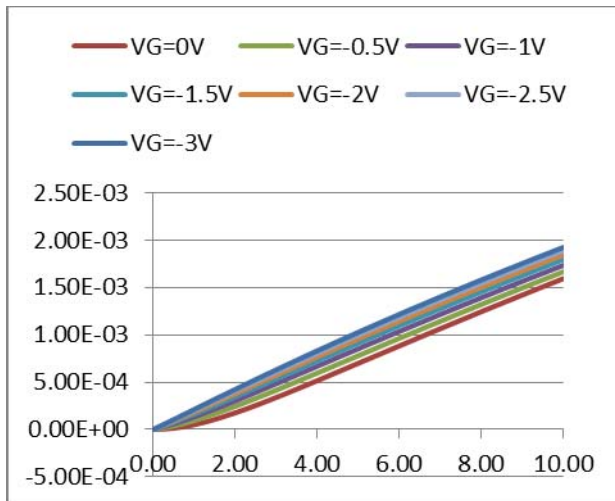


Fig.103: Ids vs Vds curves

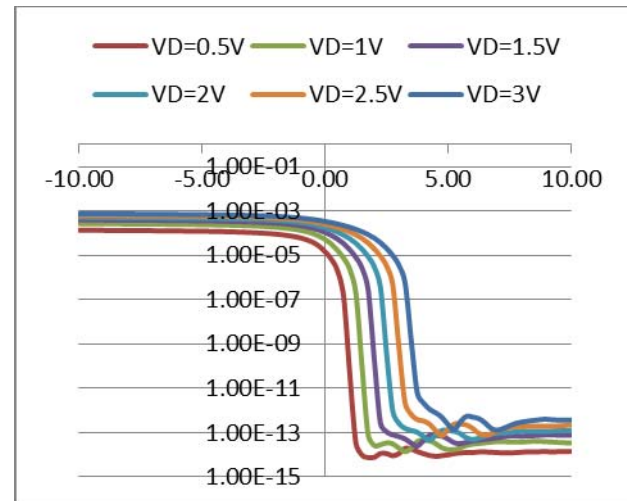


Fig.104: Ids vs Vgs curves

NW thickness 50nm:

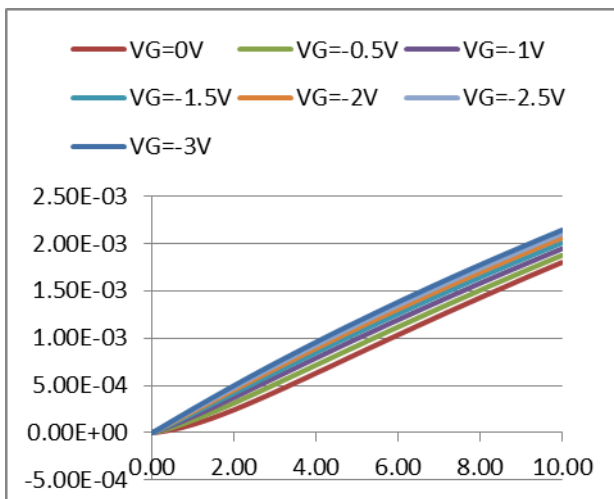


Fig.105: Ids vs Vds curves

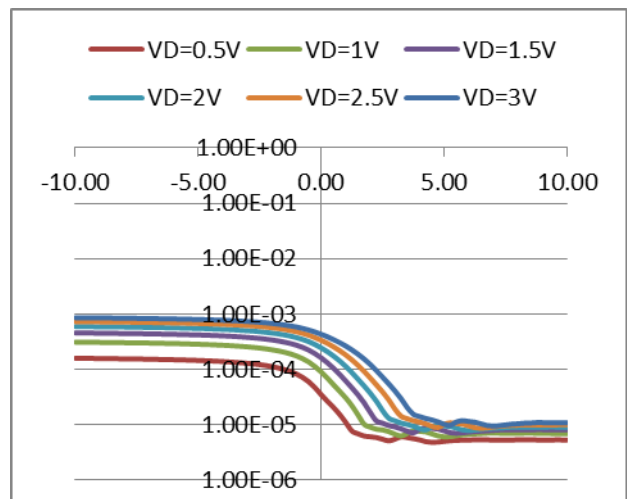


Fig.106: Ids vs Vgs curves

NW thickness 75nm:

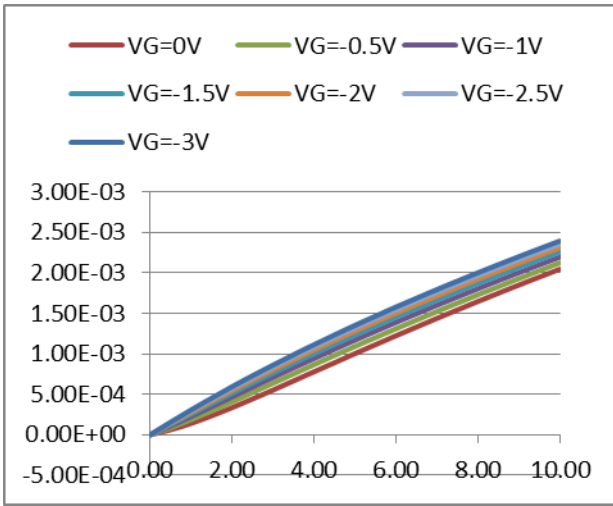


Fig.107: Ids vs Vds curves

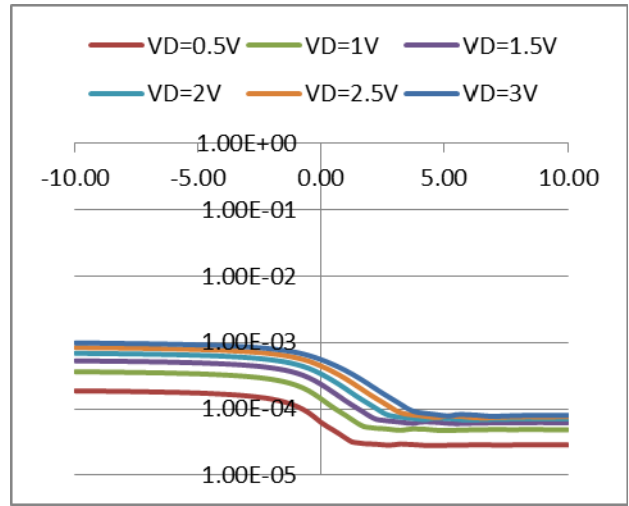


Fig.108: Ids vs Vgs curves

NW thickness 75nm:

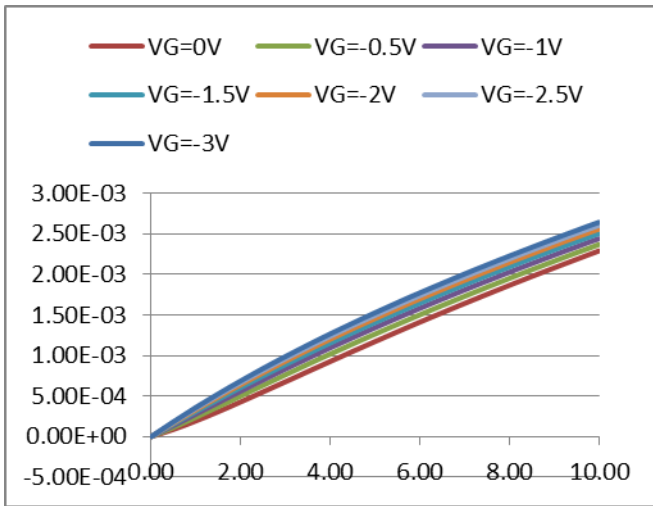


Fig.109: Ids vs Vds curves

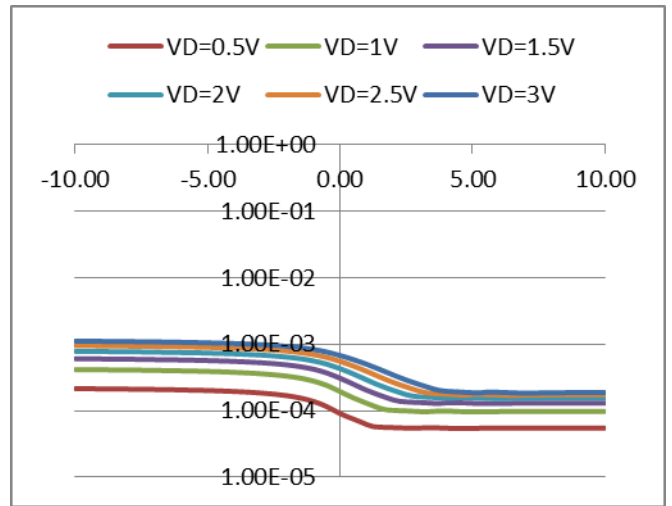


Fig.110: Ids vs Vgs curves

Appendix B

Poly Silicon Nanowire

1. $1e16/cm^3$

NW thickness 10nm:

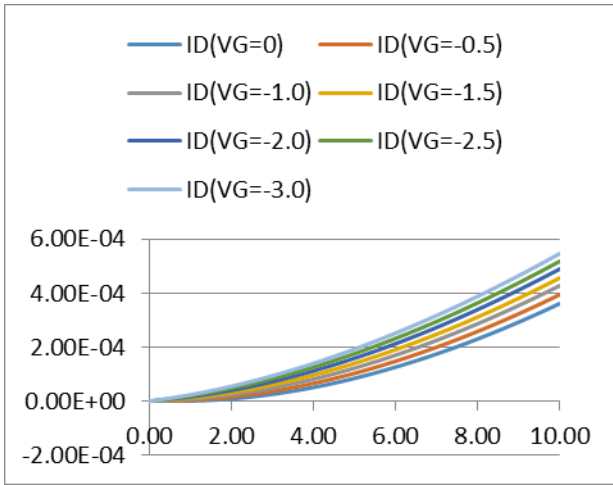


Fig.01: I_{ds} vs V_{ds} curves

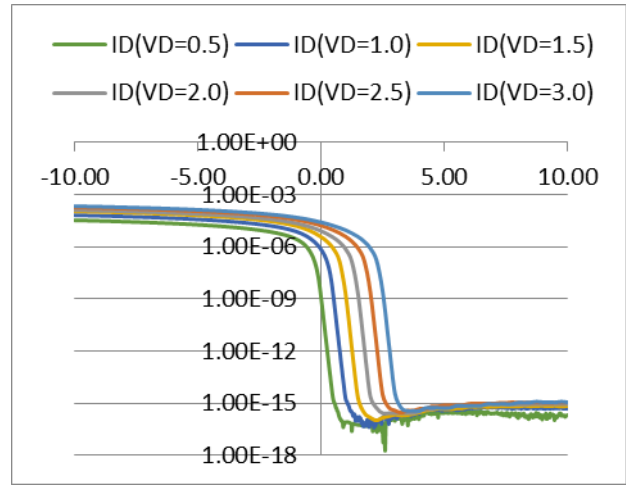


Fig.02: I_{ds} vs V_{gs} curves

NW thickness 25nm:

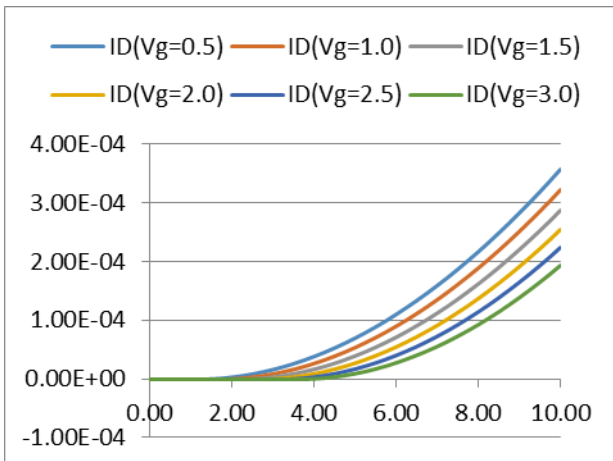


Fig.03: I_{ds} vs V_{ds} curves

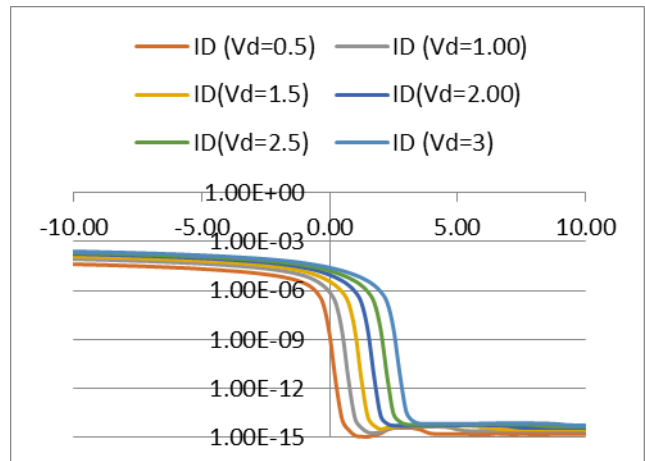


Fig.04: I_{ds} vs V_{gs} curves

NW thickness 50nm:

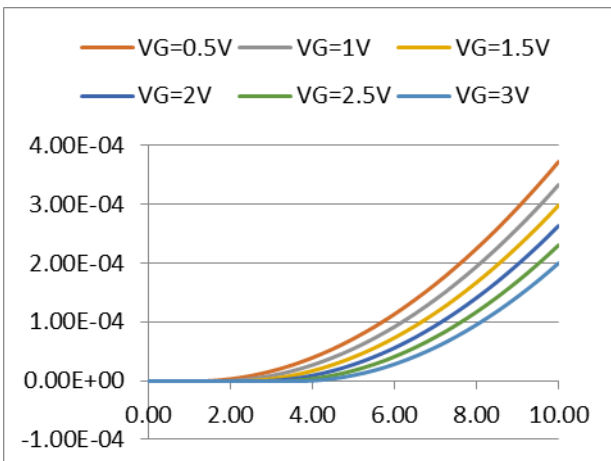


Fig.05: I_{ds} vs V_{ds} curves

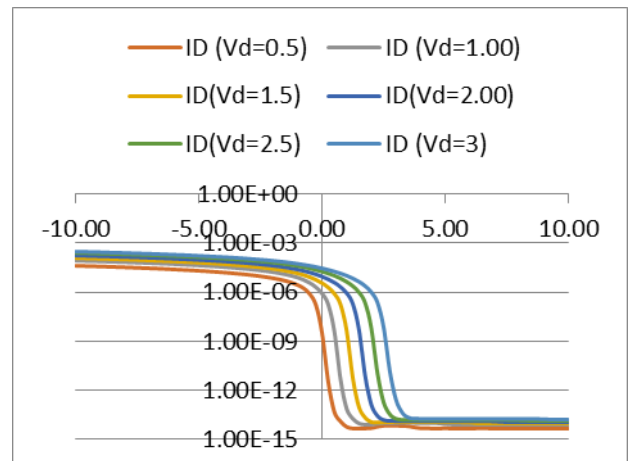


Fig.06: I_{ds} vs V_{gs} curves

NW thickness 75nm:

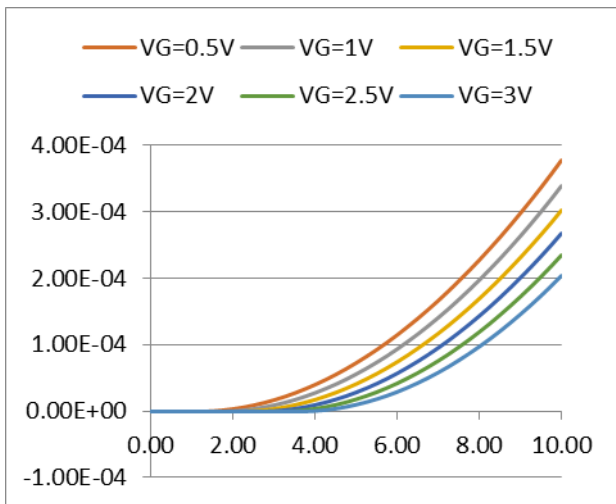


Fig.07: Ids vs Vds curves

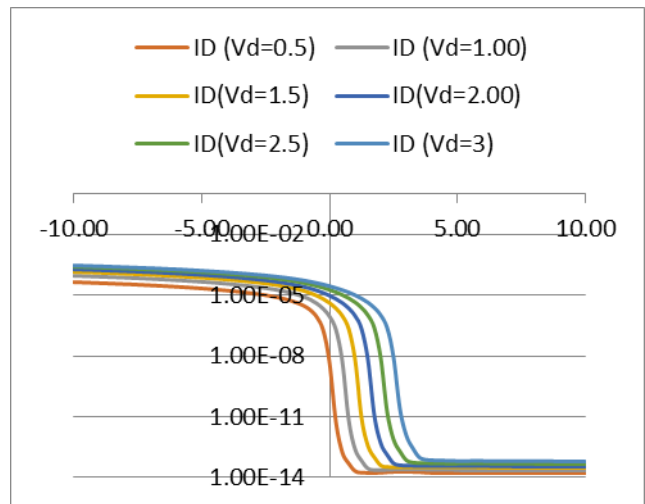


Fig.08: Ids vs Vgs curves

NW thickness 100nm:

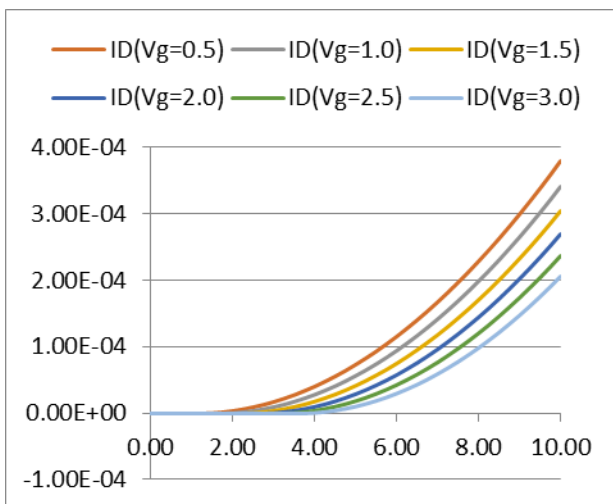


Fig.09: Ids vs Vds curves

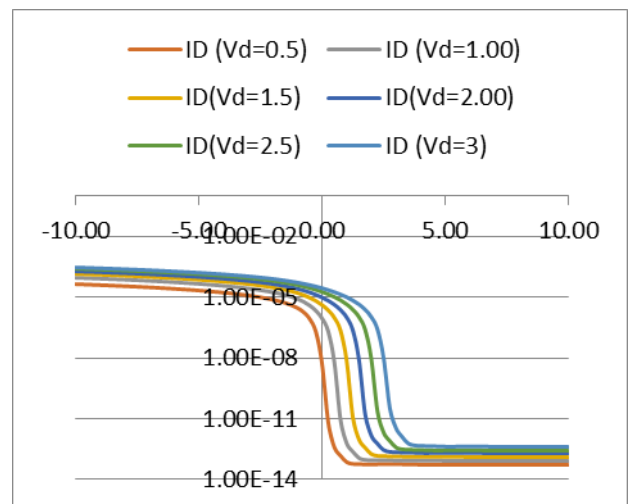


Fig.10: Ids vs Vgs curves

2. $2 \times 10^{16} / \text{cm}^3$

NW thickness 10nm:

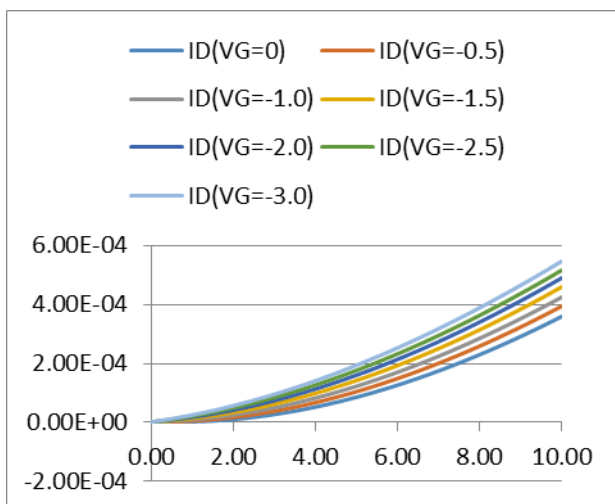


Fig.11: Ids vs Vds curves

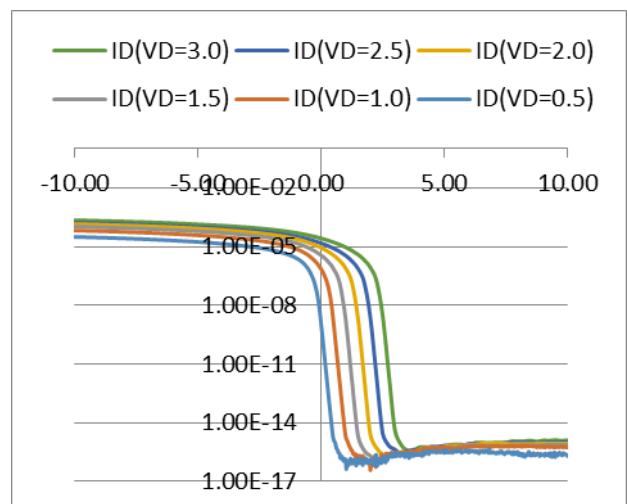


Fig.12: Ids vs Vgs curves

NW thickness 25nm:

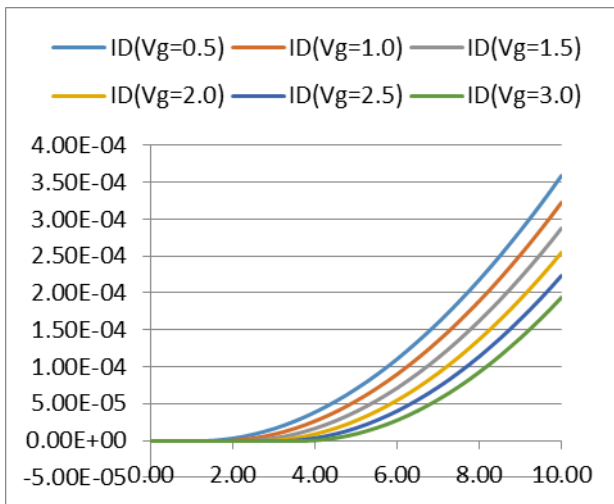


Fig.13: Ids vs Vds curves

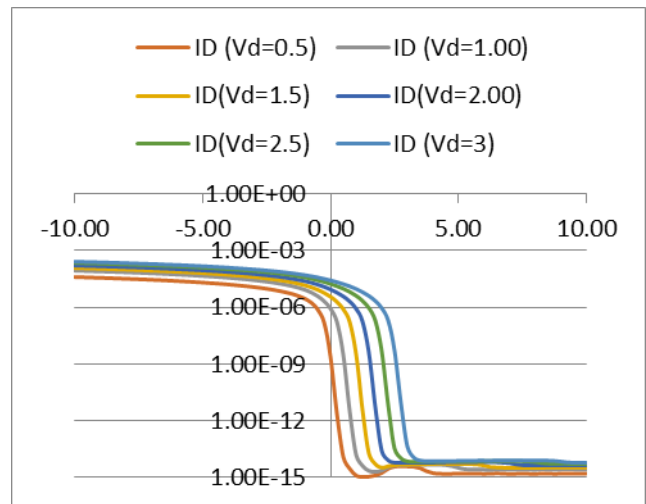


Fig.14: Ids vs Vgs curves

NW thickness 50nm:

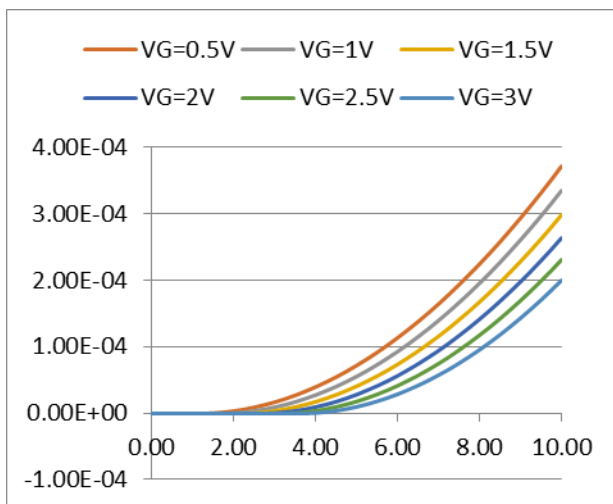


Fig.15: Ids vs Vds curves

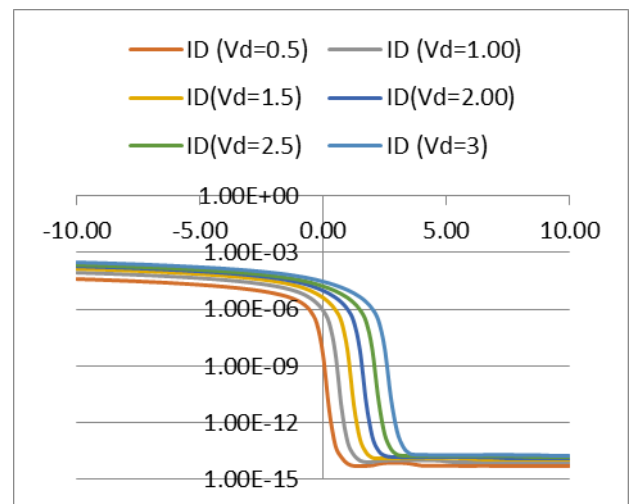


Fig.16: Ids vs Vgs curves

NW thickness 75nm:

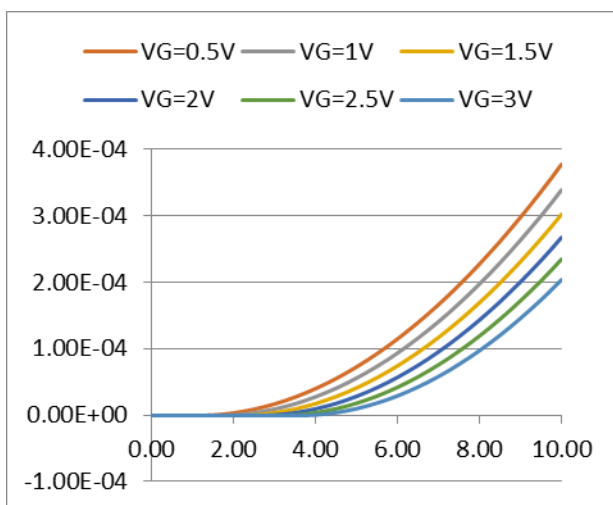


Fig.17: Ids vs Vds curves

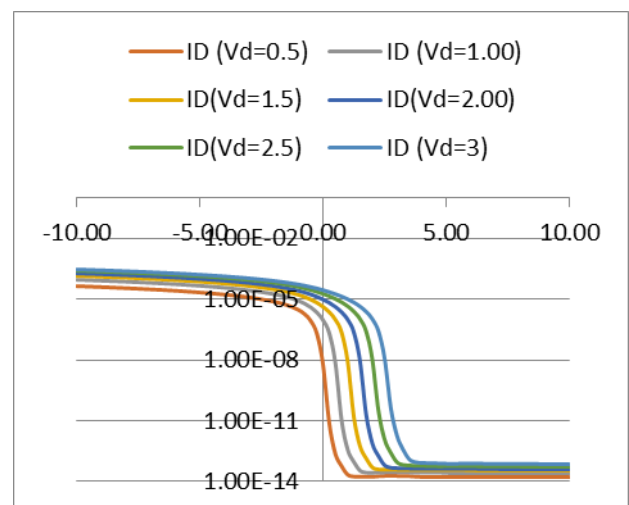


Fig.18: Ids vs Vgs curves

NW thickness 100nm:

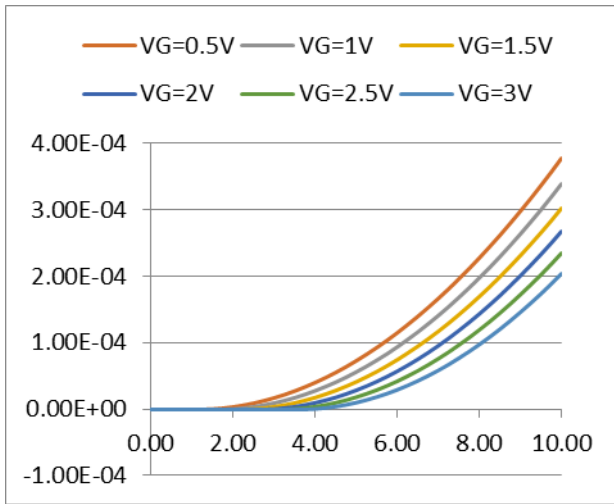


Fig.19: Ids vs Vds curves

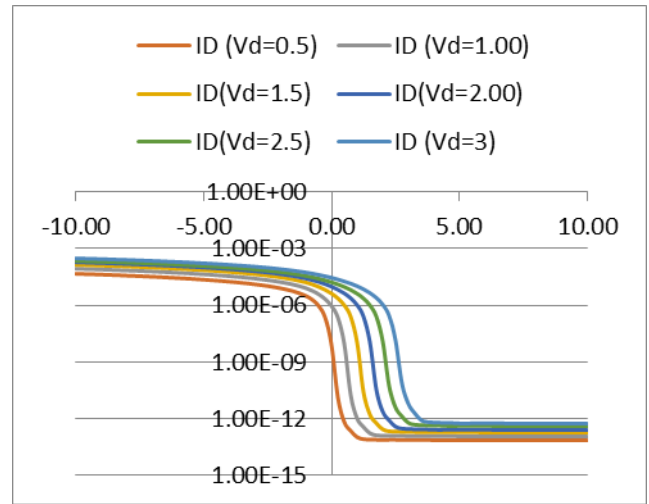


Fig.20: Ids vs Vgs curves

3. $4e16/cm^3$

NW thickness 10nm:

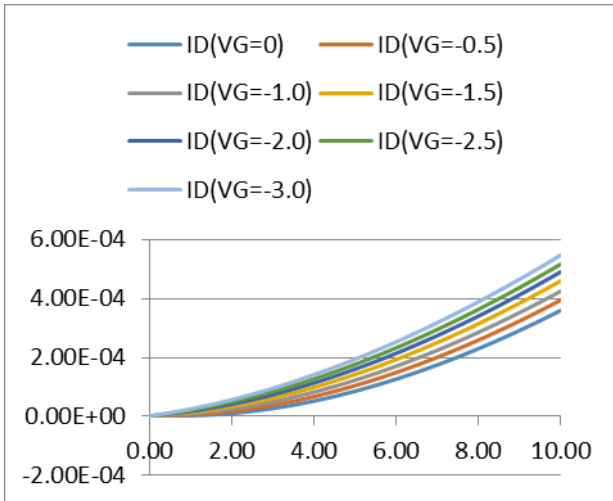


Fig.21: Ids vs Vds curves

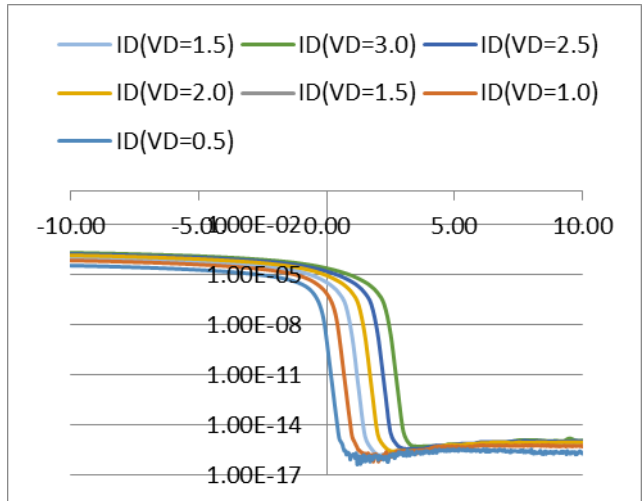


Fig.22: Ids vs Vgs curves

NW thickness 25nm:

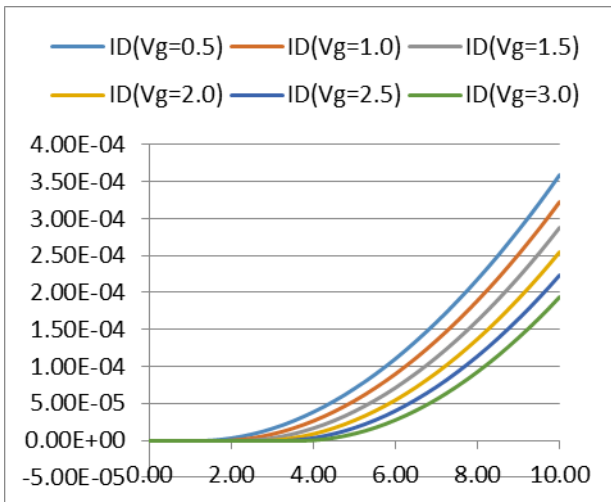


Fig.23: Ids vs Vds curves

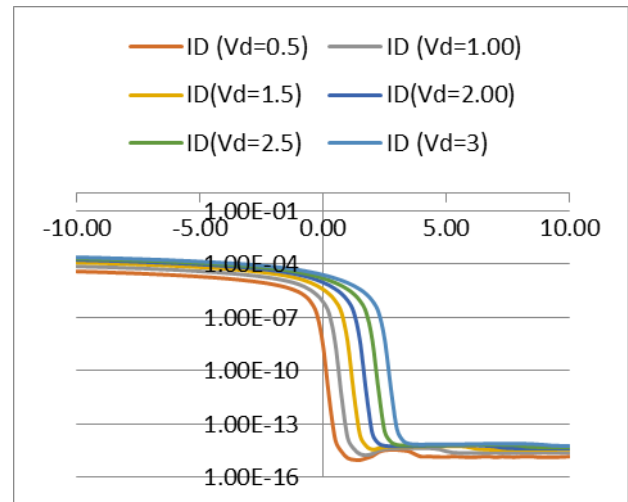


Fig.24: Ids vs Vgs curves

NW thickness 50nm:

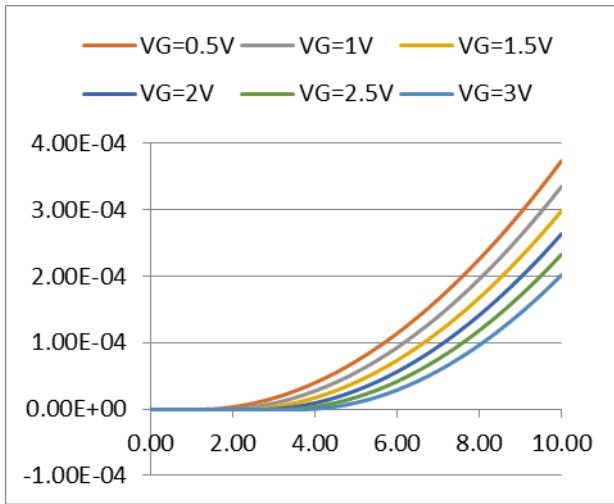


Fig.25: Ids vs Vds curves

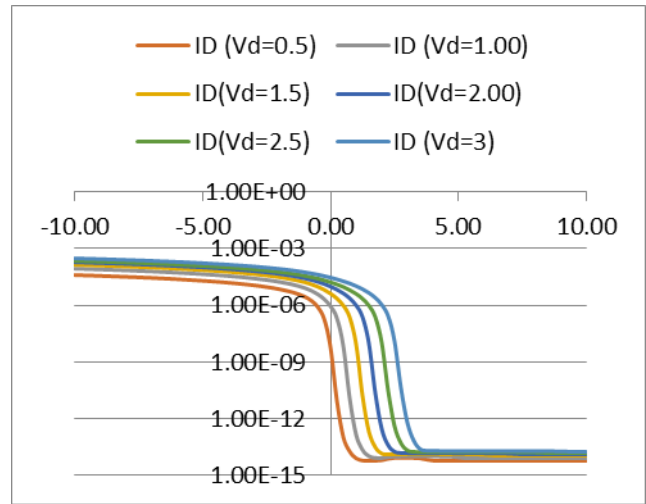


Fig.26: Ids vs Vgs curves

NW thickness 75nm:

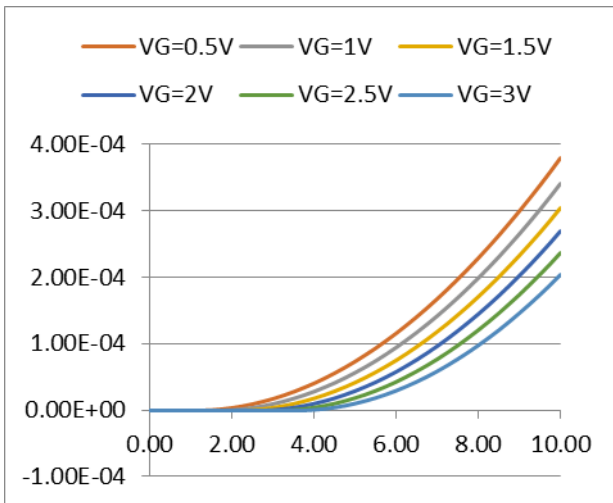


Fig.27: Ids vs Vds curves

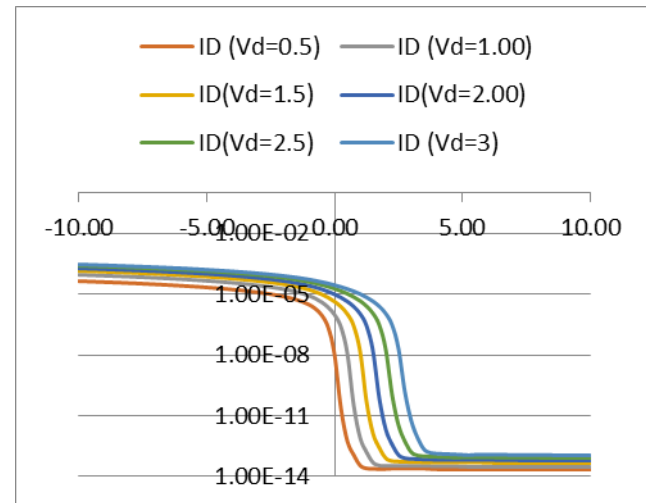


Fig.28: Ids vs Vgs curves

NW thickness 100nm:

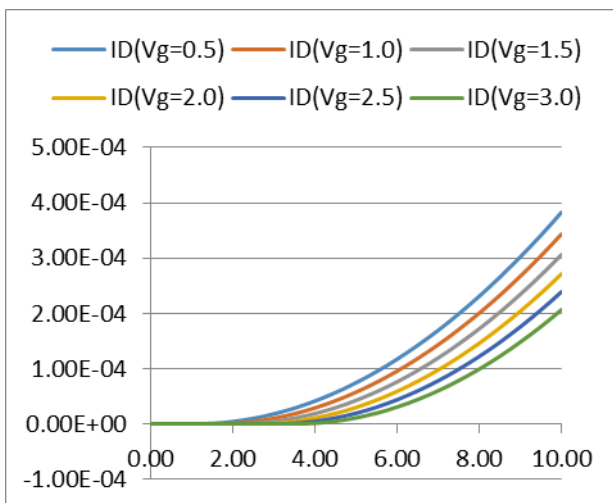


Fig.29: Ids vs Vds curves

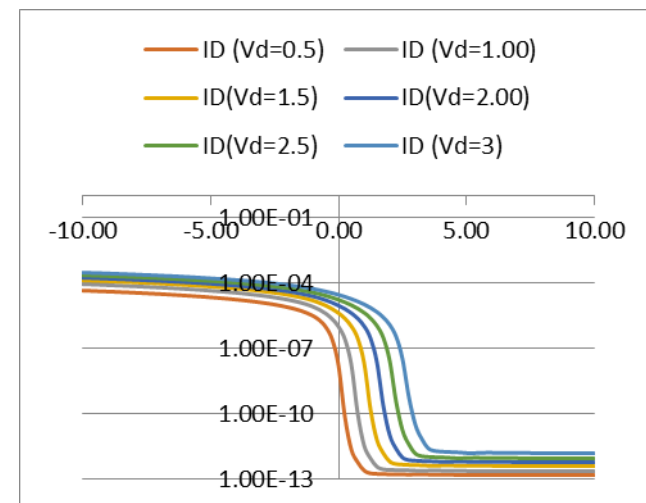


Fig.30: Ids vs Vgs curves

4. $6e16/cm^3$

NW thickness 10nm:

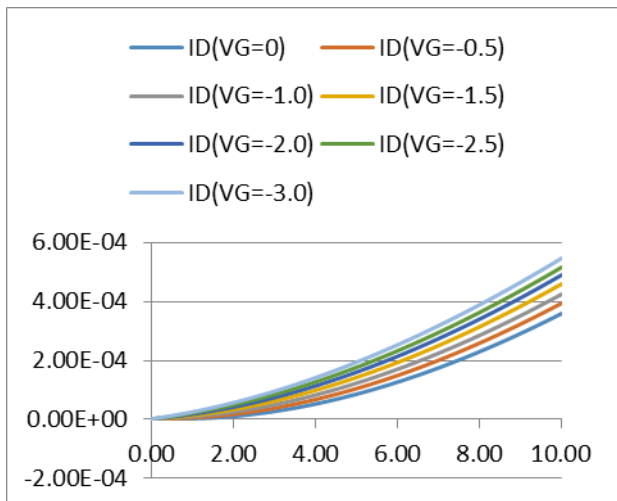


Fig.31: Ids vs Vds curves

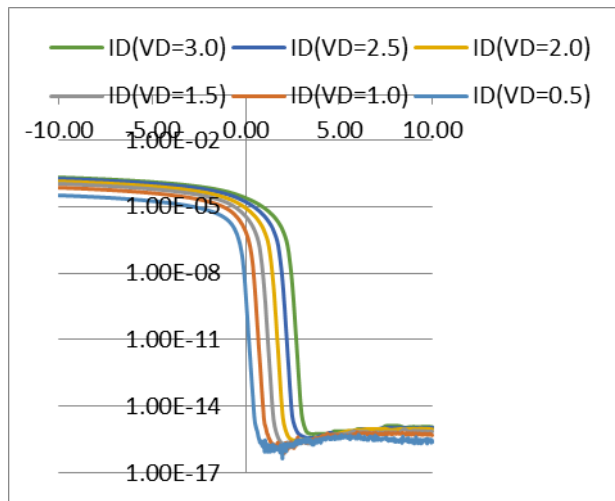


Fig.32: Ids vs Vgs curves

NW thickness 25nm:

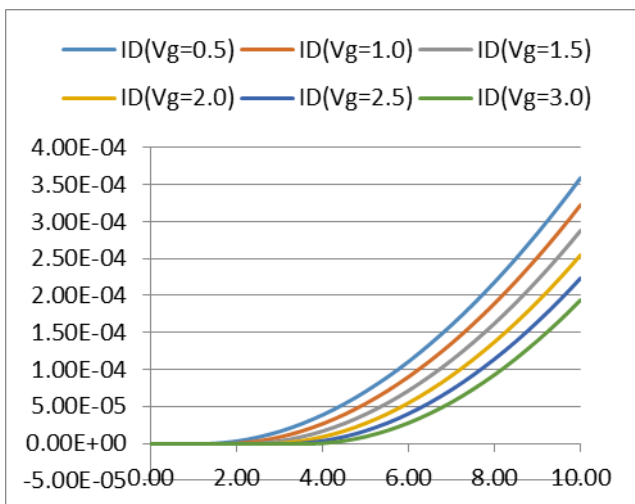


Fig.33: Ids vs Vds curves

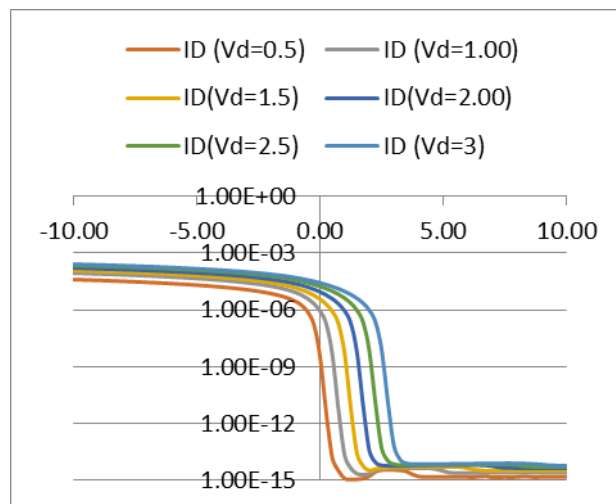


Fig.34: Ids vs Vgs curves

NW thickness 50nm:

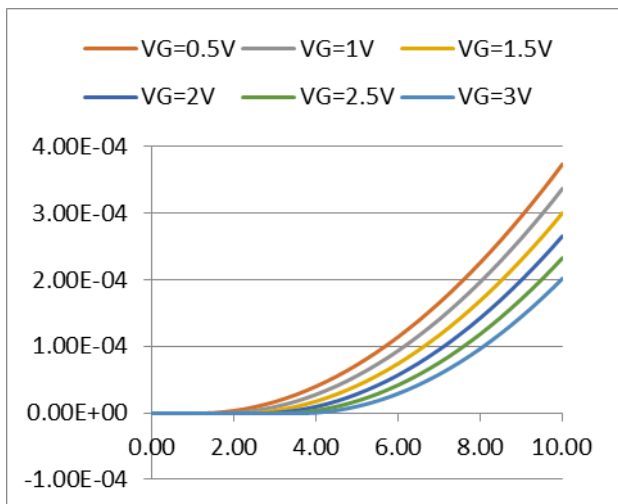


Fig.35: Ids vs Vds curves

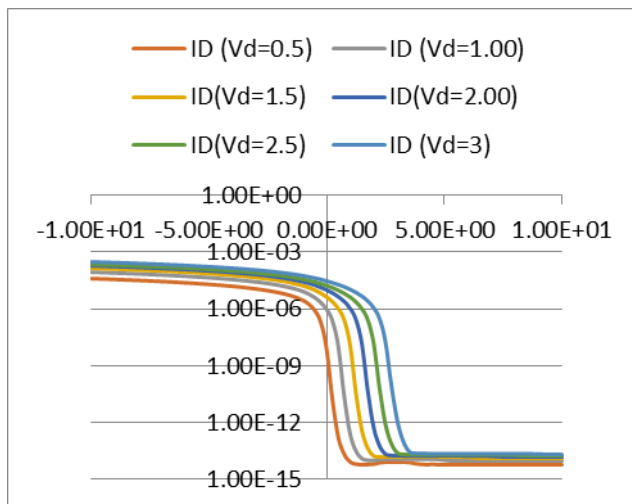


Fig.36: Ids vs Vgs curves

NW thickness 75nm:

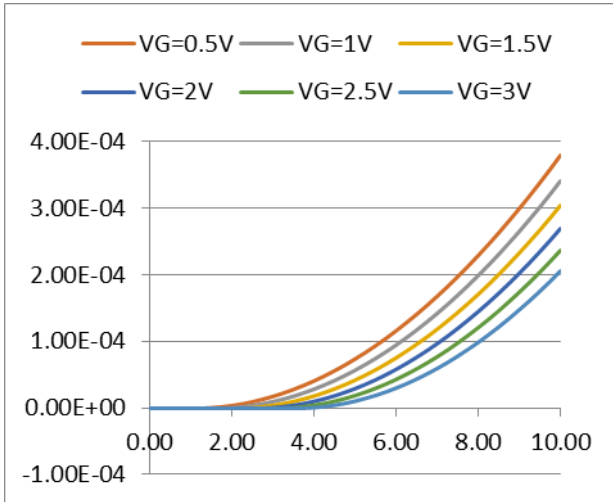


Fig.37: Ids vs Vds curves

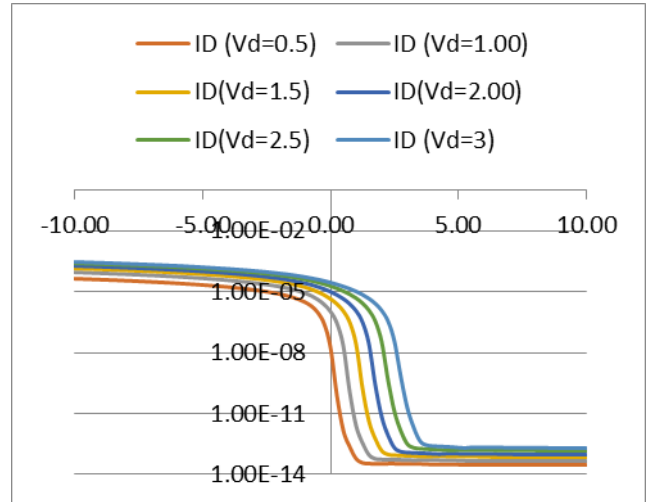


Fig.38: Ids vs Vgs curves

NW thickness 100nm:

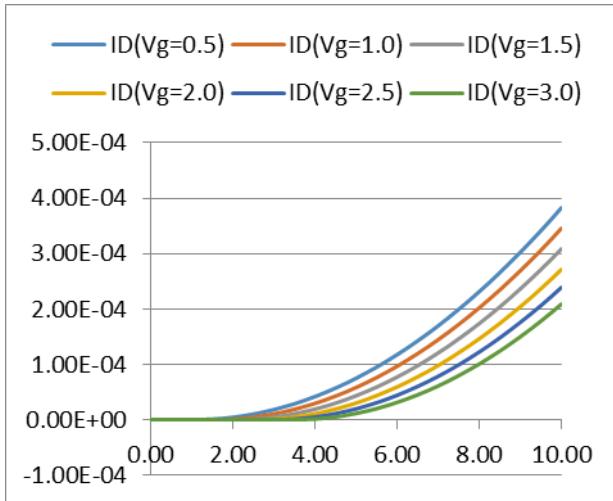


Fig.39: Ids vs Vds curves

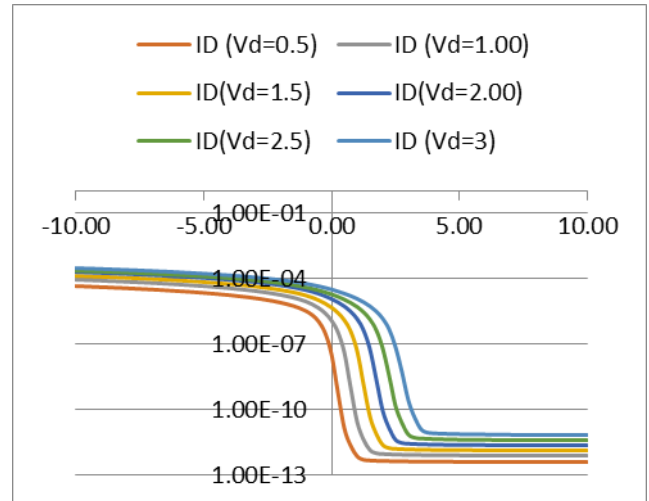


Fig.40: Ids vs Vgs curves

5. $8e16/cm^3$

NW thickness 10nm:

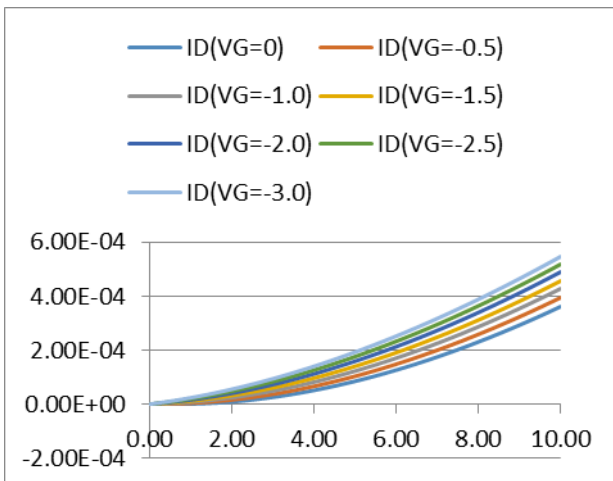


Fig.41: Ids vs Vds curves

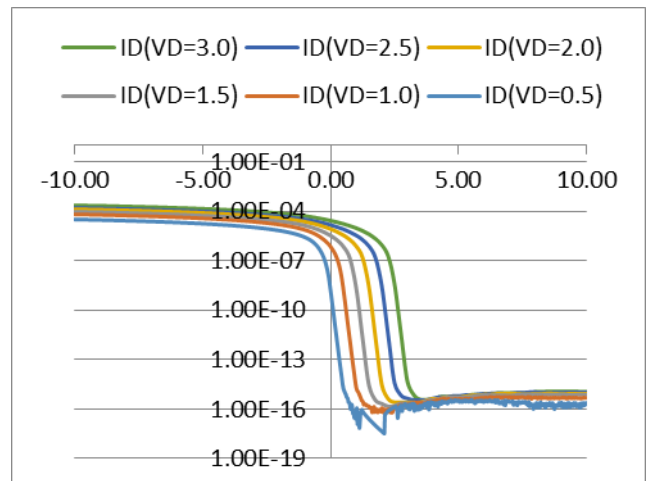


Fig.42: Ids vs Vgs curves

NW thickness 25nm:

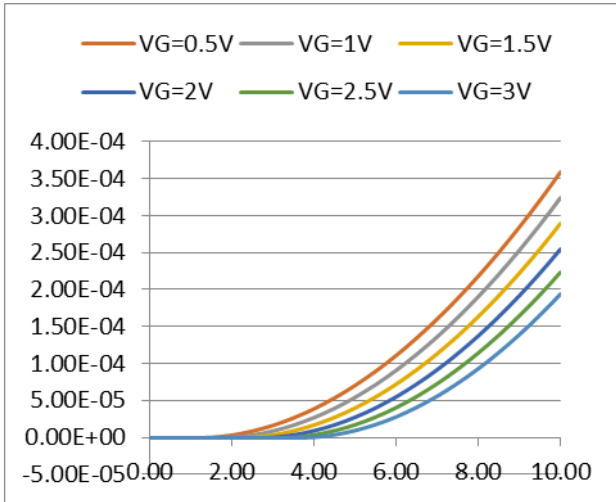


Fig.43: Ids vs Vds curves

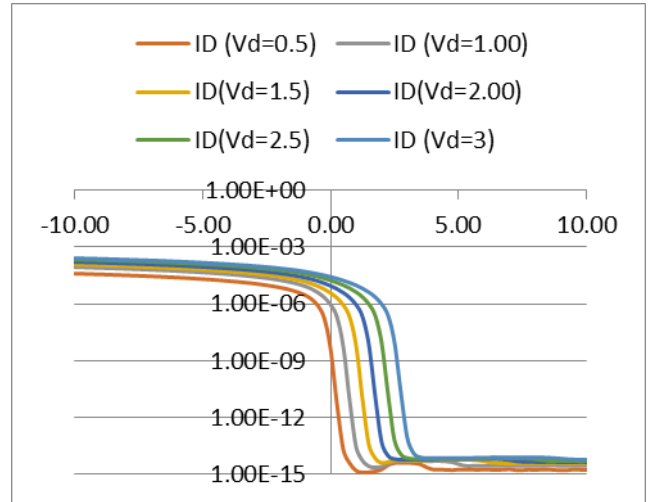


Fig.44: Ids vs Vgs curves

NW thickness 50nm:

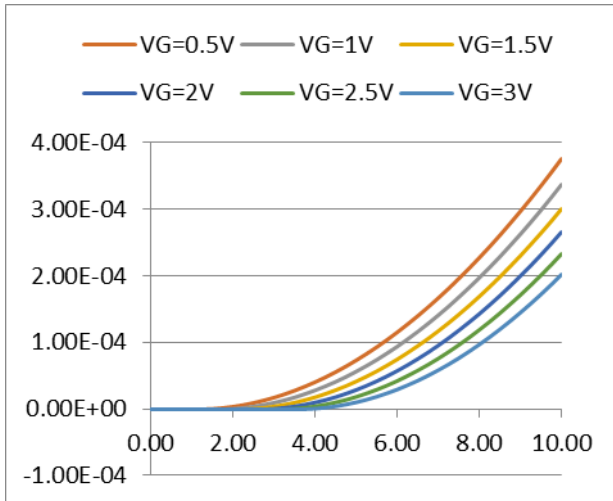


Fig.45: Ids vs Vds curves

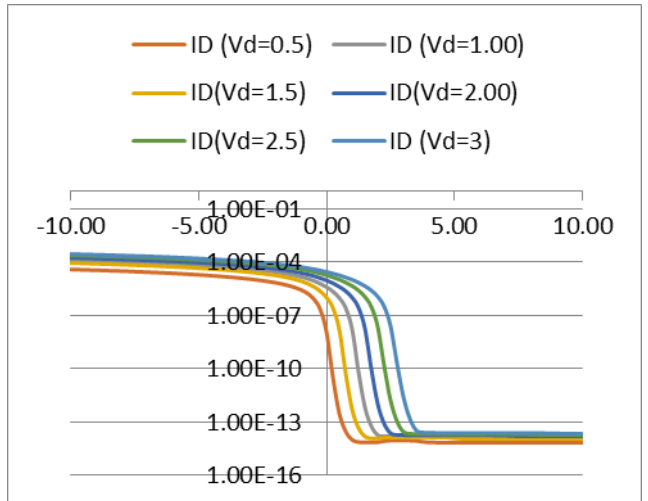


Fig.46: Ids vs Vgs curves

NW thickness 75nm:

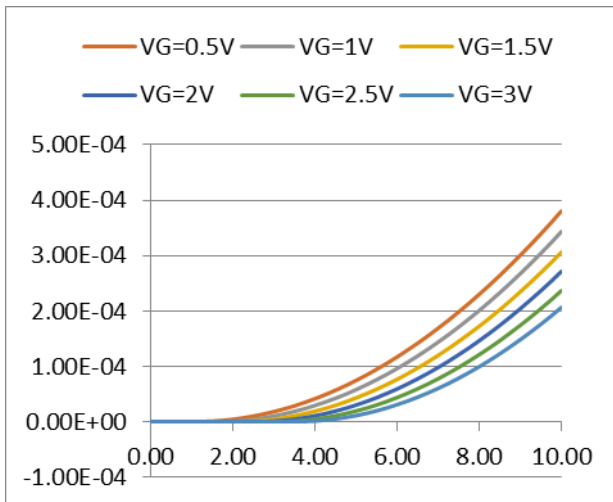


Fig.47: Ids vs Vds curves

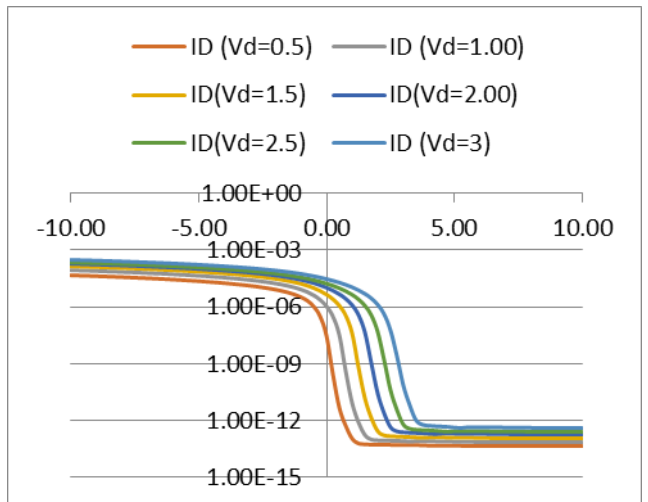


Fig.48: Ids vs Vgs curve

NW thickness 100nm:

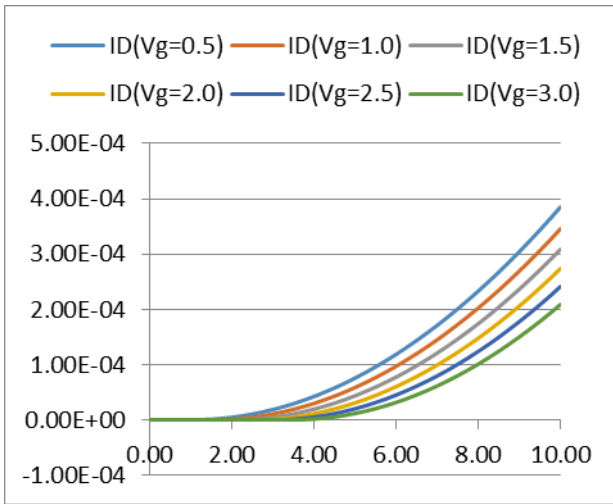


Fig.49: Ids vs Vds curves

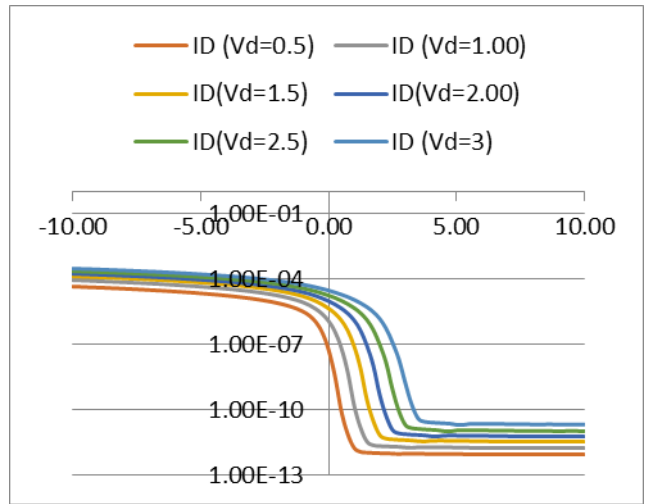


Fig.50: Ids vs Vgs curves

6. $1e17/cm^3$

NW thickness 10nm:

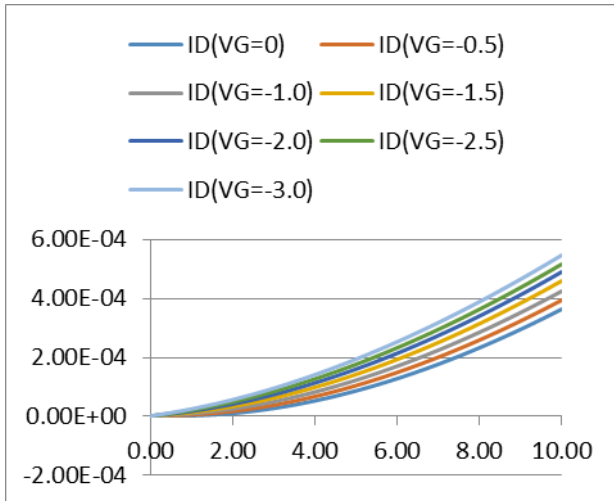


Fig.51: Ids vs Vds curves

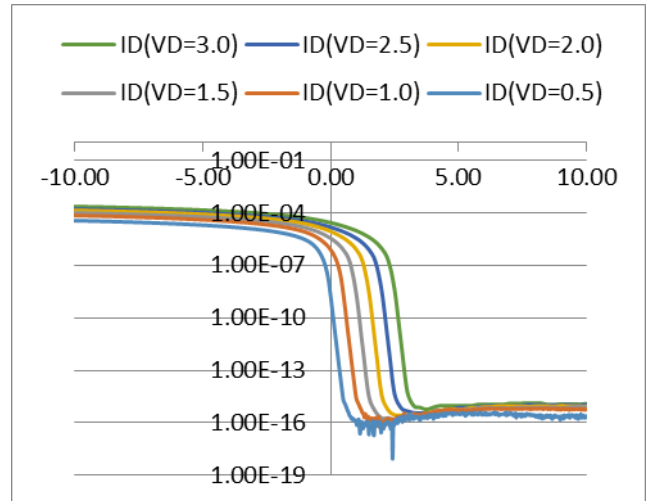


Fig.52: Ids vs Vgs curves

NW thickness 25nm:

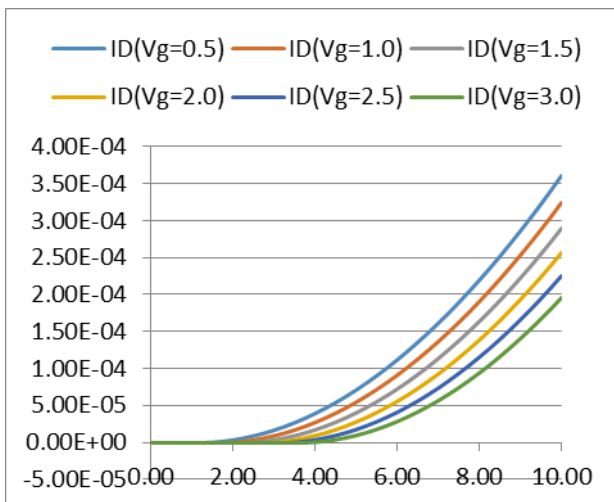


Fig.53: Ids vs Vds curves

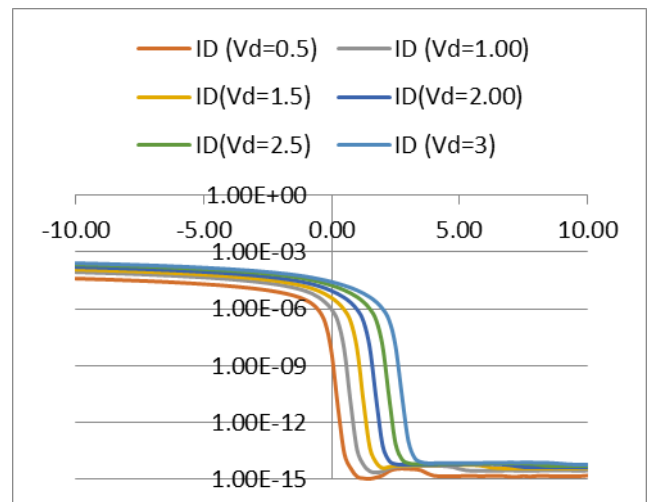


Fig.54: Ids vs Vgs curves

NW thickness 50nm:

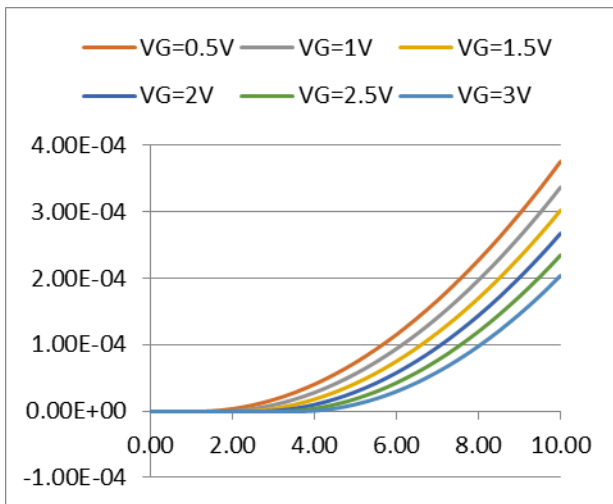


Fig.55: Ids vs Vds curves

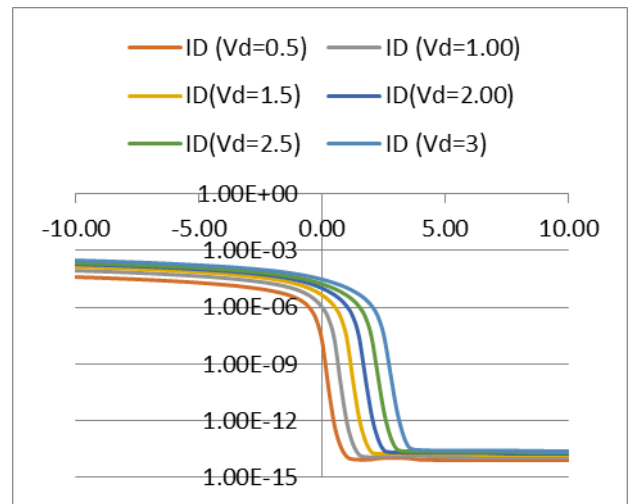


Fig.56: Ids vs Vgs curves

NW thickness 75nm:

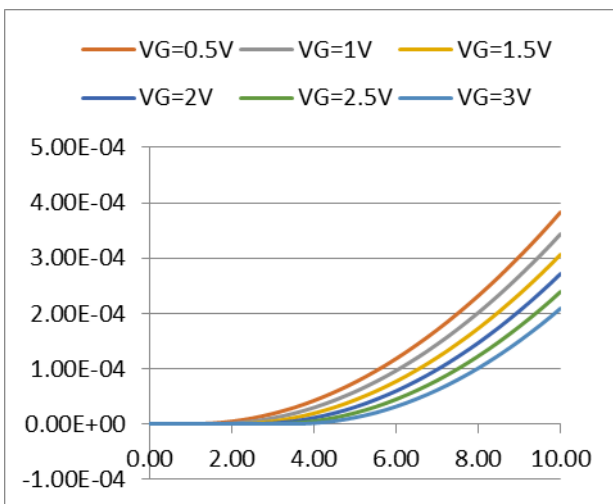


Fig.57: Ids vs Vds curves

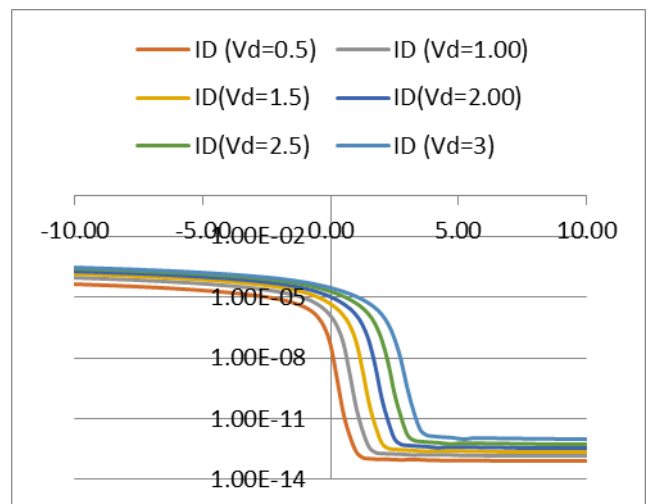


Fig.58: Ids vs Vgs curves

NW thickness 100nm:

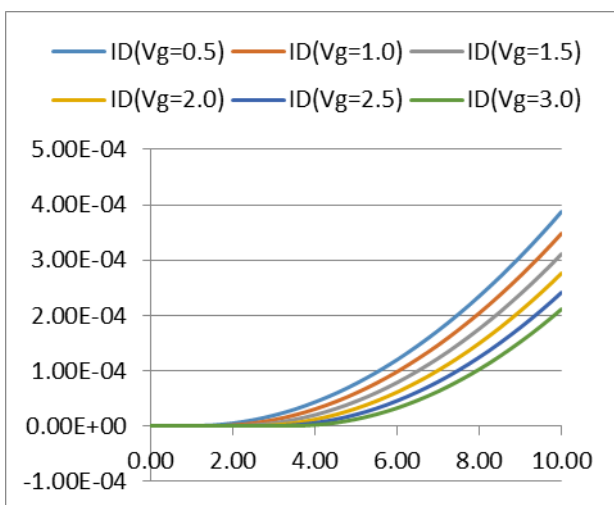


Fig.59: Ids vs Vds curves

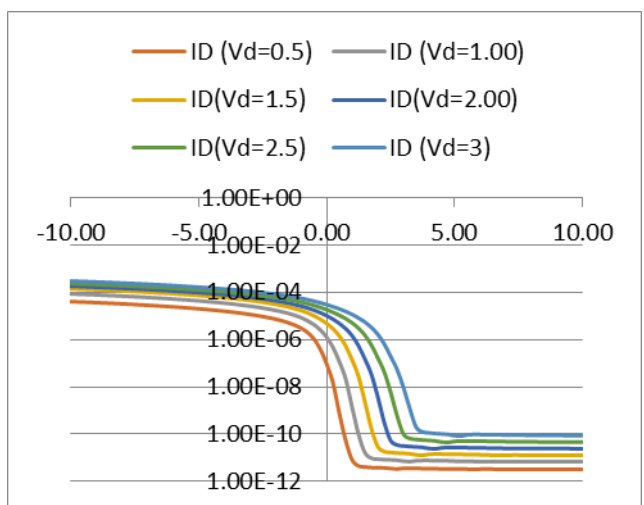


Fig.60: Ids vs Vgs curves

7. $2e17/cm^3$

NW thickness 10nm:

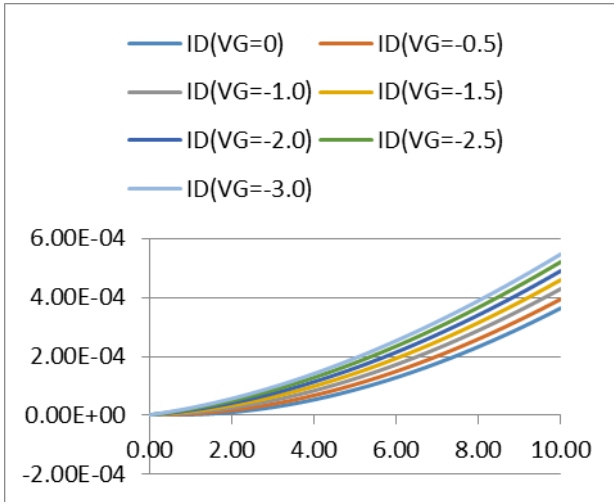


Fig.61: Ids vs Vds curves

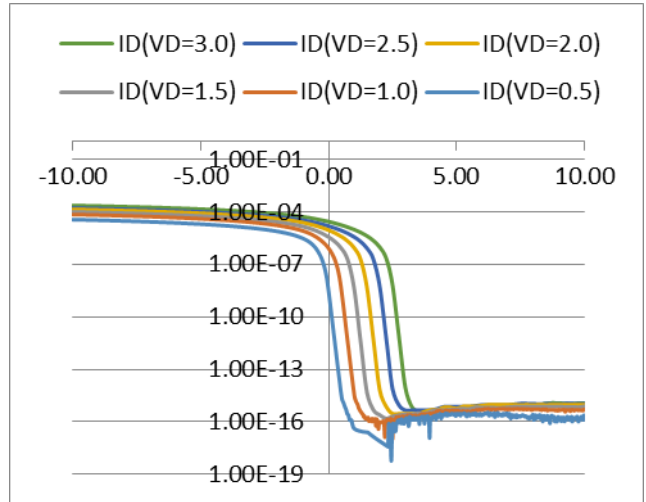


Fig.62: Ids vs Vgs curves

NW thickness 25nm:

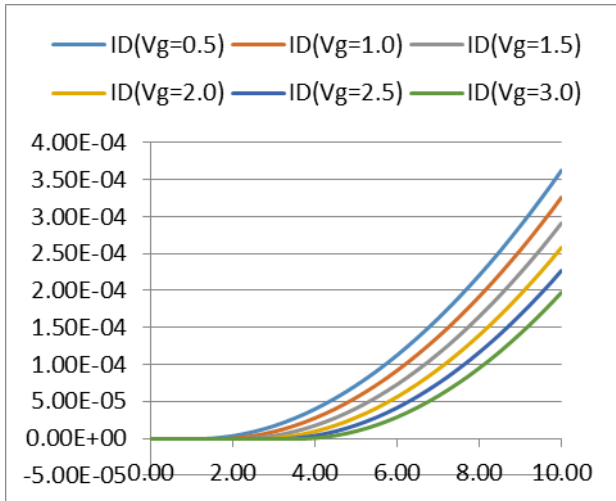


Fig.63: Ids vs Vds curves

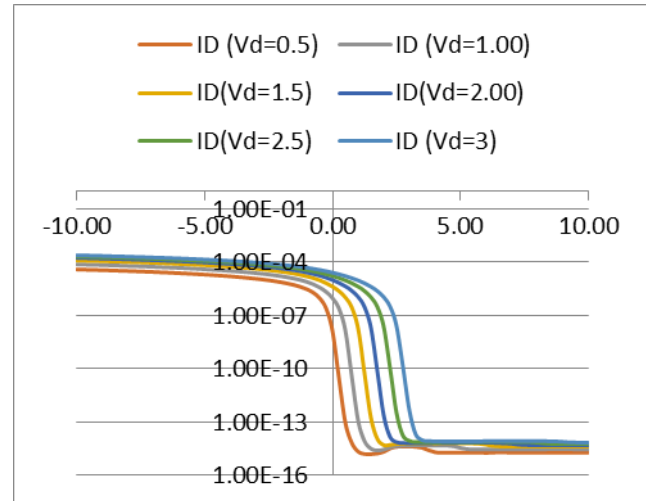


Fig.64: Ids vs Vgs curves

NW thickness 50nm:

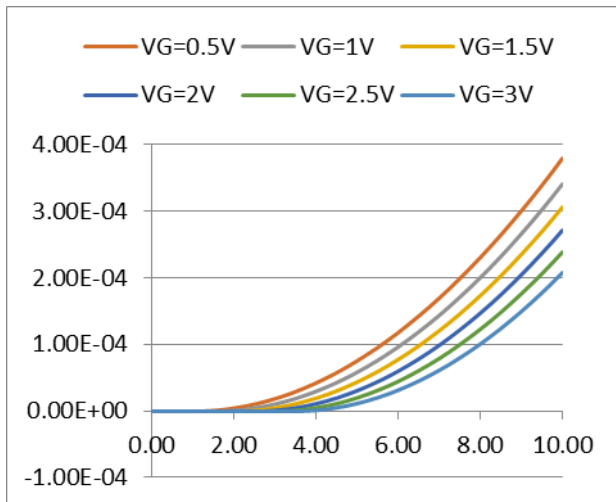


Fig.65: Ids vs Vds curves

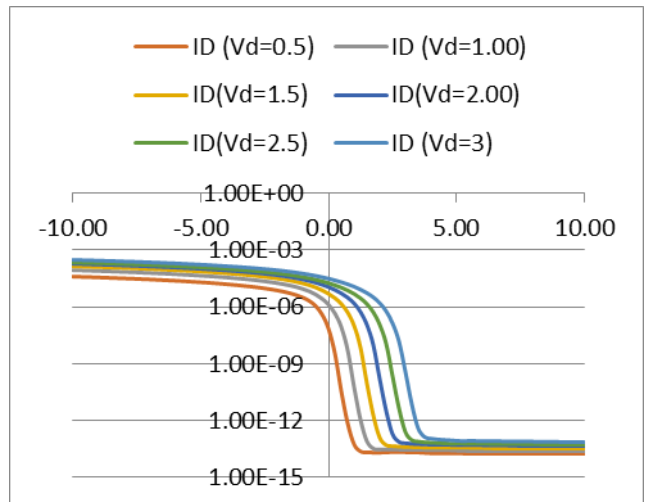


Fig.66: Ids vs Vgs curves

NW thickness 75nm:

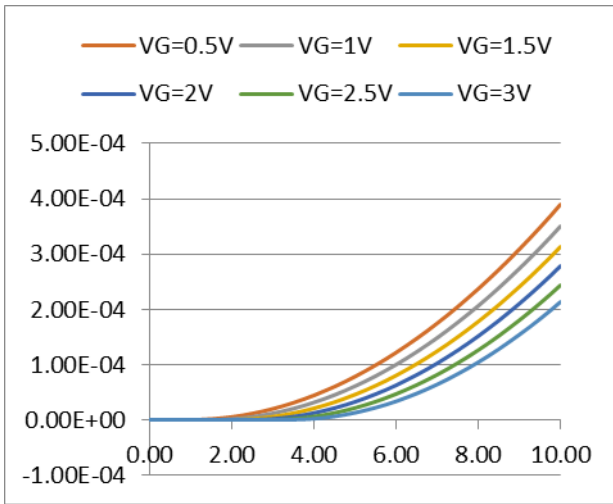


Fig.67: Ids vs Vds curves

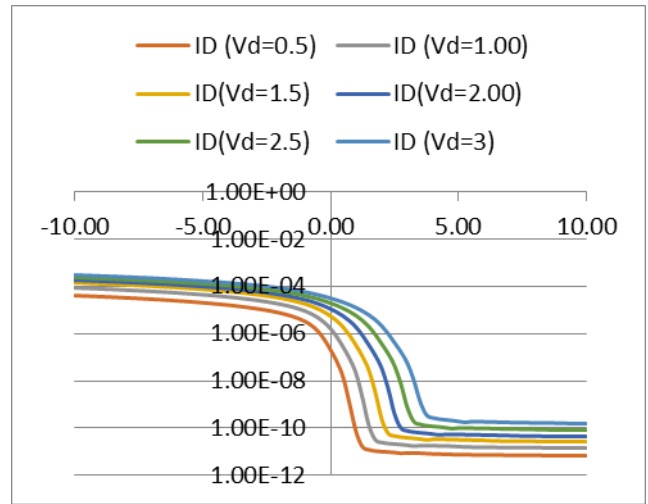


Fig.68: Ids vs Vgs curve

NW thickness 100nm:

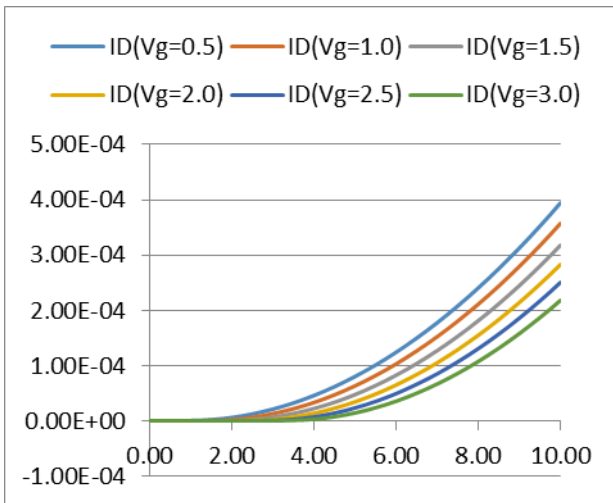


Fig.69: Ids vs Vds curves

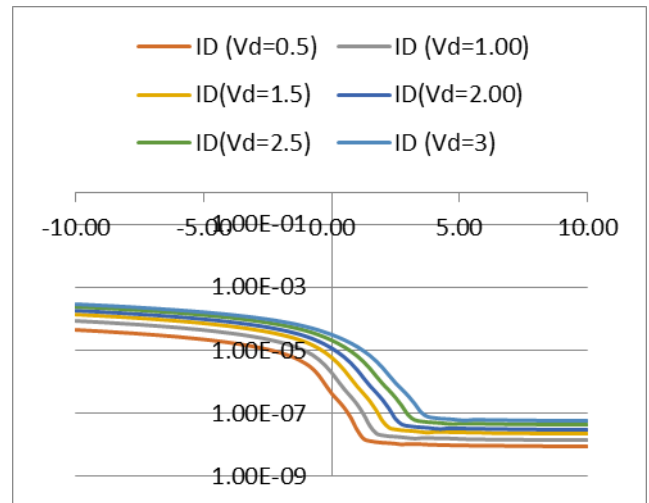


Fig.70: Ids vs Vgs curves

8. $4e17/cm^3$

NW thickness 10nm:

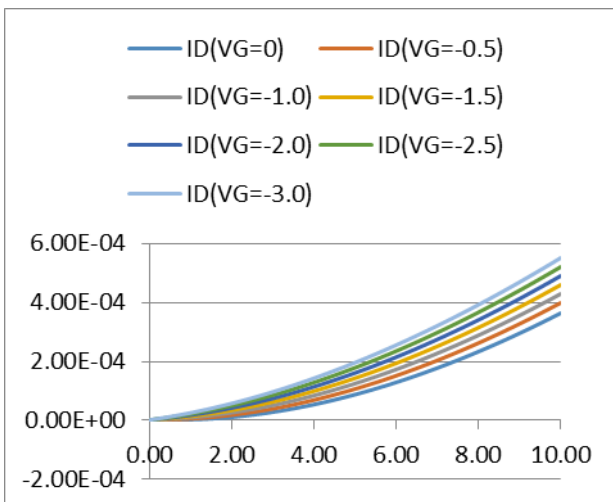


Fig.71: Ids vs Vds curves

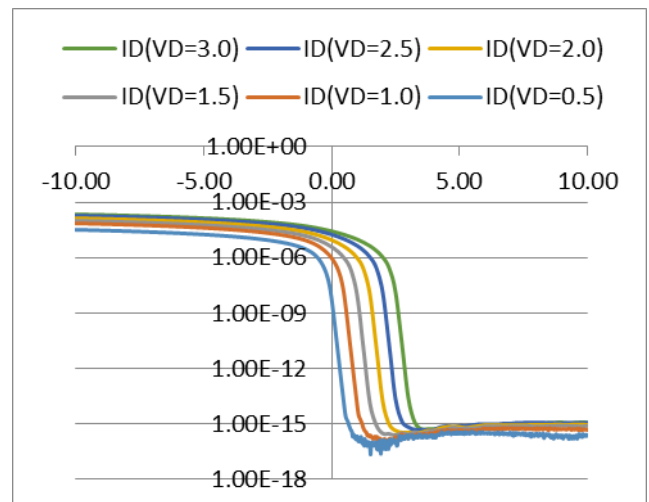


Fig.72: Ids vs Vgs curves

NW thickness 25nm:

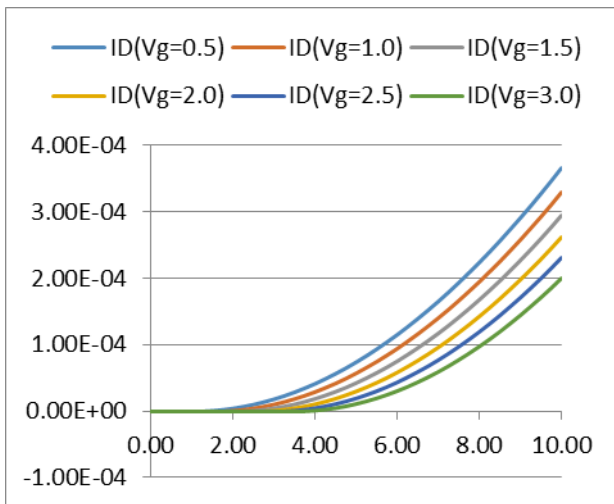


Fig.73: Ids vs Vds curves

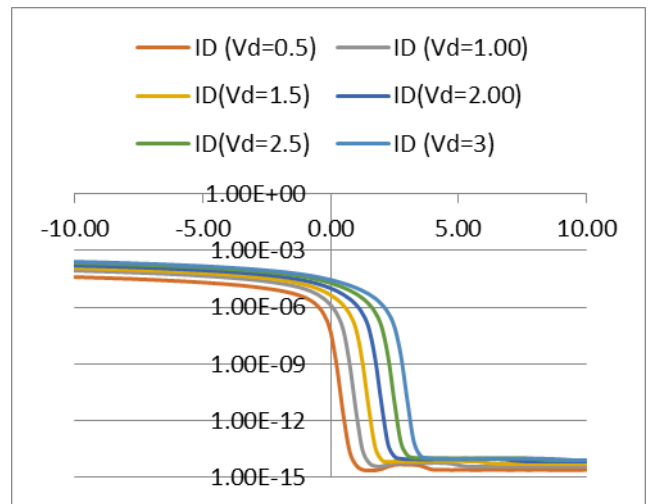


Fig.74: Ids vs Vgs curves

NW thickness 50nm:

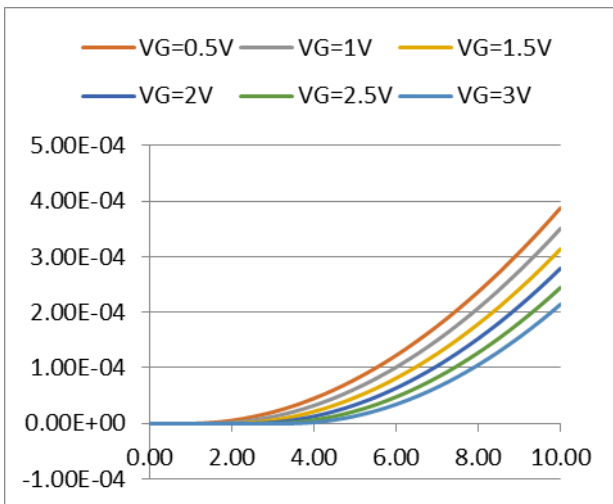


Fig.75: Ids vs Vds curves

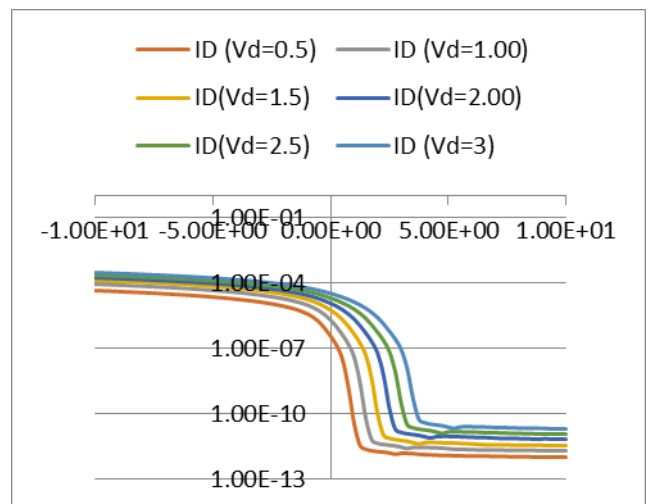


Fig.76: Ids vs Vgs curves

NW thickness 75nm:

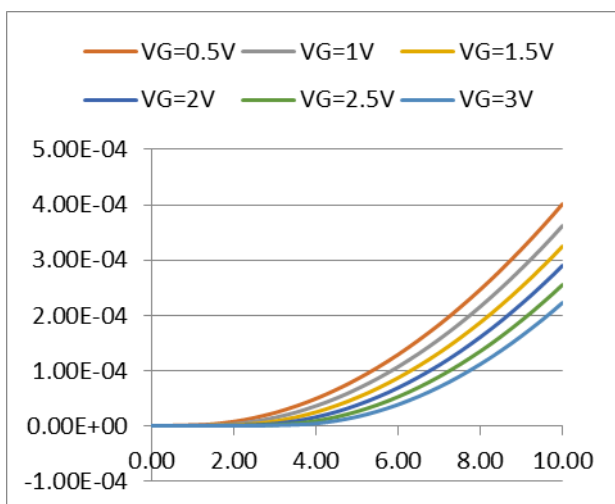


Fig.77: Ids vs Vds curves

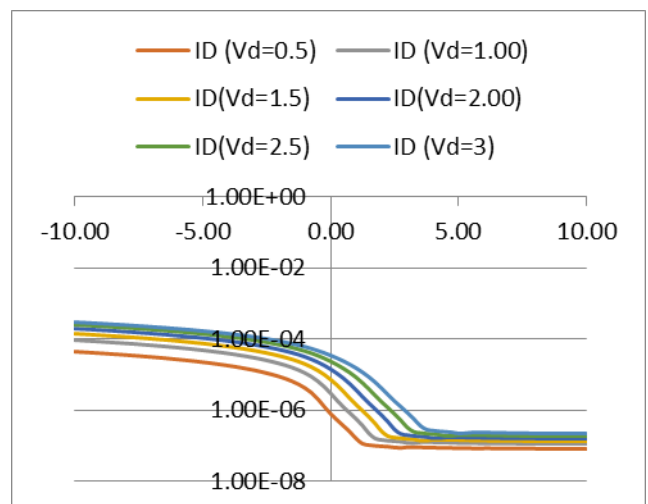


Fig.78: Ids vs Vgs curves

NW thickness 100nm:

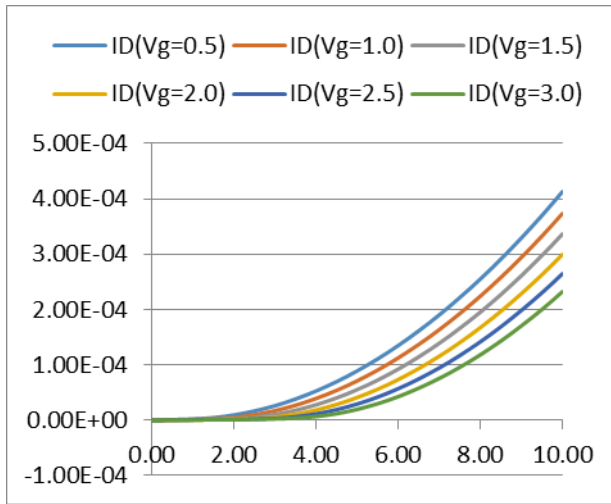


Fig.79: Ids vs Vds curves

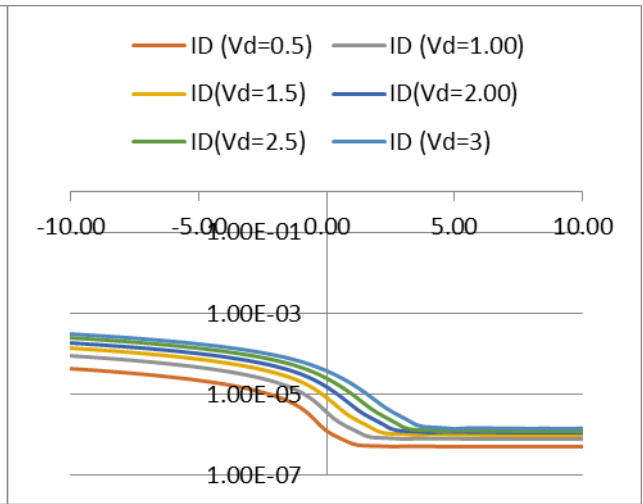


Fig.80: Ids vs Vgs curves

9. $6e17/cm^3$

NW thickness 10nm:

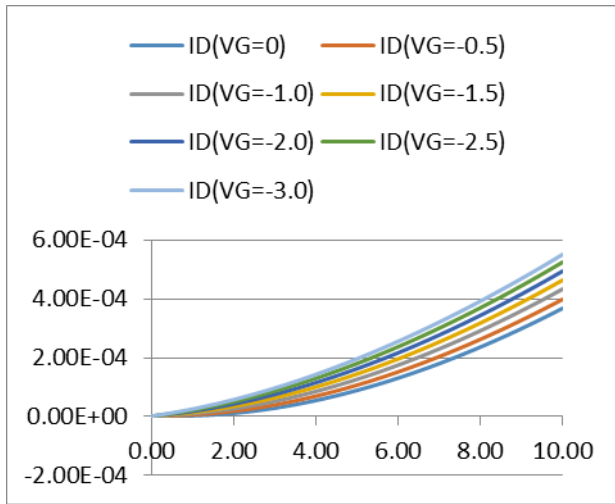


Fig.81: Ids vs Vds curves

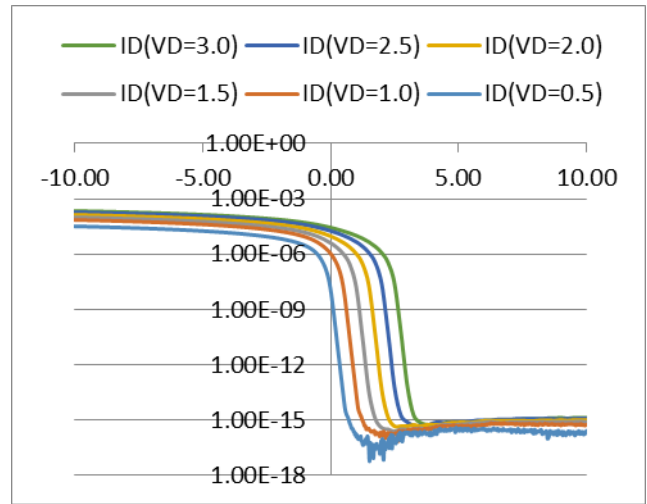


Fig.82: Ids vs Vgs curves

NW thickness 25m:

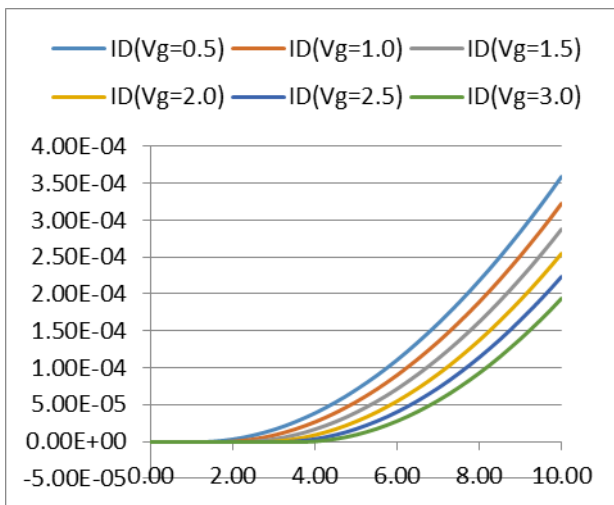


Fig.83: Ids vs Vds curves

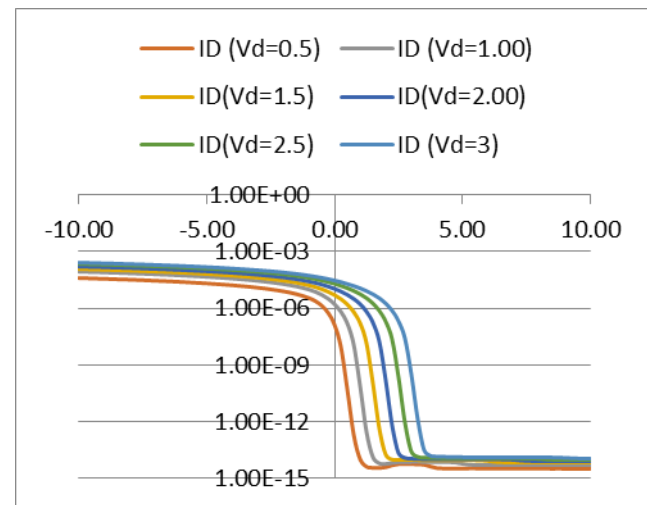


Fig.84: Ids vs Vgs curves

NW thickness 50m:

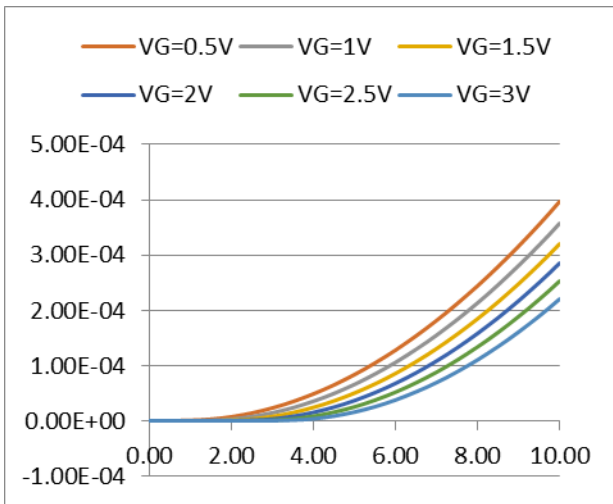


Fig.85: Ids vs Vds curves

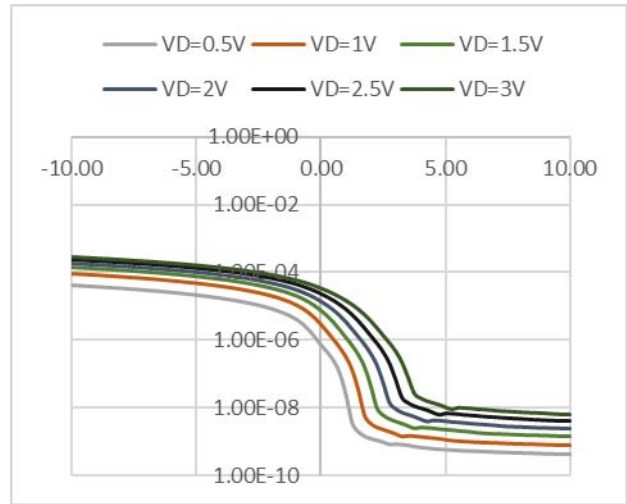


Fig.86: Ids vs Vgs curves

NW thickness 75m:

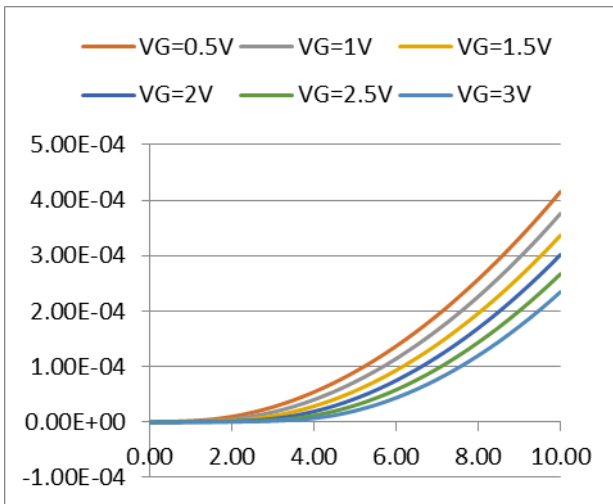


Fig.87: Ids vs Vds curves

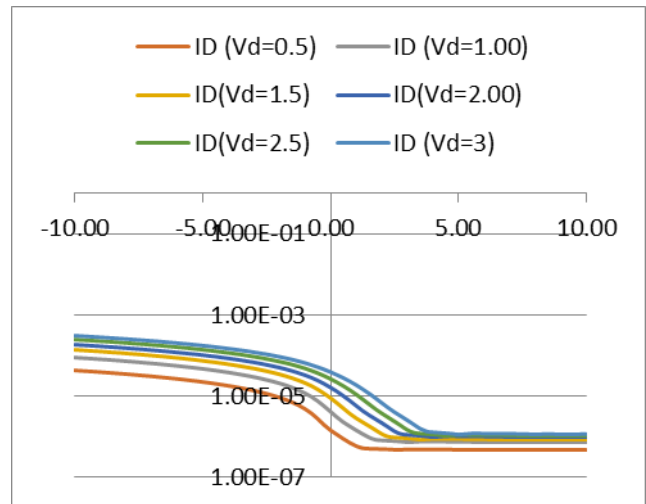


Fig.88: Ids vs Vgs curves

NW thickness 100m:

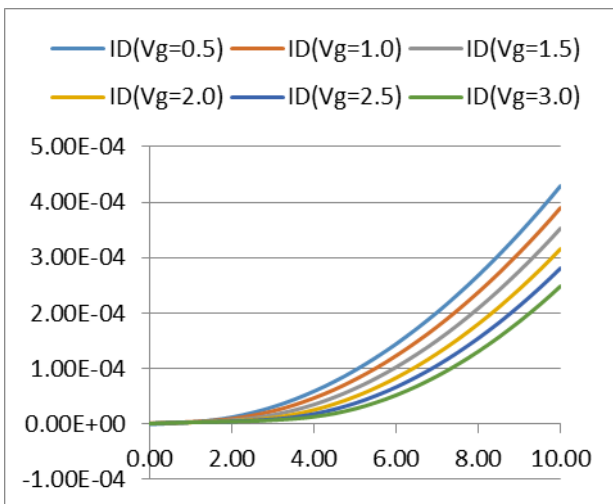


Fig.89: Ids vs Vds curves

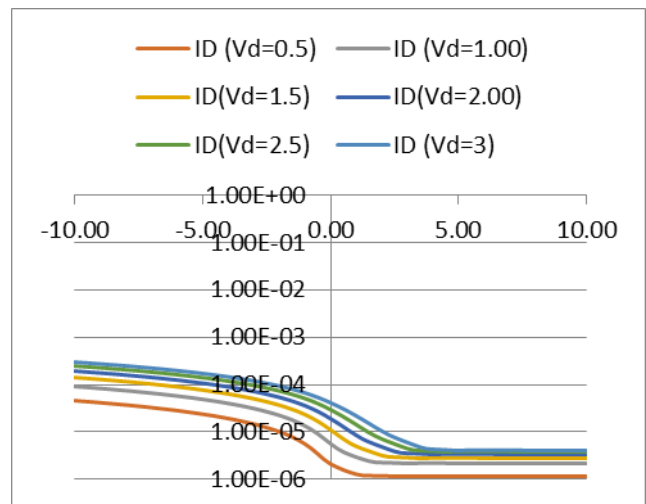


Fig.90: Ids vs Vgs curves

10. 8e17/cm³

NW thickness 10nm:

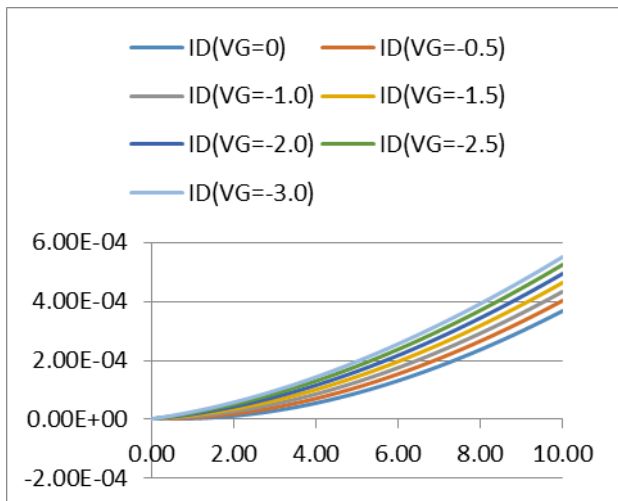


Fig.91: Ids vs Vds curves

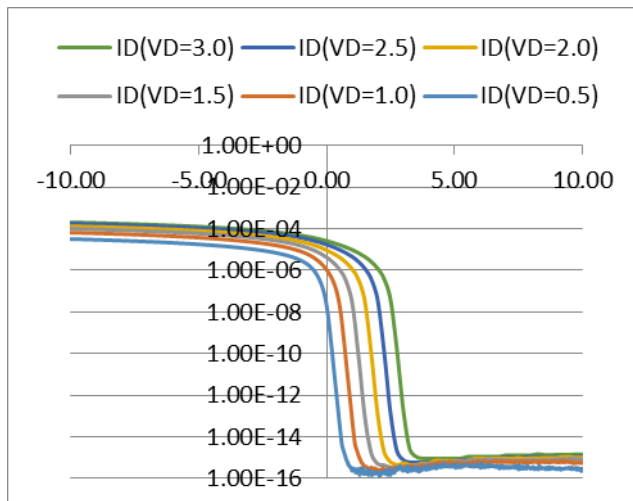


Fig.92: Ids vs Vgs curves

NW thickness 25nm:

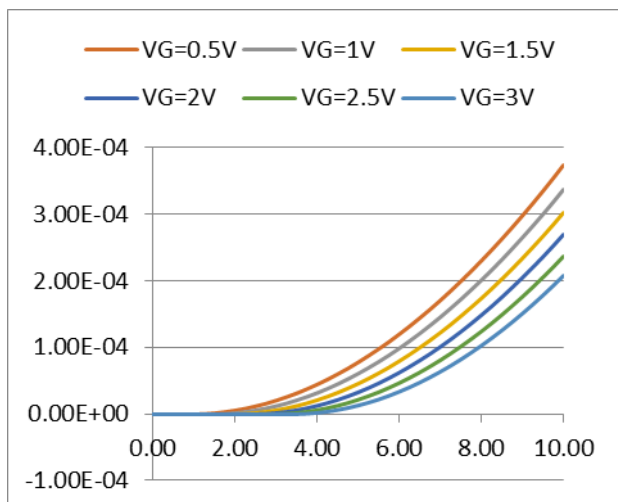


Fig.93: Ids vs Vds curves

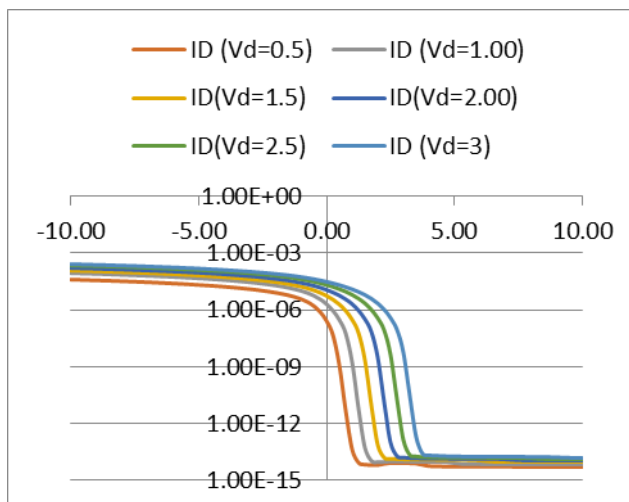


Fig.94: Ids vs Vgs curves

NW thickness 50nm:

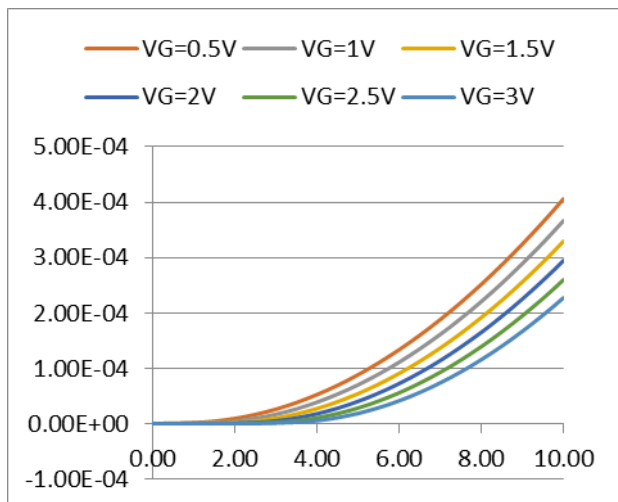


Fig.95: Ids vs Vds curves

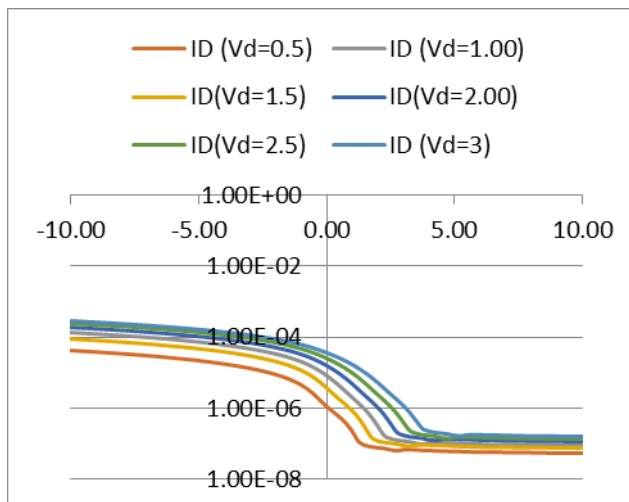


Fig.96: Ids vs Vgs curves

NW thickness 75nm:

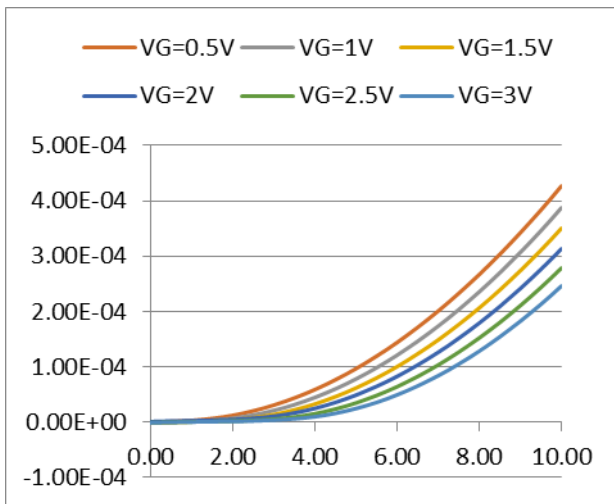


Fig.97: Ids vs Vds curves

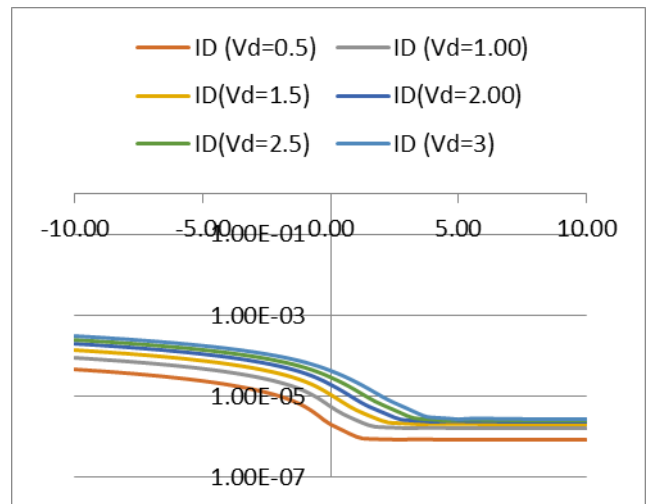


Fig.98: Ids vs Vgs curves

NW thickness 100nm:

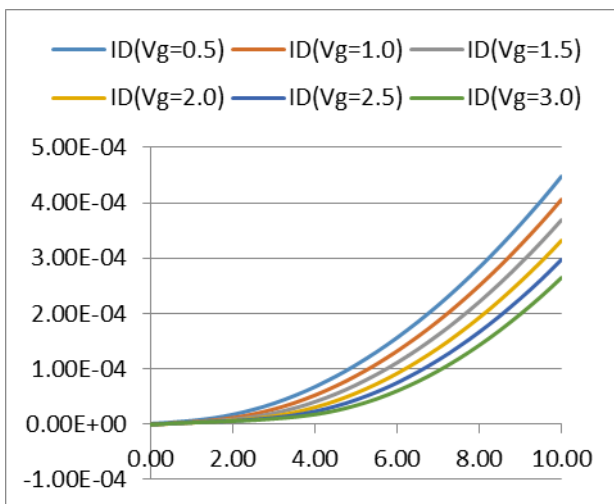


Fig.99: Ids vs Vds curves

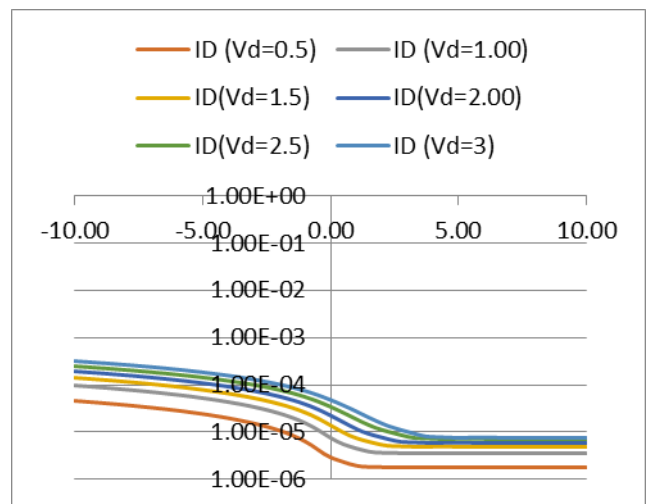


Fig.100: Ids vs Vgs curves

11. $1e18/cm^3$

NW thickness 10nm:

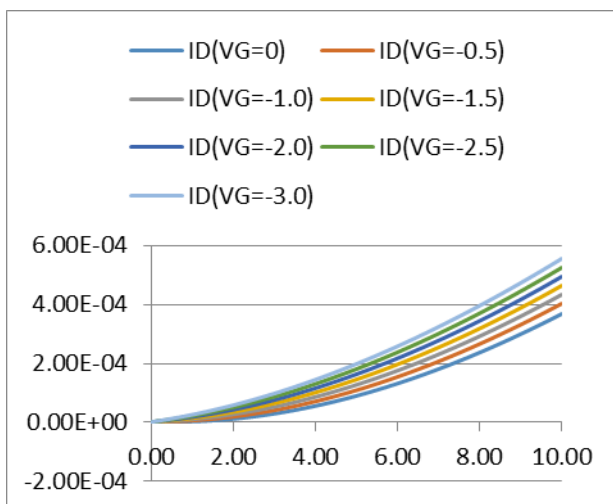


Fig.101: Ids vs Vds curves

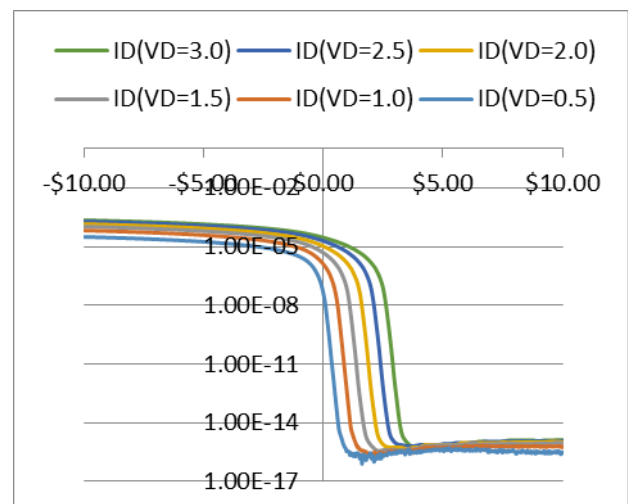


Fig.102: Ids vs Vgs curves

NW thickness 25nm:

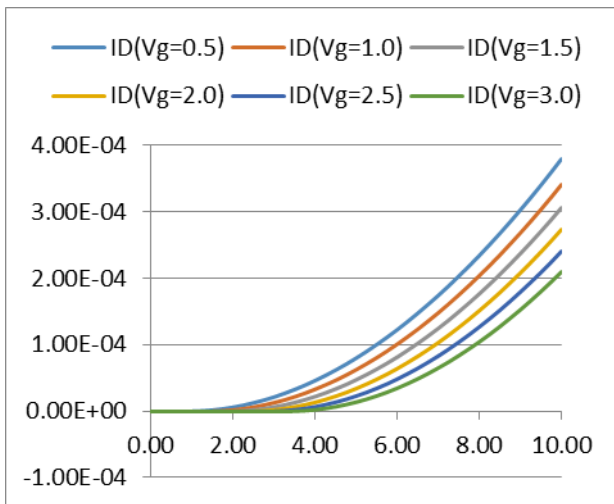


Fig.103: Ids vs Vds curves

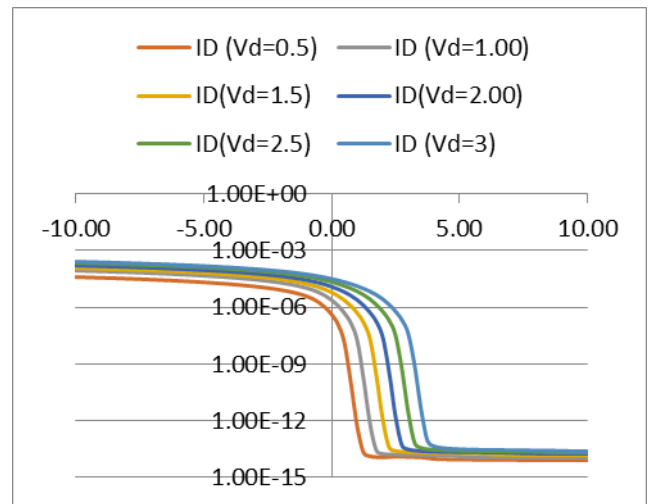


Fig.104: Ids vs Vgs curves

NW thickness 50nm:

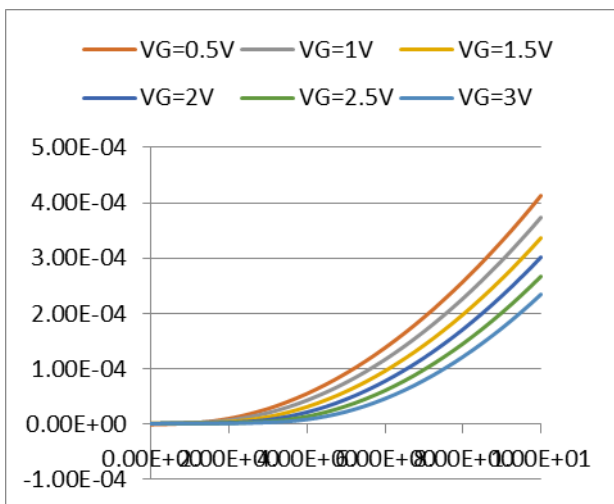


Fig.105: Ids vs Vds curves

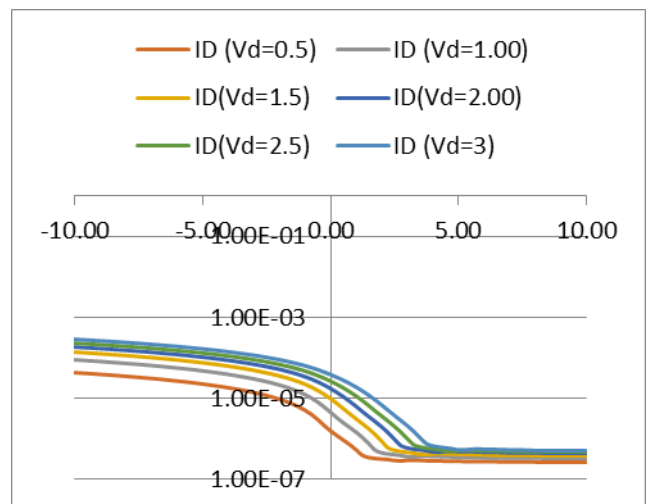


Fig.106: Ids vs Vgs curves

NW thickness 75nm:

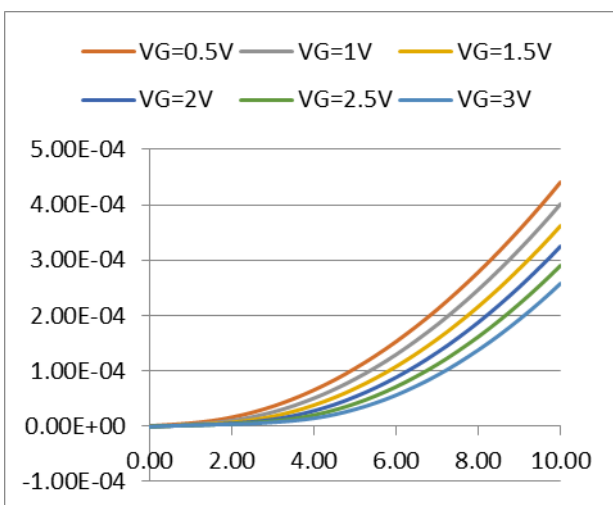


Fig.107: Ids vs Vds curves

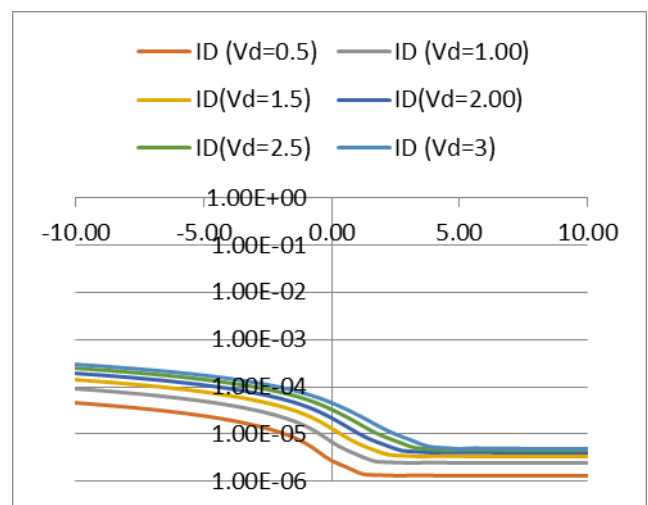


Fig.108: Ids vs Vgs curves

NW thickness 100nm:

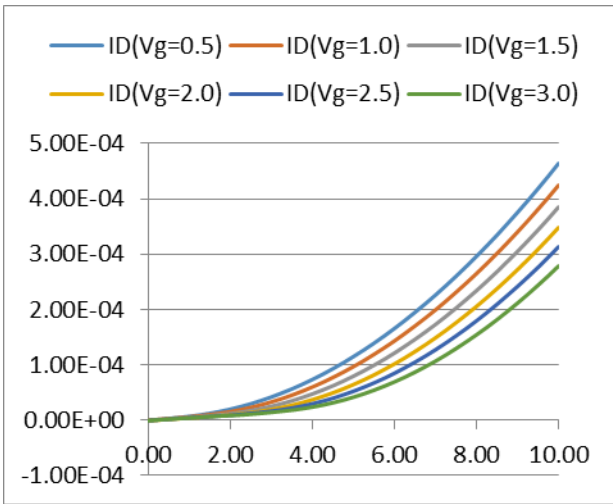


Fig.109: Ids vs Vds curves

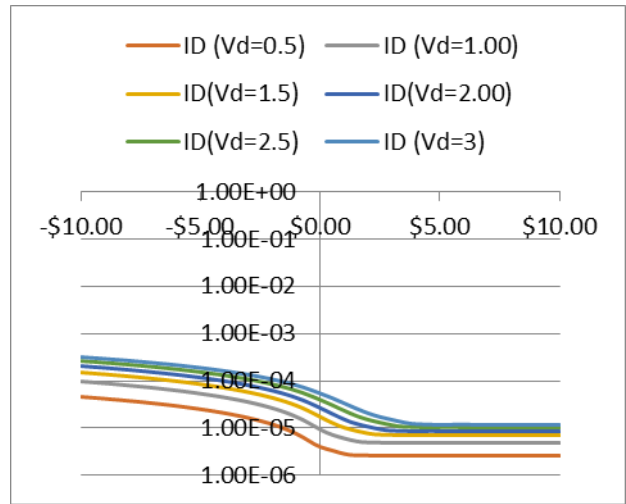


Fig. 110 : Ids vs Vgs curves